Local Buckling and Crippling of Composite Stiffener Sections

by

David Louis Bonanni

Thesis submitted to the Faculty of the
Virginia Polytechnic Institute and State University
in partial fulfillment of the requirements for the degree of
Master of Science
in
Aerospace Engineering

APPROVED:

Eric R. Johnson, Chairman

Rakesh K. Kapania

Zafer Gurdal

April, 1988
Blacksburg, Virginia

Local Buckling and Crippling of Composite Stiffener Sections

by

David Louis Bonanni

Eric R. Johnson, Chairman

Aerospace Engineering

(ABSTRACT)

The local buckling, postbuckling, and crippling (failure) of channel, zee, and I- and J-section stiffeners made of AS4/3502 graphite-epoxy unidirectional tape are studied by experiment and analysis. Thirty-six specimens were loaded in axial compression as intermediate length columns. Examination of the experimental results indicates the existence of a number of damage initiation modes, all of which involve either delamination in some part of the specimen or local material strength failure in a corner of the specimen. The ratio of the flange width to thickness has a strong influence on the buckling stress and damage initiation mode. The inner corner radius strongly affects the buckling and crippling stresses for the I- and J-section specimens.

Comparison of the numerical results from a computer code for shell analysis (STAGS) with experimental data shows good correlation prior to buckling and at the buckling load, but diminished agreement in the postbuckling region. This lack of postbuckling correlation is attributed to the neglecting of transverse shearing deformations in the structural theory, inaccuracies in the modeling of in-plane boundary conditions, and damage initiation in the experimental specimens. A plane stress failure analysis for five of the specimens shows the compressive fiber mode criterion of Hashin correlates reasonably well with the first detectable damage event. Equilibrium is used to develop interlaminar stress equations for classical laminated plate theory that require high order derivatives of the displacements. Derivatives computed from discrete displacement data using the Discrete Fourier Transform are inaccurate due to the Gibbs phenomenon.

Acknowledgements

This work was performed while the author was a participant in the NASA-Virginia Tech Composites Program, and was funded through NASA grants NAG1-343 and NAG1-537. I wish to thank Dr. James H. Starnes of the Structural Mechanics Branch at NASA Langley Research Center for his support and guidance, technicians George W. Johnson and James J. Kiss for their invaluable assistance during the experimental portion of this study, and Dr. Norman F. Knight for his help with the STAGS computer code. I would also like to express my gratitude to Dr. Eric R. Johnson for the many hours of patient discussion and advice he has given me, and to Dr. Rakesh K. Kapania and Dr. Zafer Gurdal for serving on my committee.

Finally, I would like to thank my family for their encouragement, and Laurie Seaton for her truly inspiring patience and understanding during the course of this work.

Table of Contents

Introduction 1

1.1 Compressive Failure of Stiffened Panels 1

1.2 Columns Subject to Local Crippling Failure 2

1.3 Previous Work on Crippling of Composite Columns 4

1.4 Objectives of the Current Study 9

Experimental Program 11

2.1 Description of Specimens 11

2.2 Preparation of Specimens for Testing 16

2.2.1 Machining and Potting 16

2.2.2 Measurement of Initial Geometric Imperfections 20

2.2.3 Instrumentation 20

2.3 Test Procedure 23

Experimental Results and Observations 29

3.1 I-Section Specimens 29

3.1.1 Experimental Results 29

3.1.2 Description of Damage Events 38

3.1.3 Effects of Geometric Parameters 47

3.1.3.1 Flange Width-To-Thickness Ratio 47

3.1.3.2 Inner Corner Radius 48

3.2 J-Section Specimens 51

3.2.1 Experimental Results 51

3.2.2 Description of Damage Events 52

3.2.3 Effects of Geometric Parameters 66

3.2.3.1 Flange Width-To-Thickness Ratio 66

3.2.3.2 Inner Corner Radius 70

3.3 Channel and Zee Section Specimens 74

3.3.1 Experimental Results 74

3.3.2 Description of Damage Events 80

3.3.3 Effects of Geometric Parameters 80

3.3.3.1 Flange Width-To-Thickness Ratio 80

3.3.3.2 Inner Corner Radius 82

Analysis and Correlation With Experiment 85

4.1 Analysis Methodology 85

4.2 Bifurcation Buckling Analysis 86

4.2.1 Boundary Conditions 87

4.2.2 Material Properties 90

4.2.3 Corner Details 91

4.3 Nonlinear Analysis 92

4.4 Results of Analysis and Correlation With Experiment 94

4.4.1 Specimen Z6 94

4.4.2 Specimen I2 100

4.4.3 Specimen I16 110

4.5 Plane Stress Failure Analysis 118

Interlaminar Stress Postprocessor Development **126**

5.1 Derivation of the Interlaminar Stress Equations 126

5.2 Construction of a Fourier Series Approximation for Discrete Data 137

  5.2.1 Derivation of the Method 138

  5.2.2 Examples of the Method 142

    5.2.2.1 One-Dimensional Example 142

    5.2.2.2 Two-Dimensional Example 148

Summary and Conclusions **159**

6.1 Experimental Program 160

6.2 Analytical Program 163

6.3 Suggestions for Future Work 165

References **167**

Plane Stress Failure Criteria **170**

A.1 Hashin's Failure Criteria 170

A.2 Other Failure Criteria 171

Vita **172**

List of Illustrations

Figure 1. Specimen cross sections and geometric parameters 12
Figure 2. Examples of machined and potted test specimens 18
Figure 3. Initial geometric imperfection scanning rail 21
Figure 4. Close-up of imperfection measurement device and specimen 22
Figure 5. Typical specimen cross-sectional strain gage pattern 24
Figure 6. Sample moire′ interferometry pattern for a buckled specimen 25
Figure 7. Laboratory area and equipment 27
Figure 8. Close-up of test machine and prepared specimen 28
Figure 9. Typical experimental corner and free edge strain response 31
Figure 10. Crippling failure of specimen I5 32
Figure 11. Crippling failure of specimen I17 33
Figure 12. Compressive material failure of specimen I14 34
Figure 13. Dimensionless load-shortening plots for I-section specimens I1-I12, I15-I17 36
Figure 14. Dimensionless load-shortening plots for I-section specimens I13, I14, I18, I19 ... 37
Figure 15. Flange free edge and corner axial strains, specimen I2 41
Figure 16. Web center axial strains, specimen I2 42
Figure 17. Flange free edge and corner axial strains, specimen I5 44
Figure 18. Web center axial strains, specimen I5 45
Figure 19. Moire′ photographs of apparent mode change during testing of specimen I11 ... 46
Figure 20. Buckling stress versus flange width-to-thickness ratio, specimens I1-I19 50
Figure 21. Crippled specimen J4 exhibiting axially uneven fracture 53

Figure 22. Crippled specimen J13 54
Figure 23. Dimensionless load-shortening plots for J-section specimens 55
Figure 24. Cap corner axial strains, specimen J3 59
Figure 25. Flange and web displacements, specimen J3 60
Figure 26. Attachment corner axial strains, specimen J6 61
Figure 27. Flange center and free edge axial strains, specimen J6 62
Figure 28. Cap flange free edge and cap corner axial strains, specimen J7 64
Figure 29. Web center lateral strains, specimen J7 65
Figure 30. Flange center and free edge axial strains, specimen J13 67
Figure 31. Attachment corner axial strains, specimen J13 68
Figure 32. Buckling stress versus average flange width-to-thickness ratio, specimens J1-J14 . 72
Figure 33. Dimensionless load-shortening plots, channel and zee specimens 76
Figure 34. Dimensionless load-shortening plots, Ref. 8 channel specimens 77
Figure 35. Dimensionless load-shortening plots, Ref. 8 zee specimens 78
Figure 36. Corner axial and lateral strains, specimen Z1 81
Figure 37. Buckling stress versus flange width-to-thickness ratio for channels and zees 84
Figure 38. STAGS finite element model geometry for a zee section 88
Figure 39. Degrees of freedom for the STAGS 411 finite element 89
Figure 40. STAGS model geometry and finite element mesh for specimen Z6 97
Figure 41. Buckling mode of specimen Z6 98
Figure 42. Load-shortening curves for specimen Z6 of Ref. 8 and replicate 99
Figure 43. Axial surface strains for specimen Z6 at P = 3563.64 lb 101
Figure 44. Axial surface strains for specimen Z6 at P = 8365.96 lb 102
Figure 45. Axial surface strains for specimen Z6 at P = 12121.1 lb 103
Figure 46. STAGS model geometry and finite element mesh for specimen I2 105
Figure 47. Detail of filled corner region of I- and J-section specimens 106
Figure 48. Buckling mode of specimen I2 108
Figure 49. Load-shortening curves for specimen I2 109

Figure 50. Axial surface strains for specimen I2 at P = 994.87 lb 111
Figure 51. Axial surface strains for specimen I2 at P = 2772.79 lb 112
Figure 52. Axial surface strains for specimen I2 at P = 10289.02 lb 113
Figure 53. STAGS model geometry and finite element mesh for specimen I16 114
Figure 54. Buckling mode of specimen I16 116
Figure 55. Load-shortening curves for specimen I16 117
Figure 56. Axial surface strains for specimen I16 at P = 7931.24 lb 119
Figure 57. Axial surface strains for specimen I16 at P = 16530.64 lb 120
Figure 58. Axial surface strains for specimen I16 at P = 17797.55 lb 121
Figure 59. Laminated plate and interlaminar stresses at k + 1 interface 128
Figure 60. Protracted functions for the cylindrical bending example 146
Figure 61. Displacement w for 1-D cylindrical bending example 149
Figure 62. Second derivative of w for 1-D cylindrical bending example 150
Figure 63. Third derivative of w for 1-D cylindrical bending example 151
Figure 64. Fourth derivative of w for 1-D cylindrical bending example 152
Figure 65. Displacement function for the two-dimensional free edge example 153
Figure 66. W,xxxx for the two-dimensional free edge example 157
Figure 67. W,yyyy for the two-dimensional free edge example 158

List of Tables

Table 1. Test specimens 13

Table 2. Elements of the laminate stiffness matrix 17

Table 3. Measured specimen parameters 19

Table 4. I-section experimental results 39

Table 5. I-section average buckling and crippling stresses 49

Table 6. J-section experimental results 56

Table 7. J-section average buckling and crippling stresses 71

Table 8. Channel and zee section specimens from Ref. 8 75

Table 9. Channel and zee section experimental results 79

Table 10. Channel and zee section average buckling and crippling stresses 83

Table 11. Results of plane stress failure analysis 123

Chapter 1

Introduction

1.1 Compressive Failure of Stiffened Panels

The reduction of structural weight is of great concern to an aerospace vehicle designer. Weight pared from the structure creates the desirable alternatives of increased payload capacity or a decreased need for propulsive energy. For this reason, aerospace vehicle structures are usually of the semimonocoque type; that is, they have a stiffened, thin shell configuration. This method of construction combines thin-sheet coverings or skins with longitudinal stiffener members and transverse support elements. Incorporation of laminated composite materials into such a design offers further weight savings, due to the high strength-to-weight and stiffness-to-weight ratios of these materials.

Proper attachment between skin and stiffeners is vital if the system is to perform effectively. Metallic components are commonly joined by closely spaced mechanical fasteners. Composite stiffeners may be bonded, stitched, co-cured, or mechanically fastened to the skin. In any case, the connection between skin and stiffener is continuous or nearly continuous. The stiffeners themselves are thin-walled, prismatic structural elements consisting of flanges and webs; some of the more common open shapes are angles, blades, zees, channels, and I- and J-sections.

Compressive loading of a stiffened skin structure may cause loss of stability. Stiffened-skin panels are usually designed so that the skin buckles in compression before the stiffeners. As a consequence, the compressive load increases more rapidly in the stiffeners than in the postbuckled skin as the total compressive load on the panel is increased. For co-cured or secondarily bonded composite stiffeners, catastrophic panel failure may be initiated either by stiffener separation from the skin (also known as stiffener pull-off) or by local buckling and then crippling of the stiffener section. It is assumed in the present work that the stiffened panel design is such that the stiffener pull-off mode of failure does not occur prior to crippling.

Local buckling of a stiffener is characterized by the buckling of flange and web elements as separate plates which rotationally restrain each other at the element junctions, or corners. The corners themselves can remain straight and parallel. Thus, the cross section of the stiffener deforms, but does not rotate or translate. This may be distinguished from a global or overall buckling mode, common to long columns, in which the cross section of the column rotates and/or translates, but does not distort. Since local buckling is essentially a plate buckling phenomenon, these stiffeners, like buckled plates restrained along at least one unloaded edge, have postbuckling strength. Eventual failure of the stiffeners in the postbuckled state is known as stiffener crippling.

1.2 Columns Subject to Local Crippling Failure

The crippling mode of failure which is seen in thin-walled sections used as stiffeners in semimonocoque construction may also be observed in short length columns of the same cross section. Columns subject to local crippling failure are short enough to avoid Euler (global) buckling but long enough to prevent the end conditions from increasing the crippling stress. For metallic thin-walled columns, an effective slenderness ratio of about twelve is commonly used to obtain the crippling stress from tests. The process of stiffener crippling can be studied by examining the behavior of such short, prismatic, thin-walled columns.

The crippling of metallic stiffeners has been extensively studied and is relatively well understood; semi-empirical formulas and design curves were developed for this case some time ago. After local buckling, a compressively loaded metallic stiffener will continue to resist increasing load, until either the entire cross section of the stiffener weakens due to reduced section properties, causing failure in a global or overall buckling mode, or crippling occurs. The crippling failure mode for metallic thin-walled sections is a local collapse driven by material yielding at the junctures, or corners, between the stiffener elements. As the compressive load increases in the postbuckling regime, the in-plane load is redistributed from the deformed flanges and webs into the corners, causing a relatively higher level of compressive stress there. The maximum load the stiffener can support, called the crippling load, occurs when the level of stress in the corners is such that collapse of the column is imminent.

The crippling of laminated composite stiffeners is not so well understood. One of the sources of this relative lack of understanding is the existence of a number of possible failure modes for a composite stiffener; geometry, material properties, and stacking sequence may determine the mode of failure. This complexity is in marked contrast to the single mechanism for the metallic crippling mode.

1.3 Previous Work on Crippling of Composite Columns

Much of the early research on composite stiffener crippling was done by Spier[1-5]. In 1975, Spier reported on tests and analyses of three graphite-epoxy compression panels with co-cured stiffeners[1]. The stiffened panels were fabricated from AS/3501 graphite-epoxy, and two panels had I-section stiffeners while the third was blade stiffened. Traditional aircraft strength of materials techniques along with lamination theory were used to predict crippling loads. The predicted crippling loads correlated well with test results, even though the graphite-epoxy panels failed by delamination and not by yielding as is the case with ductile metals. However, the lack of data on the local crippling strengths of graphite-epoxy elements was cited as a deficiency for the analysis and design of stiffened panels in compression.

Spier subsequently provided crippling data by conducting tests on no-edge-free and one-edge-free graphite-epoxy plates for AS/3501 in Ref. 2, and for T300/5208 in Ref. 3. The plates had stacking sequences of $[\pm 45_A/0_B/\mp 45_A]_T$ for B/A ratios of 2, 4, and 6, which are common layups for stiffeners. Nondimensional logarithmic plots involving the crippling stress, buckling stress, and material ultimate compressive strength were presented following the methodology used for the compressive failure of ductile metal plates. In Ref. 3 the no-edge-free and one-edge-free crippling data for the graphite-epoxy plates were substituted into the parabolic equation used for inelastic buckling of short metal columns on the column strength curve[6] (also known as the Johnson parabola). Tests on short graphite-epoxy square tubes and I-section columns suggested this metals methodology for crippling of short thin-walled columns seemed reasonable for the graphite-epoxy specimens.

Spier pointed out in Ref. 3 that classical orthotropic plate buckling theory could not predict the buckling loads obtained from his tests on graphite-epoxy plates. In Ref. 4 this deficiency is attributed to neglecting transverse shearing deformations in the classical theory. Transverse shearing deformations are more pronounced for the low plate width to thickness ratios (b/t) that occur in the analyses of web and flange elements in intermediate length columns and stiffeners. In Ref. 7 Arnold developed a materially nonlinear theory for the failure analysis of compressively loaded composite plates. Reissner's nonlinear mixed variational principle was used to develop the analytical model. Transverse shear deformations and a nonlinear in-plane shear stress constitutive law were incorporated into the model. Using this more refined analysis Arnold achieved good correlation with the experimental buckling loads reported by Spier. Arnold used the maximum strain criterion to predict the crippling loads.

Spier presents results of extensive static and fatigue testing on graphite-epoxy compression members in Ref. 5. The test specimens included flat plates, columns with zee sections, channel sections, hat sections, and I-sections, and hat-stiffened panels. All these members were fabricated from AS/3501 graphite-epoxy with most of them having layups of $[\pm 45/0_3/90]_S$. Some specimens were tested statically to failure. Other specimens were first subjected to 10^5 cycles of compression-compression postbuckling fatigue and, if they survived, were then tested statically to failure. For the channel and zee section intermediate columns, the tests revealed that the buckling loads were lower for the fatigued specimens than for the corresponding unfatigued specimens. However, the crippling loads for corresponding fatigued and virgin specimens were about the same. Thus, the crippling load was essentially unaffected by compression-compression postbuckling fatigue. In addition, the test results showed the channel had a much lower crippling load than the zee section for a flange width to web width ratio (b_f/b_w) of approximately 0.6. The reduction in the crippling load for the channel section was attributed to a neutral axis shift at midspan during the postbuckling response. This shift in the neutral axis does not occur for a zee section.

The majority of the research discussed above attempts to directly extend the semi-empirical methodology used in the crippling analysis of thin-walled metallic compression members. It has not yet been established whether such an extension to a graphite-epoxy material system is reasonable. The mechanisms of failure for the graphite-epoxy system are quite different than for ductile metals. Instead of yielding with subsequent large plastic deformations to collapse, fiber dominated graphite-epoxy laminates exhibit nearly brittle behavior, and are quite susceptible to delamination. This realization led to the study on the crippling of graphite-epoxy compression members reported by Tyahla and Johnson[8].

Details of an experimental program on the crippling of channel and zee section columns fabricated from AS4/3502 graphite-epoxy are presented in Ref. 8. A 2024-T3 aluminum column with a channel cross section was also tested for comparison. The graphite-epoxy specimens had layups of $[\pm 45/\mp 45/90/0_3]_S$ and $[\pm 45/0/90]_{nS}$, where $n = 1, 2$. Examination of the specimens after failure by crippling showed a fracture across the section at midspan and free edge delaminations in the flanges. Just prior to the maximum load, or the crippling load, the axial strain gage data indicated large compressive strains in the corners of the section, which were nearly uniform through the thickness. At the free edges of the flanges, however, the axial strain gage data indicated a very large gradient through the thickness due to the severe bending of the flange in postbuckling. The bending of the flange at the free edge is accompanied by through-the-thickness shear and normal stresses, which may initiate delamination. It seemed likely, then, that failure would originate at the corner or at the free edge of the flange. (In crippling tests of graphite-epoxy channel sections, Spier's observation was that failure seemed to originate at the corners[2].) In the tests, the failure event occurred very rapidly so that the location of failure initiation could not be determined from visual observation. Examination of the recorded strain gage data after testing also provided little evidence as to where failure began. It was recognized that a postbuckling analysis of the specimens tested was needed to ascertain the internal state of strain and stress at crippling, and thus yield more evidence on which to base an investigation of the causes and location of failure. The current work extends directly from this research.

More recently, Reddy and Rehfield, et al.[9] have examined the behavior of I-sections fabricated from C3000/5225 graphite-epoxy woven cloth with five stacking sequences: $[45/0/-45]_S$, $[0/90/0]_S$, $[0/90/0/90]_S$, $[45/0/90/-45]_S$, and $[0/45/-45/90]_S$. The test specimens were sized using metallic stiffener design charts and procedures. The methodology employed to analyze local buckling in metallic stiffeners involves examining flange and web elements as individual one-unloaded-edge-free and no-unloaded-edge-free plates, respectively. The focus of the analysis is to determine which element buckles at the lowest load; this element is the buckling-critical element of the stiffener cross section. Reddy and Rehfield used such a technique to size their specimens with three objectives in mind: to ensure that Euler buckling would be prevented; to make the web the buckling-critical element of the cross section; and to prevent the stresses at buckling from exceeding laminate ultimate strengths. All specimens were tested to failure, and the buckling load, crippling load, initial postbuckled stiffness, and failure strain data were recorded. In addition, the NASTRAN code was used to predict buckling loads and mode shapes. The majority of the specimens fulfilled the design objectives, thus validating the use of the preliminary metals design methodology. Comparison of NASTRAN buckling loads with experiment showed good agreement for layups containing angle plies, but exhibited diminished correlation for specimens constructed of cross plies only. Also, it was observed that flange free edge delamination seemed to initiate failure.

The observation that failure was caused by free edge delamination was supported by high-speed photographic evidence in Ref. 10, in which Rehfield and Reddy extended their study of the specimens from Ref. 9. Two failure modes were isolated for these specimens, an ultimate strength type of failure in the web, and a flange free edge delamination failure which initiated the web failure process. In addition, the effects of transverse shearing deformations and material nonlinearity were explored. A conventional shear deformation theory provided good correlation with experimental buckling loads. Materially nonlinear effects proved to be largest in layups not containing angle plies, but were negligible in all cases examined. Finally, it was noted that multiple failure modes and criteria must be considered when the crippling of composite stiffeners is treated.

Given the flange free edge delamination failures observed in Refs. 8-10, it seems reasonable to search for ways to inhibit this failure mode and thus increase stiffener ultimate strength. Causbie and Lagace[11] took this approach by conducting a test program involving channel and angle sections manufactured from a thermoplastic material, graphite/APC-2 PEEK. While this material system should have little effect on buckling loads when compared to a graphite-epoxy thermoset of equivalent moduli, it might be expected that the increased interlaminar toughness of a thermoplastic would delay crippling in a delamination mode. In fact, in comparing the graphite/PEEK specimens with similar sections made of T300/5208 graphite-epoxy, no significant difference in crippling stress or mode was discovered. Failure still seemed to be driven by flange free edge delamination. An additional facet of the work in Ref. 11 is the application of a Ritz solution method to bound the initial buckling loads and mode shapes. The method was applied twice to the buckling-critical element in each stiffener section; once assuming clamped loaded edges, which gave an upper bound on the buckling load, and then again assuming simple-support of the loaded edges, which provided a lower bound. Junctures between elements were considered simply supported. The method yielded good results for the angle sections; the experimental buckling loads for the channel sections, however, were consistently above the upper bound from the Ritz method. This was attributed to the neglected restraint exerted on the critical element (the web) by the flanges.

Wang, et al. report in Ref. 12 on a test program involving channels with square corners, square tubes, and square tubes attached to portions of skin to represent stiffened panel segments. The specimens had a variety of symmetric and nonsymmetric stacking sequences fabricated from AS4/3501-6 graphite-epoxy. Linear buckling and nonlinear postbuckling finite element analyses using a 32 degree-of-freedom semi-Loof element were performed. Buckling loads obtained from this analysis correlated well with experimental results; however, failure could not be predicted from the postbuckling analysis, which was based on classical lamination theory. It was noted that for the problem of crippling of composite compression members, successful attempts at analysis must include three-dimensional effects. The presence of interlaminar stresses must be recognized and accounted for. In fact, all specimen failures in this test program were observed to be due to delamination. Ply delaminations were discovered at the corners of the channels and square tubes. In the square tube/skin stiffened panel segments, a large delamination completely across the width of the skin was noted, as well as delamination failures at the corners of the tube stiffener. It could not be determined whether the skin delamination began at the corners of the square tube or the free edge of the skin. A final interesting result was that despite the nonsymmetry of the layups in some of the square tube sections, no significant out-of-plane deflection was seen prior to buckling, probably due to the mutual restraint of the four plate elements in this closed section.

1.4 Objectives of the Current Study

It is clear that a considerable amount of work has been done in the area of composite stiffener crippling. It is also clear, though, that there are still problems to be studied. While a variety of numerical and analytical techniques have been utilized to obtain buckling information, very little postbuckling analysis has been performed. As pointed out in Refs. 10 and 12, any such postbuckling analysis must include some treatment of interlaminar stresses. An additional limitation in much of the previous work may be the approach taken. To simplify the analysis, individual elements in the column have been treated separately as flat plates in compression with idealized unloaded edge conditions; i.e., the elastic restraint provided by adjacent elements along the junctions has been neglected. While this approach may be useful at times, it would be more meaningful in assessing stiffener buckling and postbuckling response to consider the interactions of the column elements. This idea is supported by the failure of the Ritz method to accurately determine buckling loads in channel webs in Ref. 11, due to neglecting the rotational restraint imposed by the flanges.

The present study extends directly from the work of Ref. 8 and attempts to provide additional insights into the phenomena of local buckling and crippling of composite compression members. It consists of a combined experimental and analytical program which examines the crippling of channel, zee, and I- and J-section intermediate length columns made from AS4/3502 graphite-epoxy tape. The objectives are to

1. conduct fundamental experiments to determine how composite stiffener crippling differs from metallic stiffener crippling;

2. study the influence of cross section, layup, flange width, wall thickness, corner radius, and stiffener length on the buckling, postbuckling, and crippling behavior of graphite-epoxy stiffeners;

3. use the general purpose shell analysis computer code STAGS[13] to create computational models for the buckling and postbuckling response of selected test specimens which correlate well with experimental results; and

4. develop a postprocessor to the STAGS code which will estimate the interlaminar stresses.

Chapter 2

Experimental Program

2.1 Description of Specimens

Four column cross-sectional shapes were tested as a part of the current experimental program: I- and J-sections, channels, and zees. The geometric parameters for each section include web width b_w, flange width b_f, inner corner radius r_c, and thickness t , as shown in Figure 1. For all specimens, b_w is a constant 1.25 inches. The complete test matrix is given in Table 1.

The I-section specimens are designated I1 through I19. All four flanges of each section are the same width, and two flange widths are used, 1.25 inches and 0.75 inches. The inner corner radius r_c is either 0.125 inches or 0.250 inches. Nominal thickness t is either 0.04 inches or 0.08 inches, depending on the layup used. These cross-sectional parameters are combined in various ways to generate eight unique I-sections. Several lengths of each section were tested, both to evaluate the effect of column length on the crippling process and to provide more data points for each different combination of cross-sectional parameters.

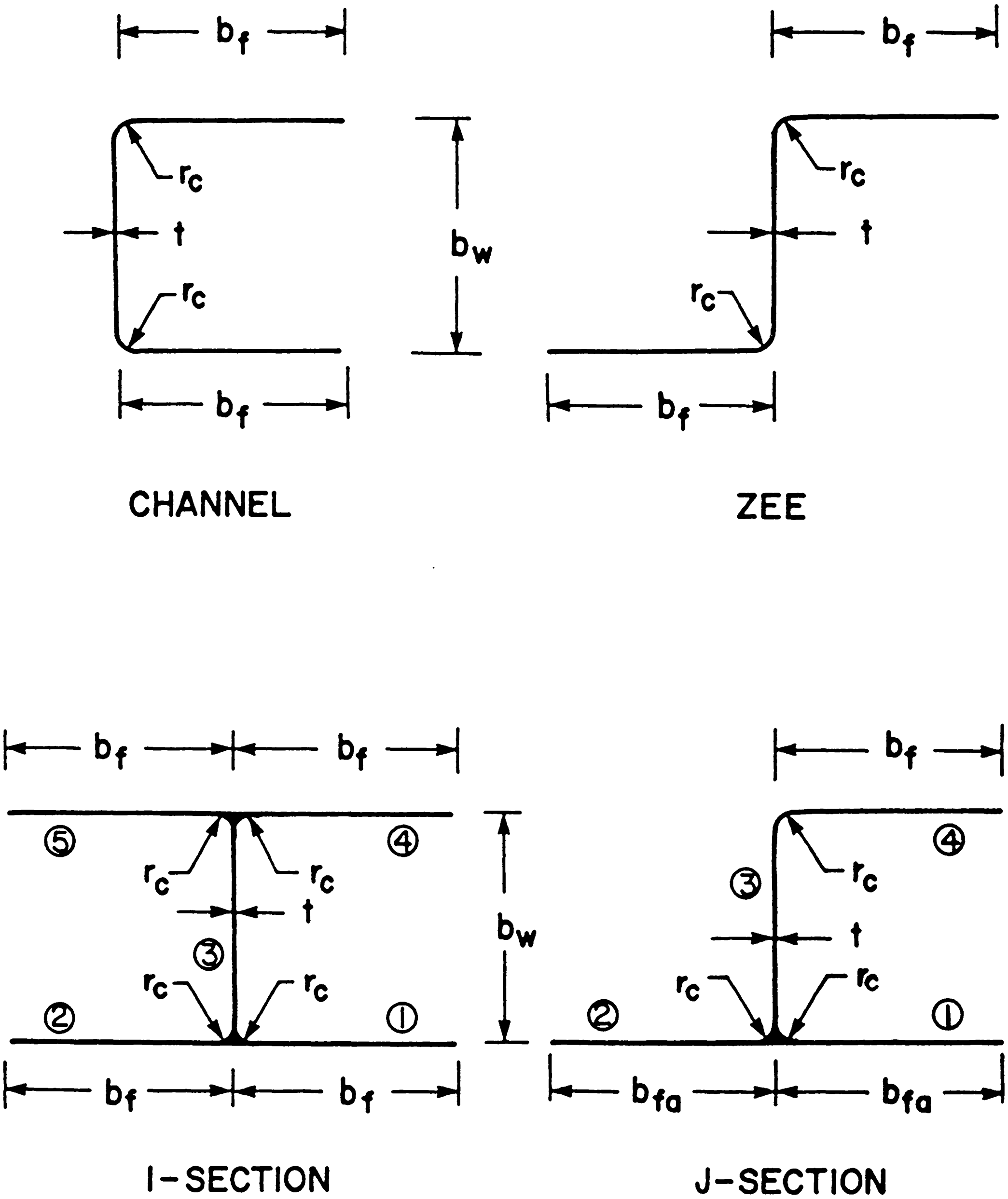

Figure 1. Specimen cross sections and geometric parameters

Table 1. Test specimens

Specimen designation[a]	Cross section	Flange width b_f, in.	Corner radius r_c, in.	Layup[b]	Gage length l, in.
I1	I	1.25	0.125	L8	4.0
I2	I	1.25	0.125	L8	6.0
I3	I	1.25	0.125	L8	12.0
I4	I	0.75	0.125	L8	4.0
I5	I	0.75	0.125	L8	8.0
I6	I	1.25	0.250	L8	4.0
I7	I	1.25	0.250	L8	8.0
I8	I	0.75	0.250	L8	4.0
I9	I	0.75	0.250	L8	8.0
I10	I	1.25	0.125	L16A	4.0
I11	I	1.25	0.125	L16A	8.0
I12	I	1.25	0.125	L16A	12.0
I13	I	0.75	0.125	L16A	4.0
I14	I	0.75	0.125	L16A	8.0
I15	I	1.25	0.125	L16B	4.0
I16	I	1.25	0.125	L16B	8.0
I17	I	1.25	0.125	L16B	12.0
I18	I	0.75	0.125	L16B	4.0
I19	I	0.75	0.125	L16B	8.0
J1	J	1.25	0.125	L8	4.0
J2	J	1.25	0.125	L8	8.0
J3	J	1.25	0.125	L8	12.0
J4	J	0.75	0.125	L8	4.0
J5	J	0.75	0.125	L8	8.0
J6	J	1.25	0.250	L8	4.0
J7	J	1.25	0.250	L8	8.0
J8	J	0.75	0.250	L8	4.0
J9	J	0.75	0.250	L8	8.0
J10	J	1.25	0.125	L16A	4.0
J11	J	1.25	0.125	L16A	8.0
J12	J	1.25	0.125	L16A	12.0
J13	J	0.75	0.125	L16A	4.0
J14	J	0.75	0.125	L16A	8.0
C1	Channel	0.50	0.125	L8	4.0
C2	Channel	0.50	0.125	L8	8.0
Z1	Zee	1.25	0.125	L16A	13.8

[a] All specimens have a web width, b_w, of 1.25 inches, and are made from AS4/3502 graphite-epoxy.

[b] Layup L8 denotes $[\pm 45/0/90]_S$, layup L16A denotes $[\pm 45/0/90]_{2S}$, and layup L16B refers to $[\pm 45/\mp 45/90/0_3]_S$.

The J-section specimens are designated J1 through J14. Each of the two attachment flanges in every specimen has a constant width b_{fa} of 1.25 inches. The single cap flange has a width b_f of either 1.25 inches or 0.75 inches. Two values of r_c , 0.125 inches and 0.250 inches, are used. Depending on the layup (L8 or L16A), the nominal laminate thickness is either 0.04 inches or 0.08 inches. No J-sections were tested with the L16B stacking sequence. These parameters are combined to create six unique J-sections, and, as in the case of the I-sections, several different lengths of each unique section were tested.

Since channels and zees with a variety of cross-sectional geometric parameters were considered in Ref. 8, only one type of cross section for each of these shapes was tested in the present program. The channel section has a b_f of 0.50 inches and an r_c of 0.125 inches, and is made from the eight ply stacking sequence L8 to yield a nominal laminate thickness of 0.04 inches. Specimens of this section with two different lengths, specimens C1 and C2, were tested. The only zee section in the test matrix, specimen Z1, has a flange width of 1.25 inches, an inner corner radius of 0.125 inches, and a nominal laminate thickness of 0.08 inches obtained by using the L16A layup.

As the main objective of the experimental program was to study local buckling and crippling, it was important to verify that the specimens in the test matrix would not buckle in a global or long column mode. The STAGS (STructural Analysis of General Shells)[13] computer code was used to fulfill this requirement. A linear bifurcation analysis, which provided buckling loads and modes, was performed for enough of the specimens to assure that all of the test specimens were short enough to avoid Euler buckling.

All specimens were made of AS4/3502 graphite-epoxy unidirectional tape. This material system is manufactured by Hercules Incorporated, has a nominal ply thickness of 0.005 inches, and has nominal material properties $E_1 = 18.5$ msi, $E_2 = 1.64$ msi, $G_{12} = 0.87$ msi, and $\nu_{12} = 0.30$. Three different layups were chosen for study, one containing eight plies giving a total nominal laminate thickness of 0.04 inches, and two composed of sixteen plies, yielding total nominal laminate thicknesses of 0.08 inches. The eight-ply layup is referred to as L8 and has a stacking sequence of

$[\pm 45/0/90]_S$, which produces quasi-isotropic laminate properties. The first sixteen-ply layup, identified as L16A, simply doubles the eight-ply stacking sequence, $[\pm 45/0/90]_{2S}$, and also results in a quasi-isotropic laminate. The final stacking sequence, termed L16B, is $[\pm 45/\mp 45/90/0_3]_S$, and produces orthotropic properties.

Since all three of the stacking sequences described are symmetric about the midplane, there should be no coupling between bending and extension; that is, there should be no non-zero terms in the **B** laminate stiffness matrix. However, the stiffener fabrication process resulted in some non-symmetric stacking sequences in the flange and/or web elements of the I- and J-sections, implying the existence of non-zero **B** matrix terms. Fabrication of I-section stiffeners of a given stacking sequence began with two sheets of graphite-epoxy material, each consisting of half the desired layup and each formed into a channel shape. The two "channels" were placed against each other, web to web, to create an I-section whose web had the proper thickness t, but whose flanges had a thickness of $t/2$. Small diameter rods of unidirectional material (sometimes called "licorice sticks") were made by rolling up the graphite-epoxy tape and were placed, with the fibers oriented along the length of the stiffener, into the gap formed at each of the two web-flange junctures to fill the I-section corners. Each pair of flanges was then covered with a single half-layup sheet of graphite-epoxy, to form an I-section with the proper thickness t in every flange and web element. Creation of J-section stiffeners of a given layup began with a single sheet of material of the desired stacking sequence. One edge of this sheet was bent to become the cap flange, and the other edge was split along the midplane and bent back ninety degrees to form two attachment flanges of thickness $t/2$. The middle of the sheet became the web. A "licorice stick" was laid into the interface between the attachment flanges and the web, and a single half-layup sheet was placed over the attachment flanges to give them the desired thickness.

The fabrication procedures for I- and J-section stiffeners discussed above preclude the creation of sections with a symmetric stacking sequence in every element; it was inevitable that at least one web or flange element in every stiffener specimen would have a non-symmetric layup, and thus possess consequent coupling between bending and extension. The number and location of non-symmetric elements varied with the specimen considered. The components of the membrane, coupling, and bending laminate stiffness matrices (**A**, **B**, and **D** respectively) for the L8, L16A, and L16B layups, both in their symmetric and non-symmetric variations, are given in Table 2. Nominal material properties and ply thicknesses are assumed.

2.2 Preparation of Specimens for Testing

2.2.1 Machining and Potting

All of the specimens tested were cut from longer stiffeners fabricated by the Lockheed-Georgia Company under NASA Contract NAS1-15949. If the specimens required any additional machining, for example a reduction in the width of a flange, it was done at this stage. The ends of each specimen were then potted in an aluminum-epoxy compound to a depth of approximately one inch, to provide the desired specimen test length (or gage length), l, as given in Table 1. (The total length of a specimen, including the potted regions, is denoted by L.) The potting was contained by an aluminum or steel ring. Finally, the potting and specimen ends were ground flat and parallel. These grinding and potting procedures were performed to ensure uniform load introduction to the specimen during the test and to prevent end brooming failures. Several machined and potted specimens are shown in Figure 2. In addition, many of the actual physical dimensions of each specimen were measured before testing; these results, along with a specification of the non-symmetric elements in the cross section of each specimen (as discussed in Section 2.1), are presented in Table 3.

Table 2. Elements of the laminate stiffness matrix

Element[a]	L8[b]		L16A[c]		L16B[d]	
	Sym.	Non-sym.	Sym.	Non-sym.	Sym.	Non-sym.
A_{11}, lb./in.	326.9 x 10³	326.9 x 10³	653.8 x 10³	653.8 x 10³	823.7 x 10³	823.7 x 10³
A_{12}	99.0 x 10³	99.0 x 10³	198.0 x 10³	198.0 x 10³	198.0 x 10³	198.0 x 10³
A_{16}	0.0	0.0	0.0	0.0	0.0	0.0
A_{22}	326.9 x 10³	326.9 x 10³	653.8 x 10³	653.8 x 10³	483.8 x 10³	483.8 x 10³
A_{26}	0.0	0.0	0.0	0.0	0.0	0.0
A_{66}	114.0 x 10³	114.0 x 10³	227.9 x 10³	227.9 x 10³	227.9 x 10³	227.9 x 10³
B_{11}, lb.	0.0	0.0	0.0	0.0	0.0	0.0
B_{12}	0.0	0.0	0.0	0.0	0.0	0.0
B_{16}	0.0	−212.4	0.0	−424.9	0.0	0.0
B_{22}	0.0	0.0	0.0	0.0	0.0	0.0
B_{26}	0.0	−212.4	0.0	−424.9	0.0	0.0
B_{66}	0.0	0.0	0.0	0.0	0.0	0.0
D_{11}, lb.-in.	39.9	39.9	342.5	342.5	278.3	278.3
D_{12}	21.1	21.1	137.2	137.2	168.9	168.9
D_{16}	6.4	0.0	21.2	0.0	4.2	0.0
D_{22}	31.4	31.4	291.5	291.5	292.4	292.4
D_{26}	6.4	0.0	21.2	0.0	4.2	0.0
D_{66}	23.1	23.1	153.2	153.2	184.9	184.9

[a] Nominal material properties and ply thickness are assumed; $t_{ply} = 0.005$ in., $E_1 = 18.5$ msi, $E_2 = 1.64$ msi, $G_{12} = 0.87$ msi, $\nu_{12} = 0.30$.

[b] The symmetric L8 layup is $[\pm 45/0/90]_S$; the non-symmetric variant of L8 is $[\pm 45/0/90_2/0/\pm 45]_T$.

[c] The symmetric L16A layup is $[\pm 45/0/90]_{2S}$; the non-symmetric variant of L16A is $[(\pm 45/0/90)_2/(90/0/\pm 45)_2]_T$.

[d] The symmetric L16B layup is $[\pm 45/\mp 45/90/0_3]_S$; the non-symmetric variant of L16B is $[\pm 45/\mp 45/90/0_6/90/\mp 45/\pm 45]_T$.

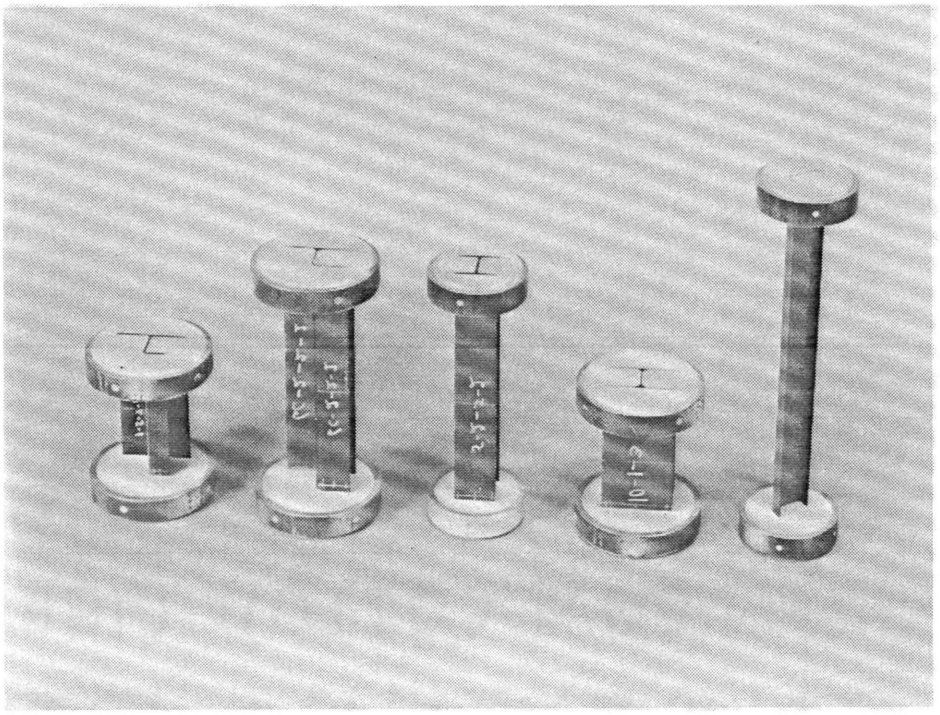

Figure 2. Examples of machined and potted test specimens

Table 3. Measured specimen parameters

Specimen designation	Thickness t_{avg}, in.	Flange widths		Web width $b_{w_{avg}}$, in.	Length l_{avg}, in.	Non-symmetric elements[b]
		$b_{f_{avg}}$, in.	$b_{fa_{avg}}$, in.[a]			
I1	0.0462	1.255	--	1.251	4.000	1,5
I2	0.0455	1.262	--	1.247	5.944	1,5
I3	0.0458	1.262	--	1.247	11.962	1,5
I4	0.0424	0.748	--	1.265	3.969	2,4
I5	0.0444	0.747	--	1.266	7.927	1,5
I6	0.0407	1.264	--	1.264	3.910	2,4
I7	0.0407	1.253	--	1.258	7.955	2,4
I8	0.0411	0.728	--	1.257	3.980	1,5
I9	0.0404	0.725	--	1.264	7.887	2,4
I10	0.0833	1.263	--		3.916	2,4
I11	0.0831	1.263	--	1.262	7.937	2,4
I12	0.0837	1.265	--	1.254	11.967	1,5
I13	0.0819	0.752	--	1.265	3.980	1,5
I14	0.0835	0.748	--	1.262	7.934	2,4
I15	0.0905	1.266	--	1.269	4.005	2,5
I16	0.0874	1.266	--	1.266	7.935	1,4
I17	0.0879	1.268	--	1.257	11.981	2,5
I18	0.0867	0.741	--	1.266	3.973	1,4
I19	0.0876	0.741	--	1.264	7.917	2,5
J1	0.0400	1.266	1.255	1.256	3.956	2
J2	0.0395	1.264	1.255	1.261	7.870	2
J3	0.0395	1.267	1.257	1.267	11.936	2
J4	0.0394	0.766	1.256	1.260	3.953	2
J5	0.0394	0.779	1.253	1.260	7.955	2
J6	0.0418	1.268	1.255	1.264	3.913	3,4
J7	0.0433	1.262	1.256	1.258	7.951	3,4
J8	0.0423	0.771	1.257	1.258	3.940	3,4
J9	0.0426	0.772	1.256	1.258	7.950	3,4
J10	0.0838	1.256	1.263	1.254	3.935	2
J11	0.0804	1.270	1.264	1.250	7.966	2
J12	0.0825	1.247	1.261	1.282	11.945	2
J13	0.0807	0.775	1.263	1.263	3.969	2
J14	0.0812	0.782	1.258	1.259	7.946	2
C1	0.0413	0.497	--	1.256	3.945	--
C2	0.0412	0.496	--	1.249	7.923	--
Z1[c]	--	--	--	--	13.813	--

[a] This column has meaning only for J-sections.

[b] Elements of the specimen cross section having non-symmetric layups (see Figure 1 for element identification numbers). Channels and zees do not have any non-symmetrically laid-up elements.

[c] The only measurement available for this specimen was average length.

2.2.2 Measurement of Initial Geometric Imperfections

Part of the way through the study, the initial geometric imperfections of the test specimens became a concern. Consequently, roughly half of the specimens (those which had not yet been instrumented at that time) were measured to determine initial imperfections. A photograph of the device used is shown in Figure 3. The main part of the imperfection measurement device is a cart with a direct current displacement transducer (DCDT) protruding from its underside. This cart could move along a rail, beneath which the potted specimens were placed such that the DCDT was in contact with some surface of the column (see Figure 4). By moving the cart along the rail, thus moving the DCDT over the desired specimen surface, and plotting the output from the DCDT directly on an X-Y plotter, some idea of the initial shape of the surface could be obtained. Typically, several axial scans and one lateral scan were made of every flat surface of each specimen, to give a three-dimensional description of the initial shape of each flange and web.

2.2.3 Instrumentation

The primary instruments used to monitor specimen response during the experiments were unidirectional electrical resistance strain gages and DCDTs. As stated in Ref. 8, crippling failure is believed to begin either at the corners or the flange free edges of the stiffener; these then are the areas of greatest interest in the cross section. In the postbuckled state, the corners experience high membrane strains, which should be independent of axial position, while the flanges undergo bending, which implies maximum axial surface strains at the wave crests. Thus the optimal axial position for strain gages and DCDTs to determine maximum bending strains and out-of-plane displacements is at one of these wave crests. The same STAGS linear bifurcation computer analyses used to verify local buckling of the specimens were studied to determine the axial locations of wave crests for each column. In some cases, the bifurcation buckling analysis revealed the

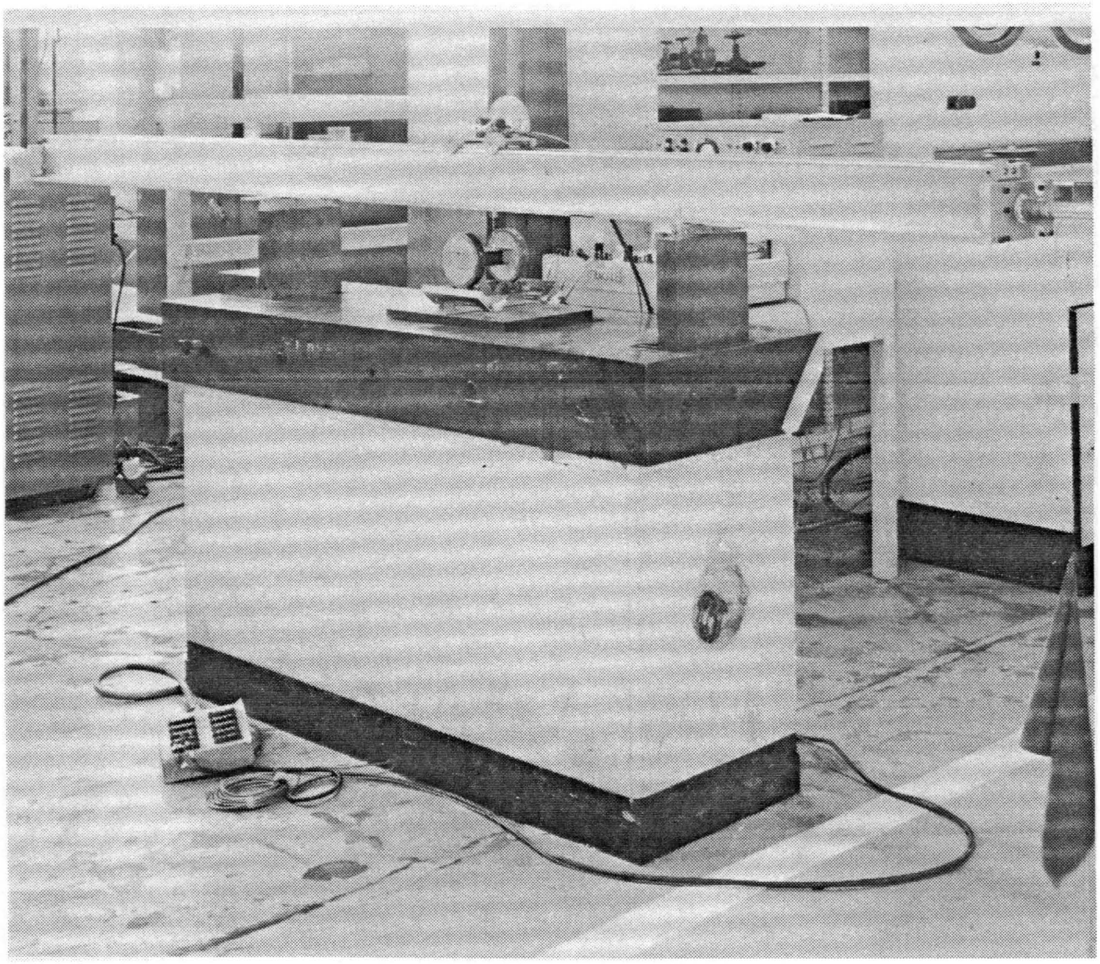

Figure 3. Initial geometric imperfection scanning rail

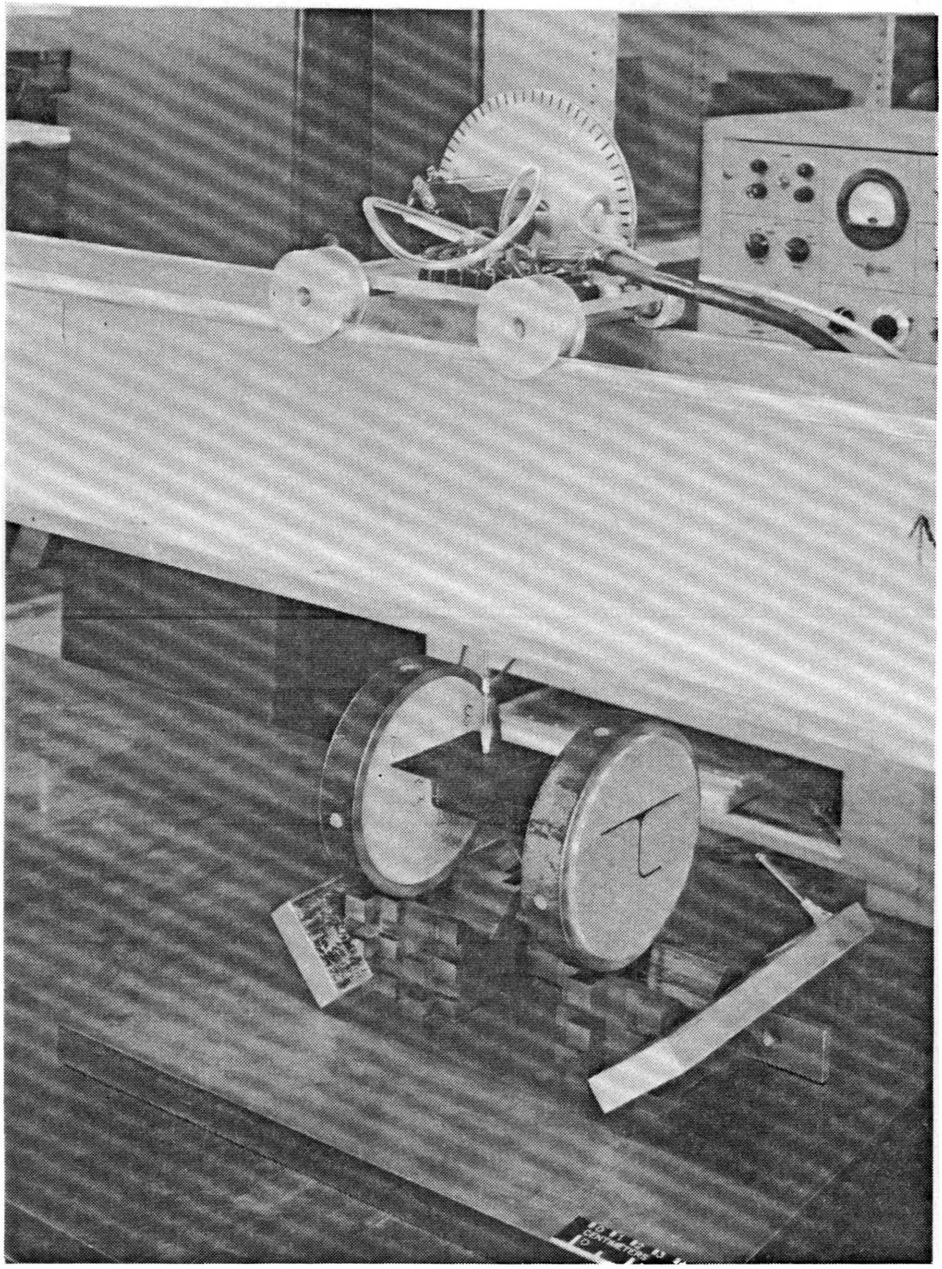

Figure 4. Close-up of imperfection measurement device and specimen

presence of higher buckling loads and modes which were close enough to the primary buckling load to warrant concern that a mode change might occur during the test. In these cases, one of the wave crests for these higher modes was also instrumented. A typical strain gage pattern for a given axial location is shown in Figure 5.

Gages were mounted in back-to-back pairs whenever practical, both to indicate bending strains and to aid in the detection of specimen buckling. When local buckling of one of the elements of the specimen cross section occurred, the back-to-back strain gage traces for that element diverged. DCDTs were typically positioned at the same axial locations as the strain gages, and placed at the flange free edges and web center to measure the maximum out-of-plane displacements of each cross-sectional element. In addition, one DCDT was placed in contact with the top platen of the test machine, to provide platen travel (or specimen end shortening) information. The DCDT traces also gave an indication of the buckling load. A qualitative measure of buckling load and mode was obtained through the use of moire′ interferometry, which provided real-time visible contours of the out-of-plane displacement of a desired specimen surface as the test progressed (see Figure 6). To facilitate this technique, the selected surface was painted white.

2.3 Test Procedure

When a specimen was ready to be tested, it was centered on the bottom platen of a 300-kip axial test machine. The attitude of the top platen of this machine could be adjusted to guarantee uniform load introduction at the start of the test. Leads from four widely spaced strain gages were attached to digital voltmeters, and the specimen was loaded to approximately ten percent of the expected buckling load. The top platen was adjusted until all four of the strain gages registered the same voltmeter readings, indicating a state of uniform strain across the column cross section, and thus a uniform loading condition. The specimen was then completely unloaded, and all strain gage and

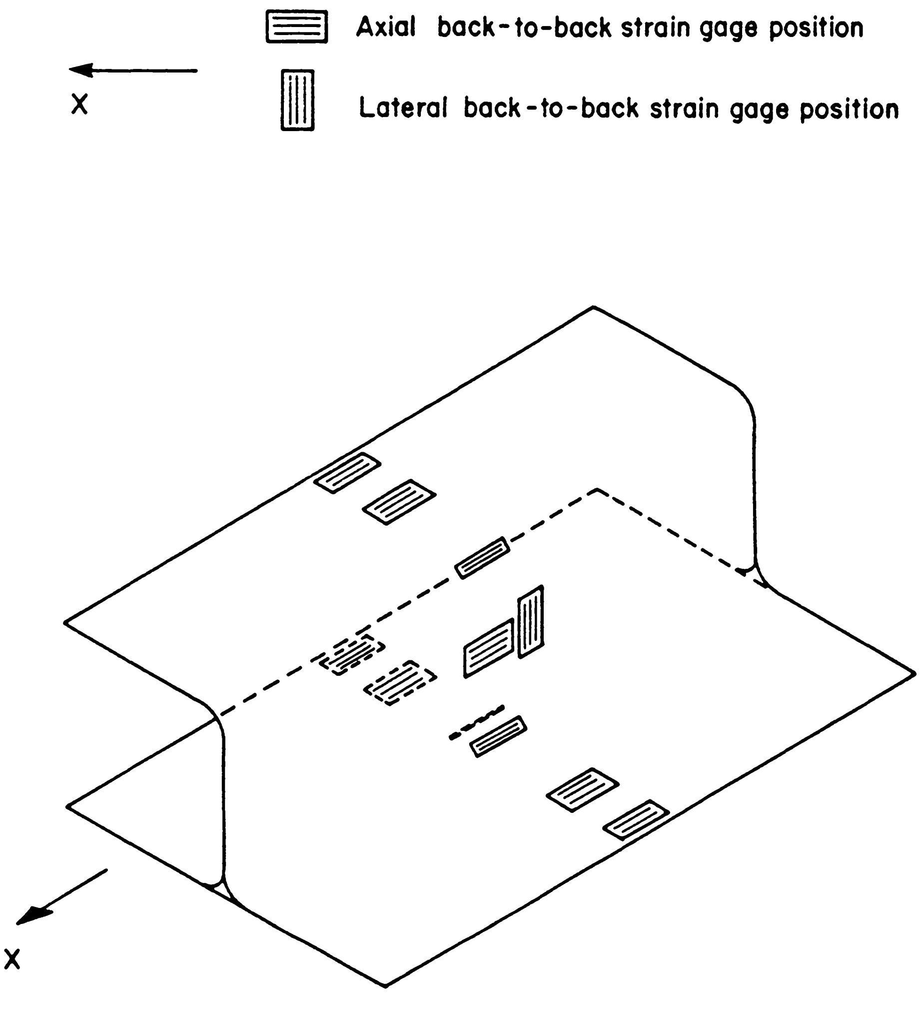

Figure 5. Typical specimen cross-sectional strain gage pattern

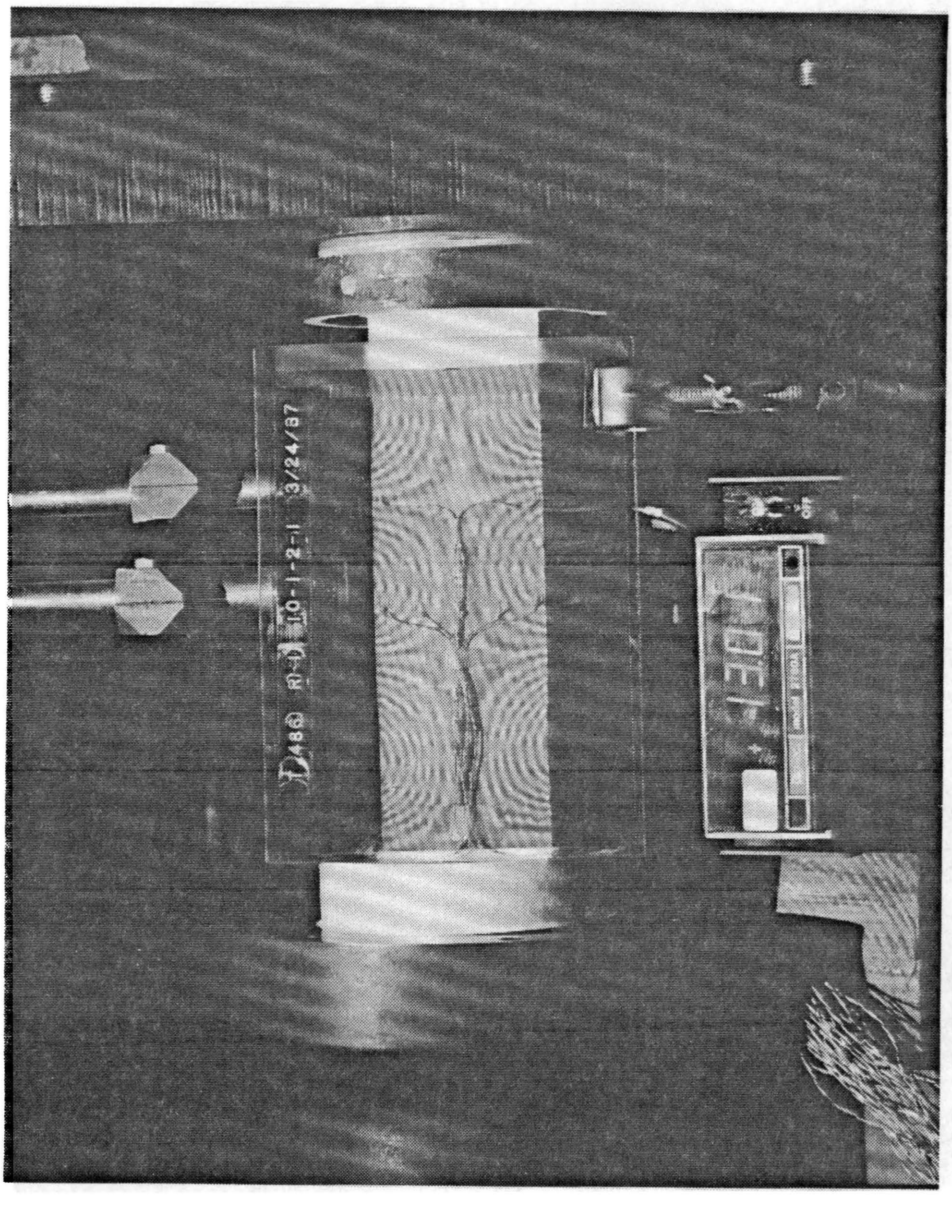

Figure 6. Sample moire′ interferometry pattern for a buckled specimen: specimen 17 at a load of 13010 pounds

DCDT leads were connected to a data acquisition system. In addition, signals from as many as eight strain gages were fed to two oscilloscopes for direct observation during the test. Typically, flange free-edge gages were chosen for display, to aid in the detection of buckling. A digital voltmeter was calibrated to show load, and placed next to the specimen.

DCDTs were positioned in contact with the back of the specimen, and the moire′ interferometry grid was placed in front of the specimen. The light source for the moire′ technique was adjusted to the proper intensity by checking the light meter on the laboratory camera. Figure 7 shows the test area including the testing machine, control console, and camera. Details of the loading area, such as a specimen, DCDTs, the load digital voltmeter, and a moire′ grid, all in position for a test, are visible in Figure 8. Once the moire′ equipment was correctly prepared, all instrumentation was set to zero for the zero loading condition, and loading of the specimen began. Load was increased at a slow rate, and data were taken every two seconds. Pictures of the specimen and moire′ fringe patterns were taken at regular intervals until the onset of buckling, and then whenever appropriate during the buckling process and in the postbuckling regime. All specimens were loaded to failure except specimen I11, which was removed from the machine after buckling but prior to failure for ultrasonic examination. After failure, the DCDTs and moire′ grid were moved away and photographs of the failed specimen were taken.

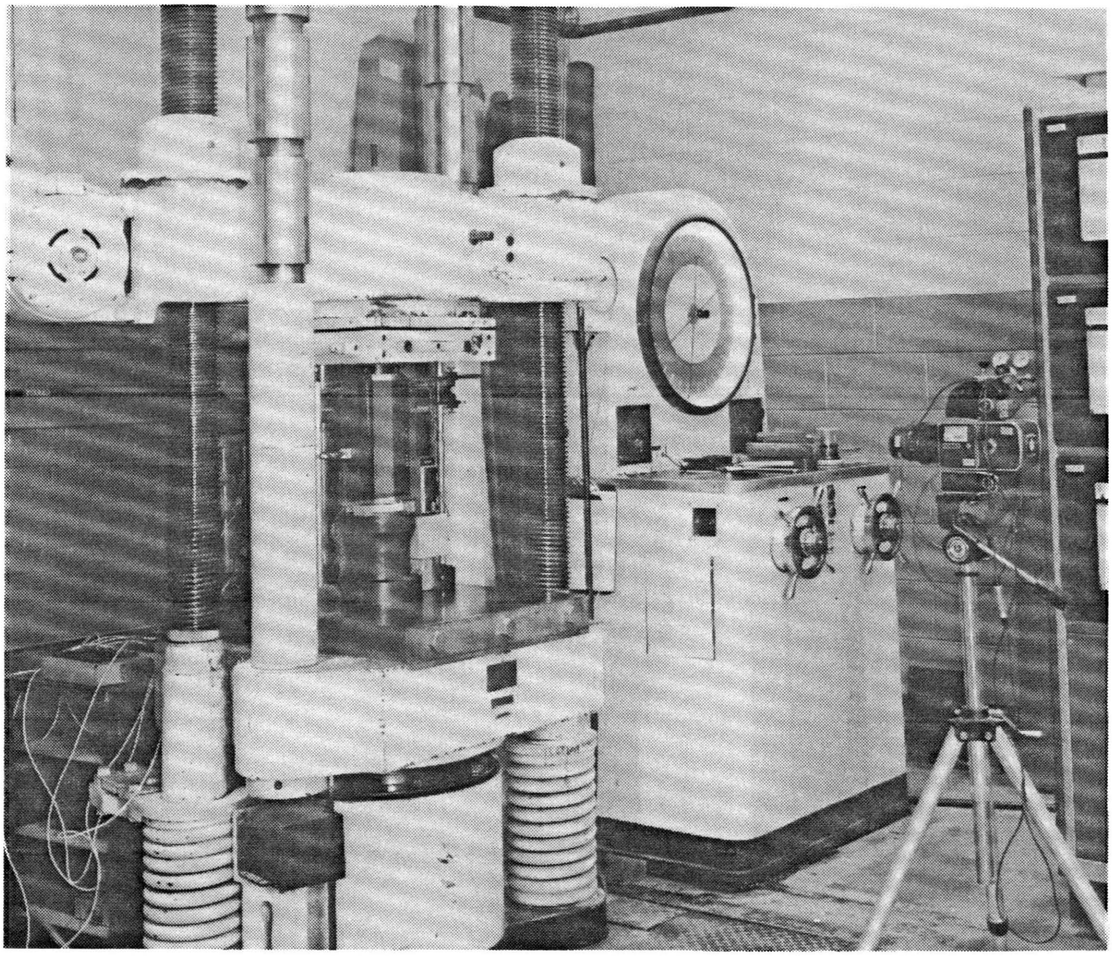

Figure 7. Laboratory area and equipment: test machine, controls, and camera

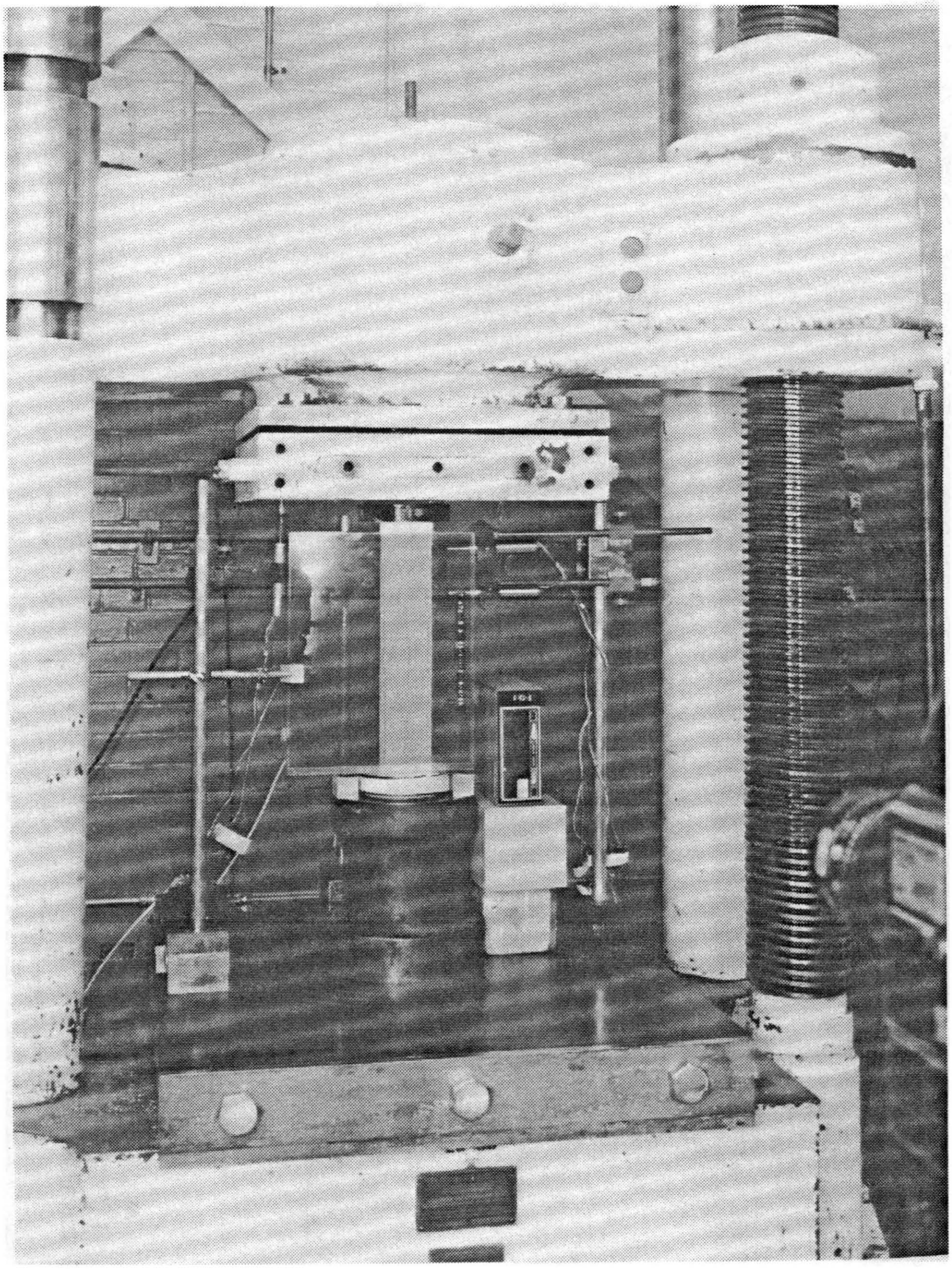

Figure 8. Close-up of test machine and prepared specimen

Chapter 3

Experimental Results and Observations

The results of the experiments performed are presented in three groups; first the I-section specimens are discussed, then the J-section specimens, and finally the channel and zee section specimens. Observations are also made concerning the effects of various geometric parameters on the experimental response within each group.

3.1 I-Section Specimens

3.1.1 Experimental Results

Nineteen I-section specimens were tested as a part of the experimental program. Local buckling followed by crippling failure was observed in fifteen of these specimens. Figure 9 shows axial strain gage data representative of the corner response and free edge behavior of all of the I-section specimens which crippled. Prior to buckling, a uniform state of strain exists within the specimens. In the postbuckling load range, the corners of the specimens experience large membrane strains and relatively little bending strain, while the free edges of the specimens experience the opposite. Crippling failure, as shown in Figure 10, is usually characterized by a fracture across the entire cross section combined with flange free edge delaminations involving only one or a few plies. Most of the crippled I-section specimens looked similar to specimen I5 shown in Figure 10. Specimens I15-I17, however, crippled as shown in Figure 11. Major delaminations involving only one ply interface are visible; these delaminations extend over a large portion of the specimen gage length and through the total width of each pair of coplanar adjacent flanges. No matrix cracking or broken fibers are in evidence. Such a crippling mode has not been previously documented in the literature. Four I-section specimens, I13, I14, I18, and I19, did not exhibit the response or failure characteristics described above, and thus are not considered to have failed in a crippling mode. Their behavior was more akin to that of a short column; that is, the axial membrane strain distribution in these specimens remained nearly uniform until a material compressive strength failure occurred. Local buckling and failure were virtually simultaneous for these four specimens. Figure 12 is a photograph of failed specimen I14; the delaminations involving many ply interfaces and occupying only a small portion of the specimen gage length, combined with a significant number of broken fibers, are typical of a material compressive strength failure.

Dimensionless load-shortening plots for the I-section specimens which failed in a crippling mode and for the I-section specimens which behaved as short columns are shown in Figures 13 and 14, respectively. In these figures the axial shortening u is normalized by the total length L of the specimen. The axial compressive load P is normalized by the effective axial stiffness $(EA)_{eff}$ of the specimen. The effective axial stiffness is defined by

$$(EA)_{eff} = KL\,, \tag{3.1}$$

where K is the prebuckling stiffness of the specimen calculated from the dimensional experimental load-shortening data. During the prebuckling response

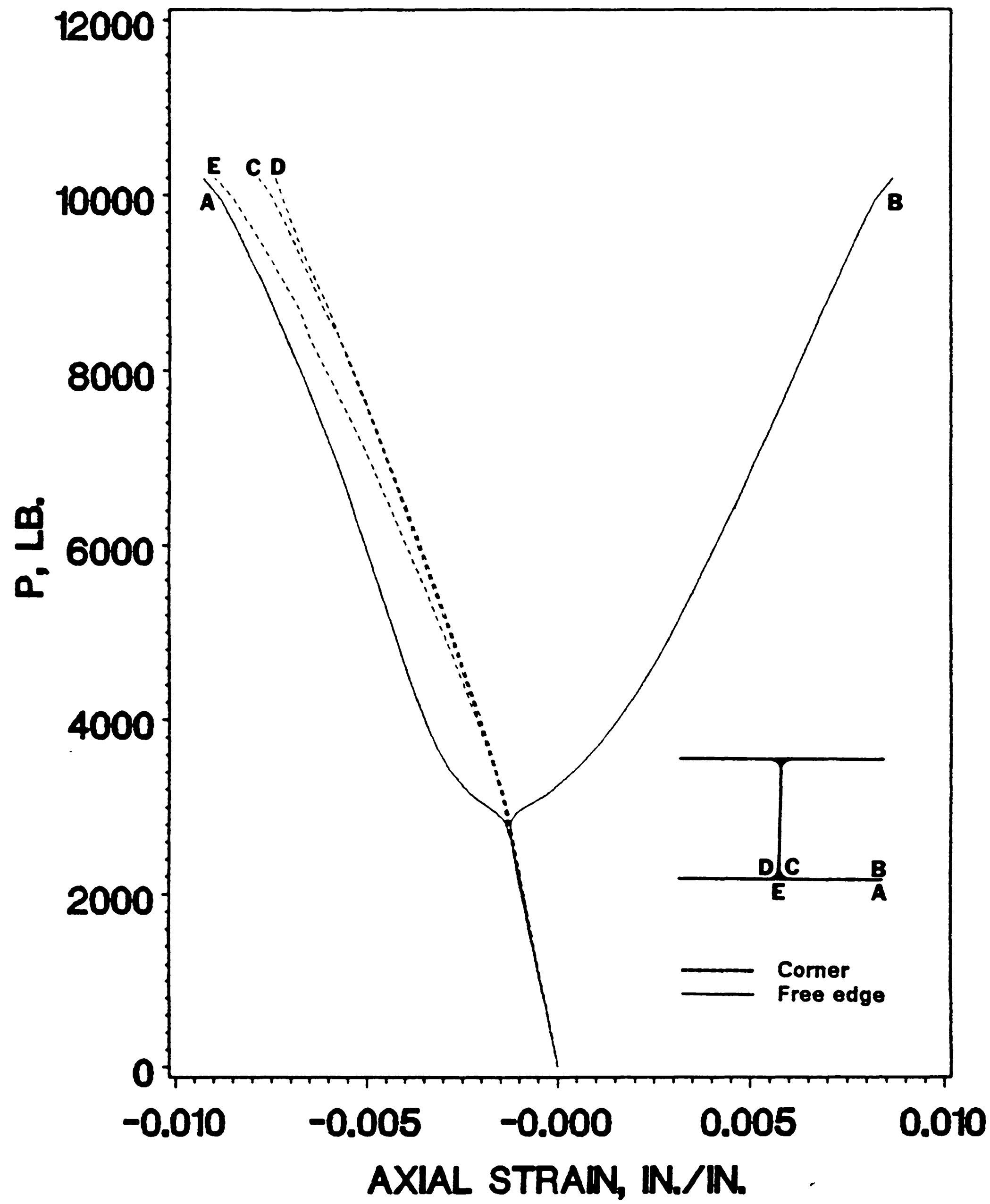

Figure 9. Typical experimental corner and free edge strain response: strain gage data for specimen I1 at *l*/2

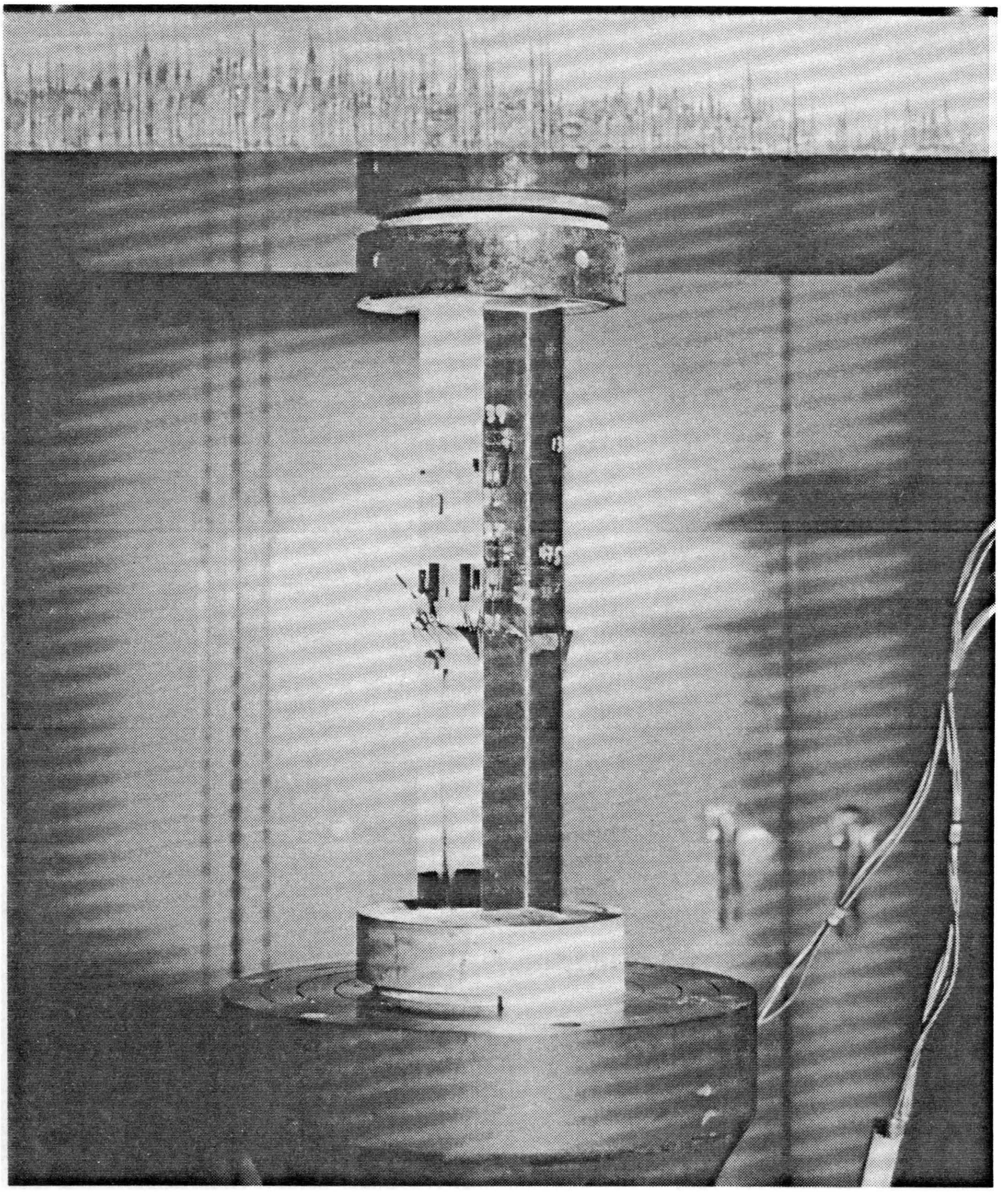

Figure 10. Crippling failure of specimen I5

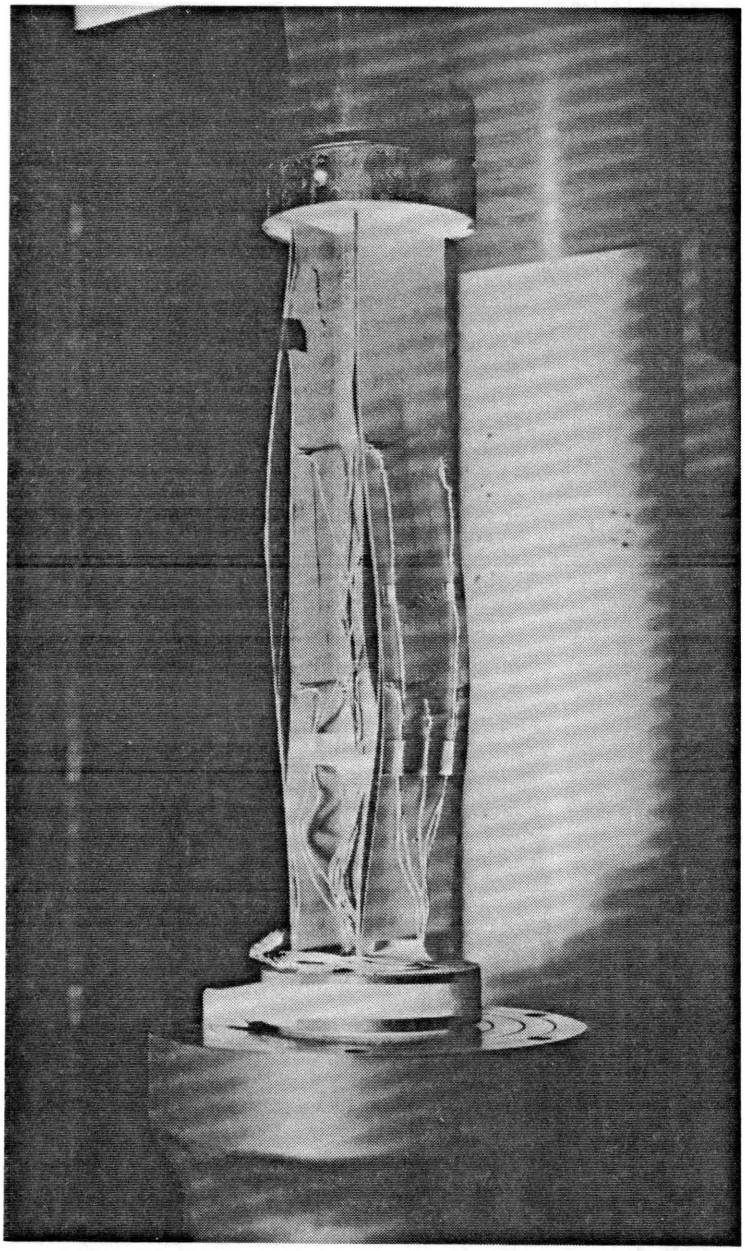

Figure 11. **Crippling failure of specimen I17:** previously undocumented failure mode involving extensive delamination across each coplanar pair of flanges and no matrix cracking or broken fibers

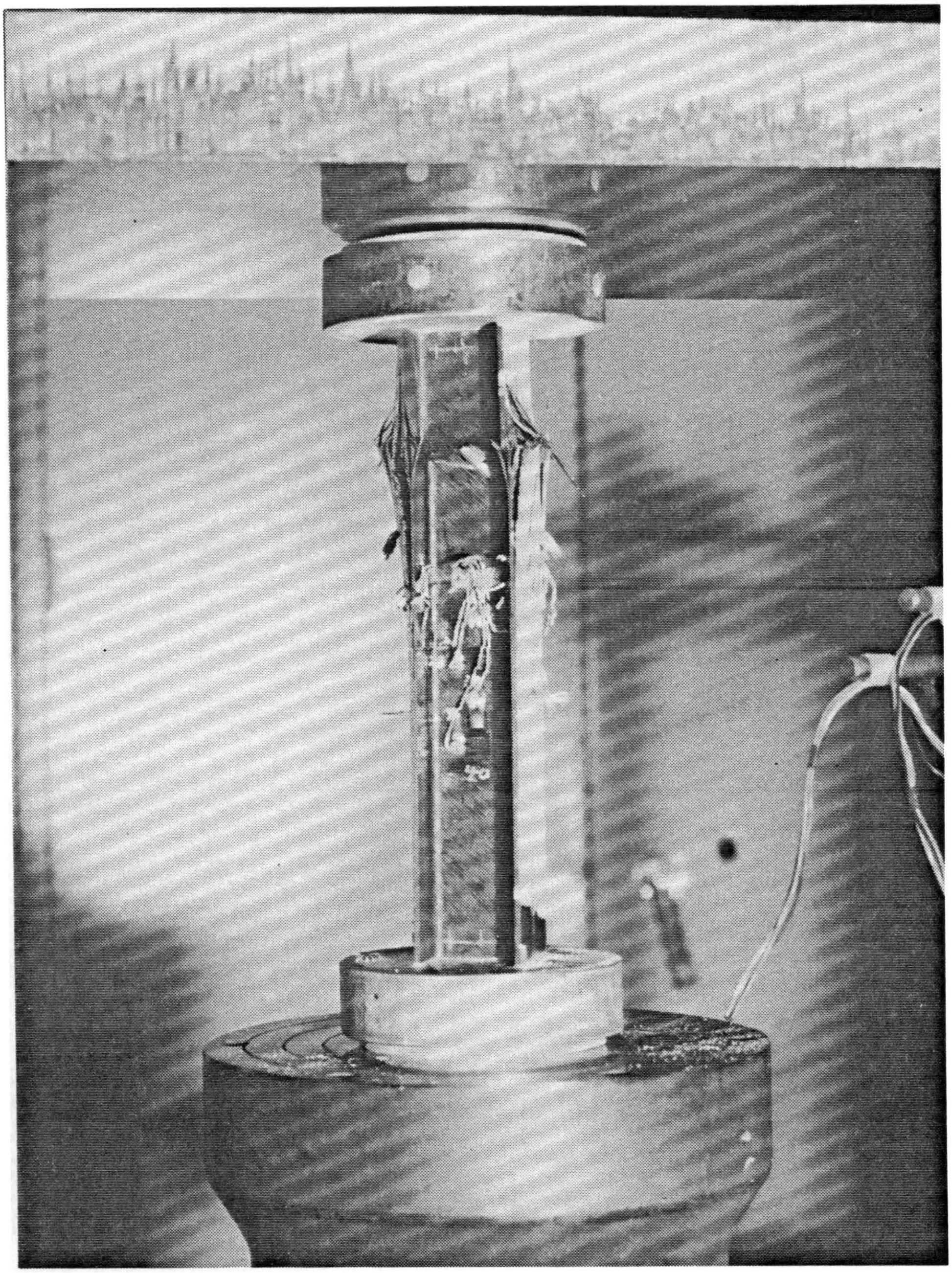

Figure 12. Compressive material failure of specimen I14

$$P = Ku \, . \tag{3.2}$$

Normalizing this expression,

$$\frac{P}{(EA)_{eff}} = \frac{KL}{(EA)_{eff}} \; \frac{u}{L}$$

which because of definition (3.1) becomes

$$\frac{P}{(EA)_{eff}} = \frac{u}{L} \; . \tag{3.3}$$

Equation (3.3) shows that the linear prebuckling paths for all specimens fall on a straight line with unit slope on the dimensionless load-shortening plot.

All specimens shown in Figure 13 exhibit load-shortening behavior typical of columns which buckle locally and then cripple in the postbuckled region except for I4, which shows a peculiar stiffening just before it buckles. No explanation for this behavior is offered. Moire′ interferometry photographs confirm that all of these specimens buckled in a local mode, including I4. The irregularities seen in the postbuckled paths of several specimens, for example I6 and I8, indicate damage events which occurred during the test. The specimens exhibiting short column behavior, if they buckled at all, buckled and failed almost simultaneously; thus the nonlinearity evident in Figure 14 is of a material, rather than geometric, nature.

Experimental results for all I-section specimens are presented in Table 4. As already discussed, K is the slope of the linear portion of the load versus end shortening plot, or the prebuckling stiffness. P_{cr} is the buckling load, which is obtained from experiment as the load at which plots of the data from back-to-back flange or web strain gage pairs diverge. It is also the load at which the load versus end shortening plot changes slope and becomes nonlinear. The buckling strain $\varepsilon_{x_{cr}}$ is simply the average axial membrane strain in each specimen at the buckling load, while the crippling load P_{cc} is the ultimate compressive load each specimen supported before failure. The last column of

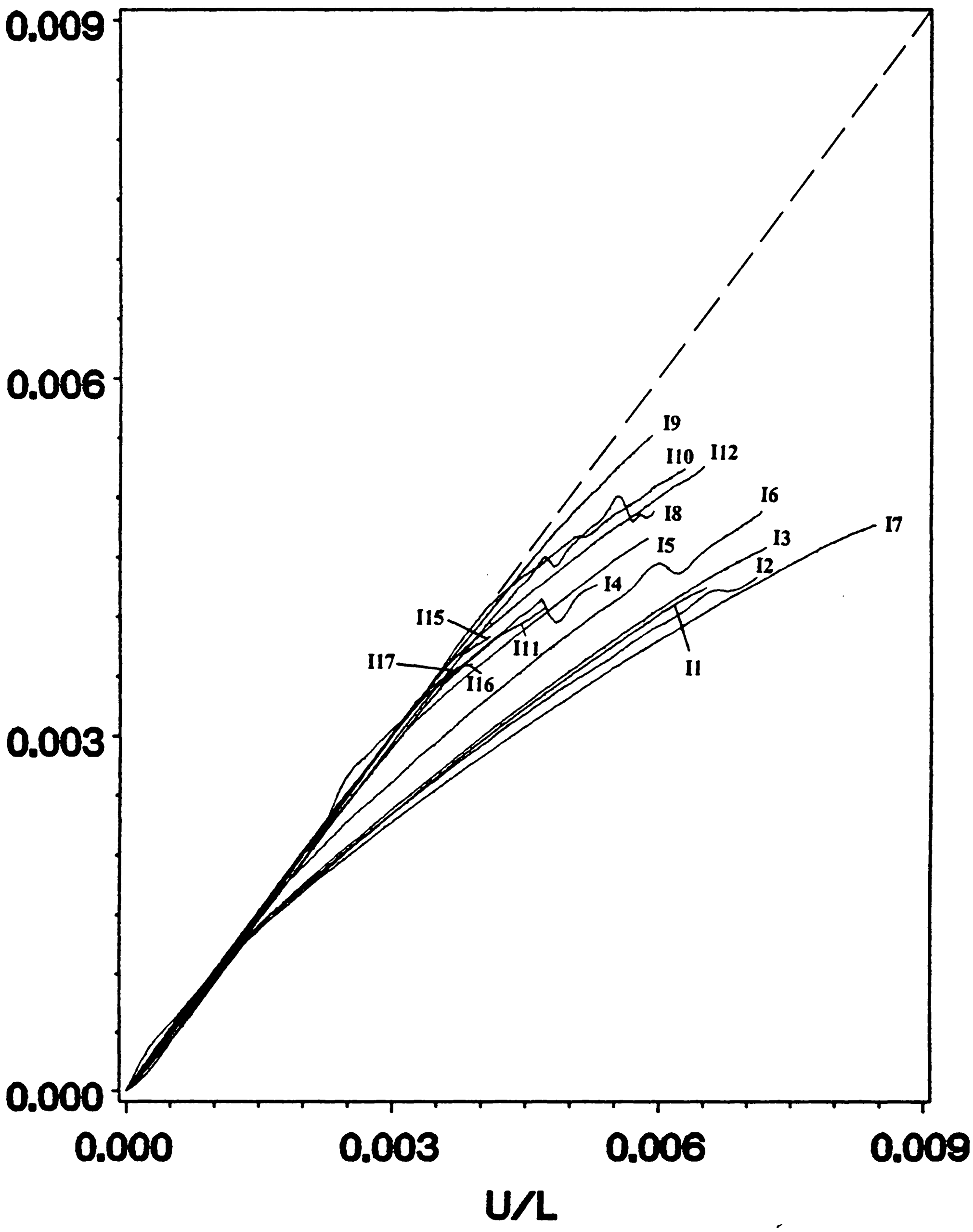

Figure 13. Dimensionless load-shortening plots for I-section specimens I1-I12, I15-I17: specimens which failed in a crippling mode

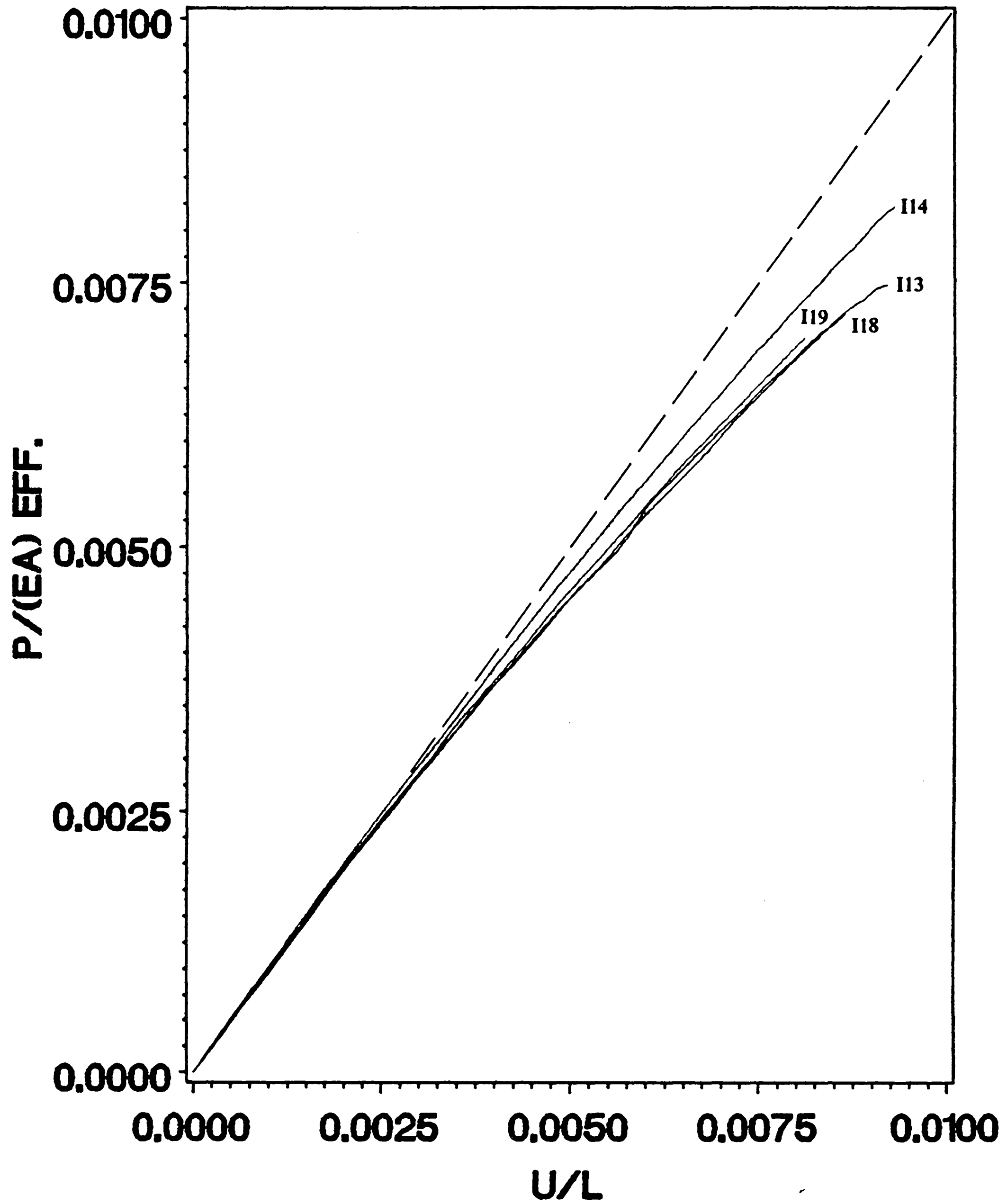

Figure 14. Dimensionless load-shortening plots for I-section specimens I13, I14, I18, I19: specimens exhibiting short column behavior

Table 4 gives an estimate of the nature and location of the first damage event which could be detected during each test, and is the result of detailed examination of strain gage and displacement transducer data gathered during each experiment. Also presented in Table 4 is the flange width-to-thickness ratio, $(b/t)_f$, defined by

$$(b/t)_f = \frac{(b_f - r_c - t/2)}{t} = \frac{b_f}{t} - \frac{r_c}{t} - \frac{1}{2} \ . \tag{3.4}$$

The flange width-to-thickness ratio is a measure of the width of the flat plate portion of a flange to its thickness. For composites with large ratios of the in-plane modulus of elasticity to the through-the-thickness shear modulus, and small ratios of width to thickness, significant transverse shear deformations can occur that are negligible in thin plates[14] . Thus, the small values of flange width-to-thickness ratio which are seen in many of the test specimens suggest that transverse shear or interlaminar shear effects, neglected in the classical theory, may be important in the current work.

3.1.2 Description of Damage Events

Three distinct types of damage events were isolated during the testing of the I-section specimens, as shown in Table 4. The first type (C) was damage occurring in a corner, due to a local compressive material strength failure. The second type of damage event was a flange free edge delamination (FD), while the third was a flange delamination occurring at the junction of two coplanar flanges and the web (CD); that is, a delamination of the flanges from the stiffened corner region. Several specimens showed evidence of pre-crippling delamination damage whose location could not be determined (D), and several more exhibited no damage events at all before failure (N).

Specimen I2 will be discussed as a representative example of those I-section specimens (I2, I3, and I6) whose first damage in postbuckling appeared to occur in one of the corners. Figure 15 shows plots of compressive load versus strain at an axial location of $l/3$ for a back-to-back axial strain gage

Table 4. I-section experimental results

Specimen designation	$(b/t)_f$[a]	Prebuckling stiffness K, lb./in.	Buckling load P_{cr}, lb.	Buckling strain[b] $\varepsilon_{x_{cr}}$	Crippling load P_{cc}, lb.	Location of first damage[c]
I1	27.625	400000	3000	-.0012	10195	N
I2	27.625	296450	2786	-.0011	10289	C
I3	27.625	151790	2500	-.0011	9751	C
I4	15.125	310700	5290	-.0034	7966	FD
I5	15.125	176800	5290	-.0033	8244	FD
I6	24.500	648210	5890	-.0020	18971	C
I7	24.500	421050	4860	-.0016	20106	FD
I8	12.000	457150	11710	-.0049	13698	D
I9	12.000	263160	11860	-.0052	14535	FD
I10	13.563	714200	16875	-.0042	22475	FD
I11[d]	13.563	434740	14536	-.0037	-------	CD
I12	13.563	282150	14071	-.0035	20774	D
I13	7.3125	607050	26710	-.0100	27291	C[e]
I14	7.3125	323230	26570	-.0101	26606	N
I15	13.563	853600	18214	-.0036	19663	D
I16	13.563	492850	16536	-.0032	17798	D
I17	13.563	339290	15643	-.0031	17060	D
I18	7.3125	714300	30290	-.0097	30874	N
I19	7.3125	403580	28190	-.0090	28192	N

[a] Flange width-to-thickness ratio.

[b] Average axial strain in the cross section at buckling.

[c] This column refers to the suspected nature and location of the first major damage event within the specimen as inferred from experimental data:

C -- corner damage
FD -- delamination in flange at free edge
CD -- delamination in flange at corner
D -- delamination at unknown location
N -- no damage observed prior to failure.

[d] Test was stopped prior to failure so that the specimen could be c-scanned.

[e] Damage occurred prior to buckling at an axial strain level of approximately -.0090 in/in. Very little evidence of further damage in postbuckling was found.

pair located at the free edge of a flange, and for the three axial strain gages mounted on the corner nearest that flange. A discontinuity in the strain plots at $P = 10000$ lbs. is evident in all curves, and is indicative of a damage event which took place somewhere in the specimen. For this material system, a one-percent compressive strain is close to the ultimate strain in the fiber direction. Since the corners of each I-section specimen are largely filled with 0° fibers, and since Figure 15 shows axial strains in the corners to be approaching one percent at a load of 10000 lbs., corner damage due to local material compressive failure is strongly suggested. On this evidence alone, however, the possibility that the observed damage was a flange delamination cannot be eliminated. Data from a back-to-back pair of axial strain gages mounted at the center of the web at an axial location of $l/12$ are presented in Figure 16. The large and discontinuous increase in axial bending observed at a load of 10000 lbs. indicates that the damage occurred close to this axial location (final failure in fact occurred at $l/4$). The magnitude of this bending increase also suggests that one or both corners were damaged and thus the elastic restraint of the web connections to the flanges was abruptly reduced; a delamination in a flange would not be expected to generate such a large response in the web, as will be shown in the next paragraph.

The damage behavior of specimen I5 is representative of the response of I-section specimens whose first damage event is due to a flange free edge delamination (I4, I5, I7, I9, and I10). Plots of load versus axial strain for a flange free edge strain gage pair and the nearest set of corner gages at an axial location of $7l/16$ are presented in Figure 17. A damage event at a load of approximately 7500 lbs. is indicated by the bending increase in the back-to-back flange free edge pair; no damage is evident in the corner strain gage plots. The strain gage data from the other corner of specimen I5 also exhibit no damage. In addition, an axial membrane strain level of about -.0056 in/in existed in the corners at a 7500 lb. load, which is well below the ultimate compressive strain of this material system. These findings suggest that the damage event observed did not occur in or near a corner of the specimen. The evidence in Figure 17 also eliminates the possibility that the damage was due to a flange delamination at one of the junctions of two flanges and the web, since this damage mode is essentially a delamination of the flanges from a corner and would be evident in the corner strain

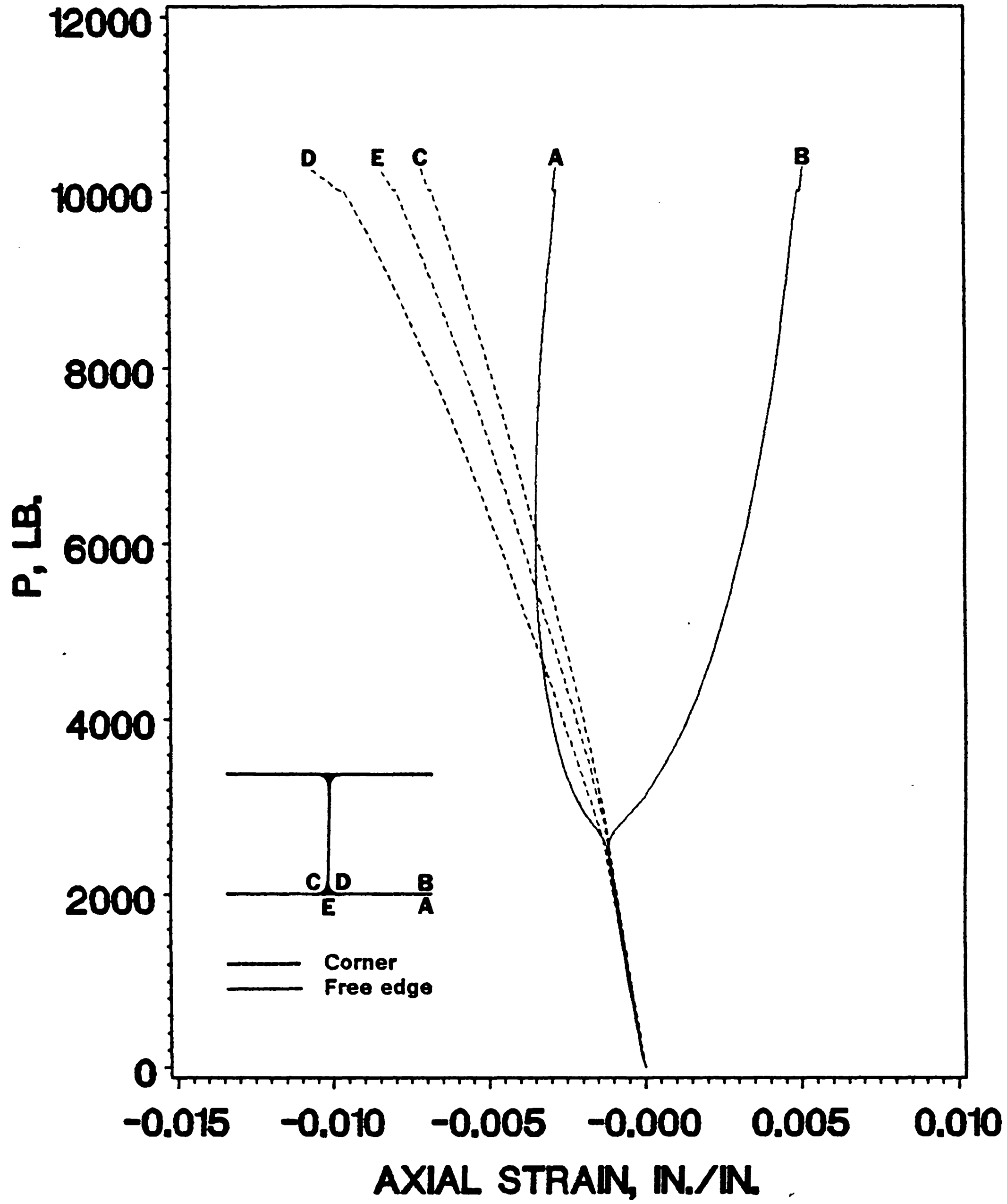

Figure 15. Flange free edge and corner axial strains, specimen I2: strain gage data at an axial location of $l/3$

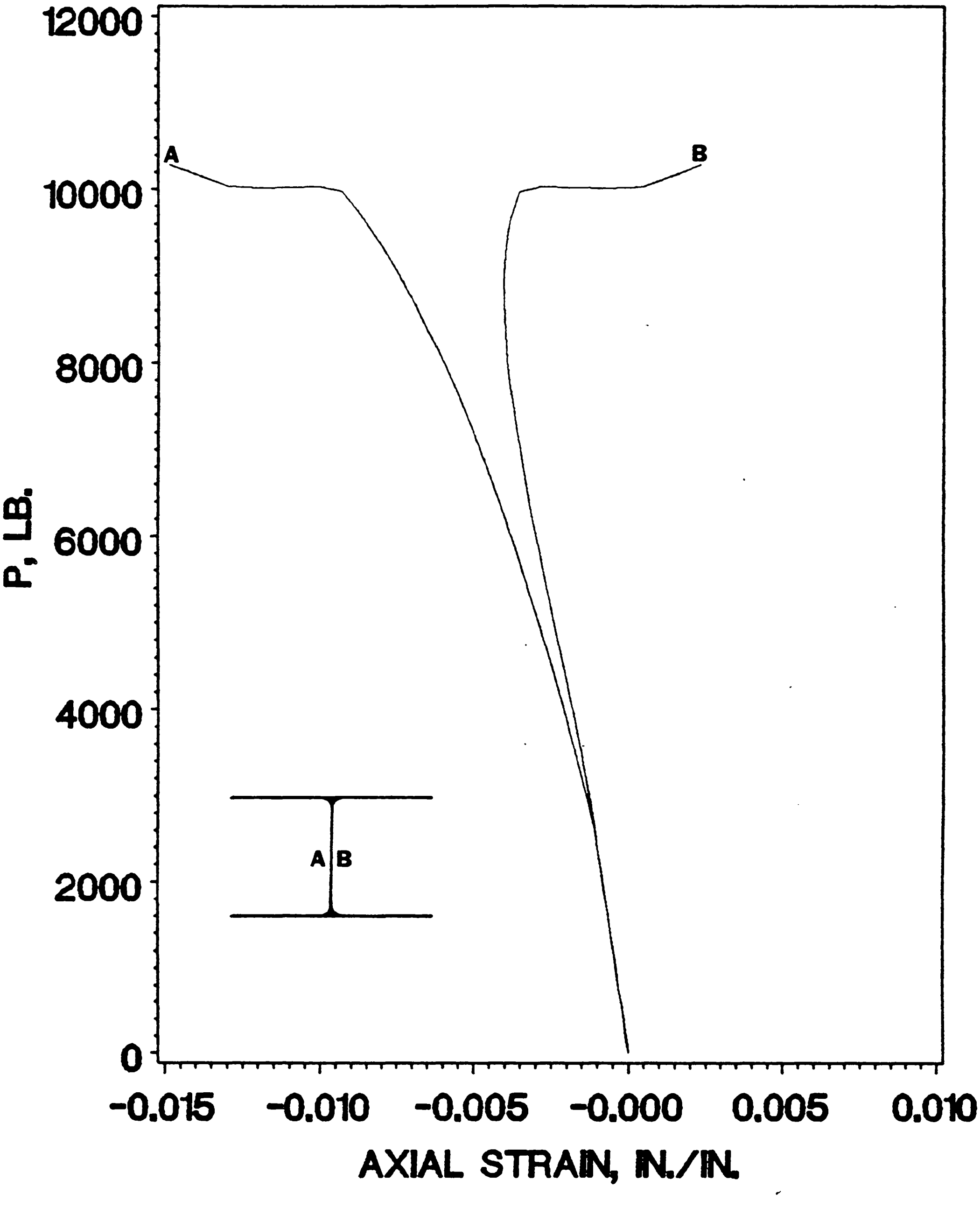

Figure 16. Web center axial strains, specimen I2: strain gage data at an axial location of *l*/12

gage data. The damage observed in specimen I5, then, must be the delamination of one or more flanges at the free edge caused by interlaminar stresses. For the purpose of comparison with specimen I2, back-to-back axial strain gage data from the center of the web of specimen I5 at an axial location of $l/4$ are plotted in Figure 18. The gentler nature of the bending increase seen in this figure is representative of the effect of a flange free edge delamination on the web response, and is in marked contrast to the bending increase exhibited in Figure 16, which was produced by corner damage.

Specimen I11 was the only I-section specimen tested which showed evidence of the third damage type, a delamination of the flanges from the flange-web junction. This specimen was not tested to failure; loading was stopped at 17450 lbs. after loud cracking noises were heard. No visible specimen damage was observed. Ultrasonic examination of specimen I11 revealed damage zones (delaminations) at both of the junctions where two flanges and the web meet, extending into the flanges and roughly centered over the web. This damage was apparently due to interlaminar stresses in the flanges over the corner created by in-plane lateral stresses in the web, and occurred at a load of about 16850 lbs. Undetected manufacturing defects in the corner may have contributed to this process. The strain gage and DCDT information from this test were not helpful in determining the nature or location of the damage, except to suggest that a mode change may have been taking place at roughly the same time. The number of halfwaves seen in the deformed flanges and the web changed at approximately $P = 16850$ lbs., as may be noted from the moire′ interferometry photographs in Figure 19. In Figure 19(a), two well-developed halfwaves and one clear but weaker halfwave are visible at a load of 15820 lbs. At a load of 17340 lbs., in Figure 19(b), only two well-developed halfwaves are seen. It could not be determined whether the damage caused the apparent mode change or vice versa. It is believed that at least some of the specimens in Table 4 whose strain gage and displacement transducer data proved inconclusive (I8, I12, and I15-I17) experienced damage by the same mechanism as specimen I11.

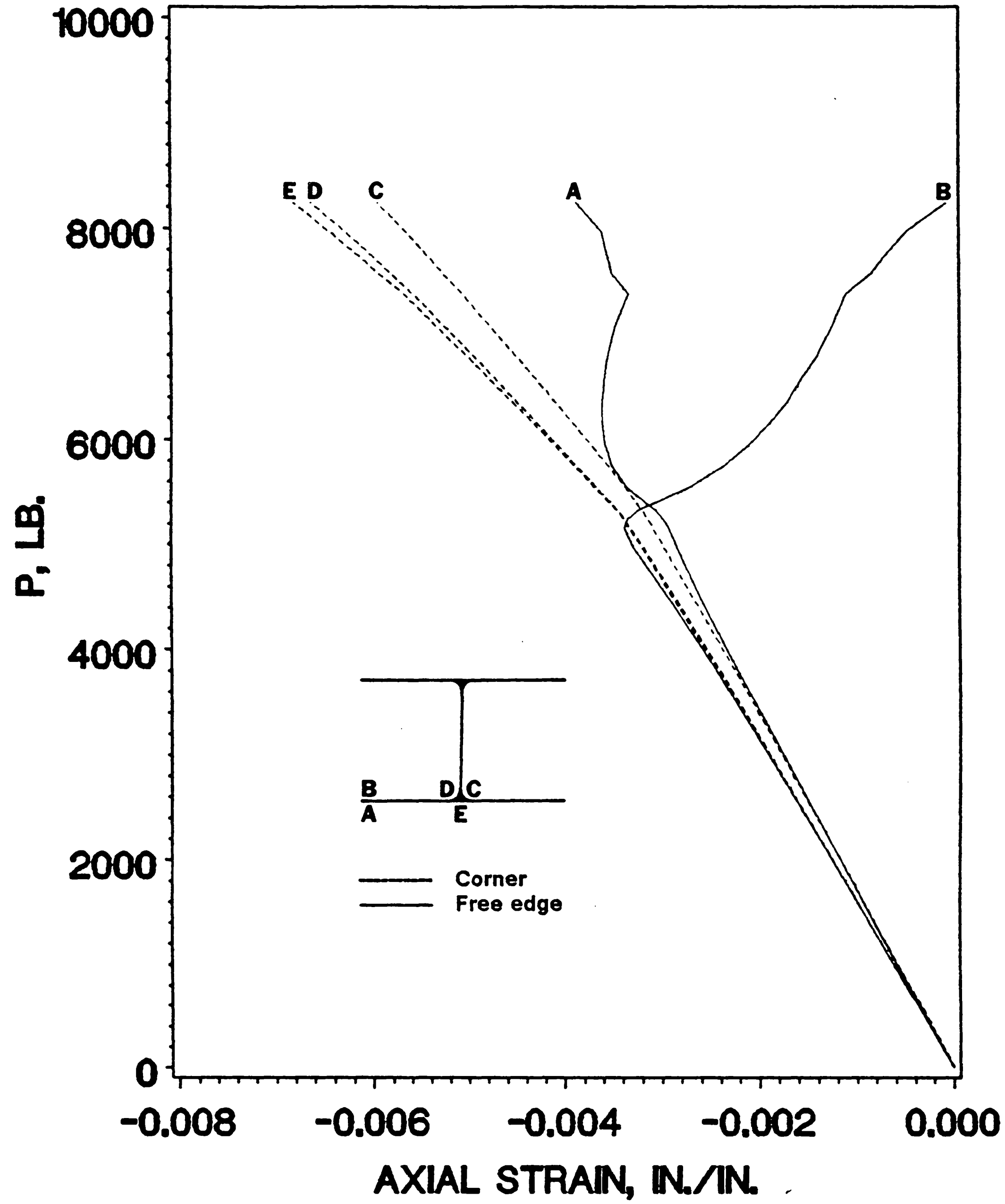

Figure 17. Flange free edge and corner axial strains, specimen I5: strain gage data at an axial location of 7*l*/16

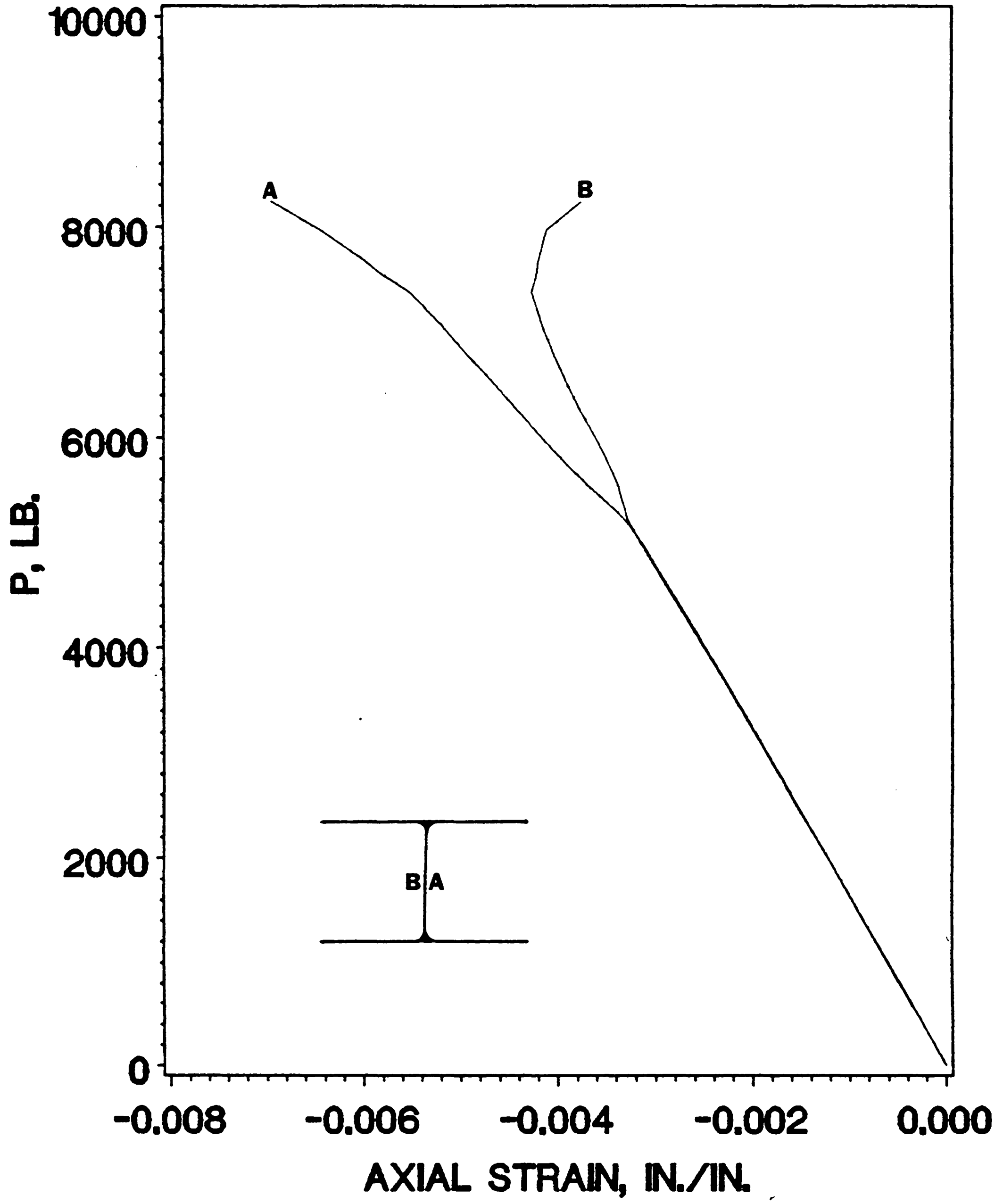

Figure 18. Web center axial strains, specimen I5: strain gage data at an axial location of $l/4$

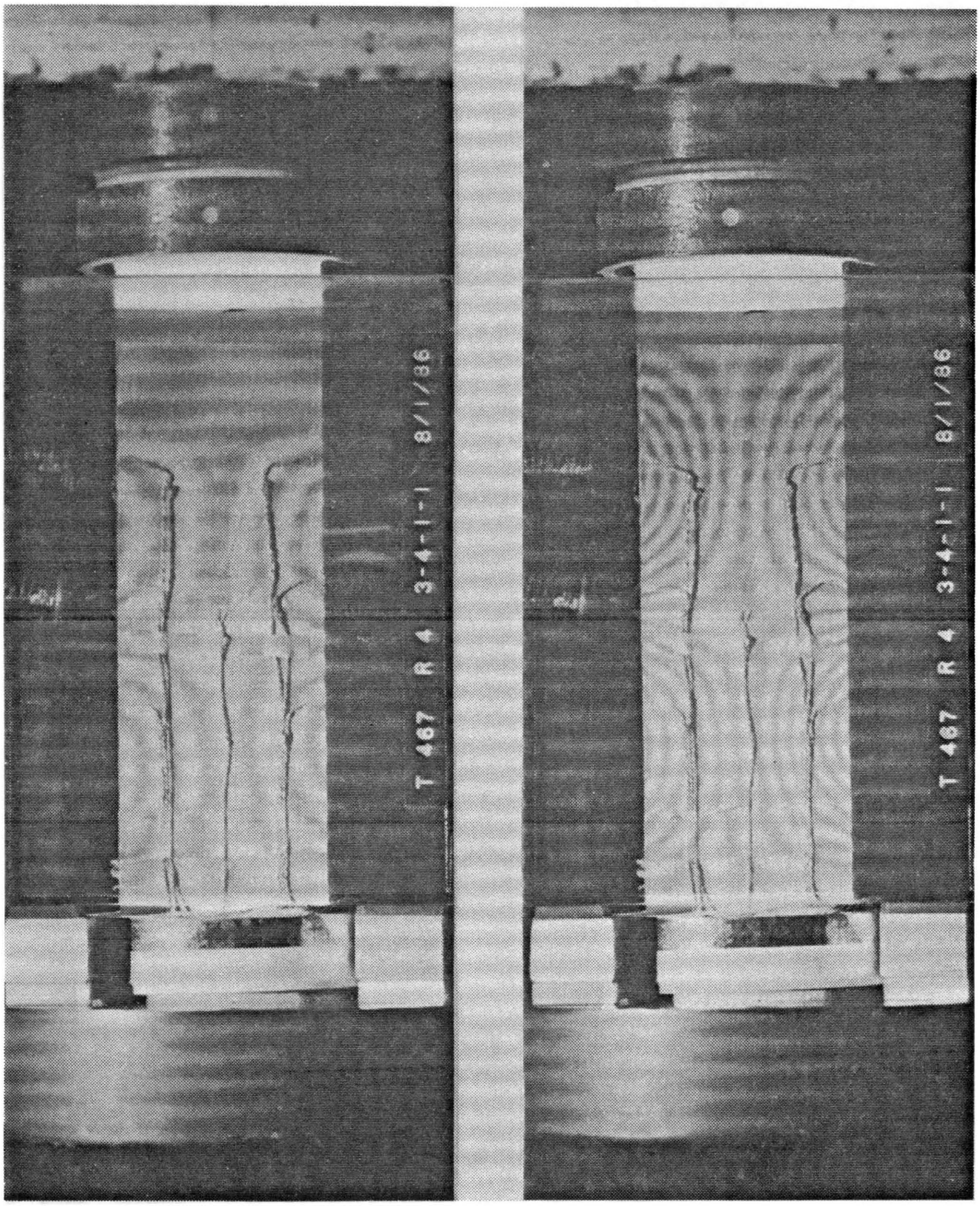

(a) $P = 15820$ lbs. (b) $P = 17340$ lbs.

Figure 19. Moire′ photographs of apparent mode change during testing of specimen I11

3.1.3 Effects of Geometric Parameters

3.1.3.1 Flange Width-To-Thickness Ratio

The flange width-to-thickness ratio combines b_f, r_c, and t into a single dimensionless parameter whose magnitude indicates the relative importance of interlaminar stresses in the specimen under consideration, as may be observed from Table 4. Of the three I-section specimens with the highest $(b/t)_f$, I1-I3, two of them experience their first damage event in a corner due to local compressive strength failure. One of the two specimens (I6 and I7) with the next highest $(b/t)_f$ also shows corner material strength damage, while the other exhibits a first damage event attributed to a flange free edge delamination. All of the remaining I-section specimens which show evidence of damage have flange width-to-thickness ratios smaller than 20; all of them appear to have a first damage event caused by some form of delamination, due to interlaminar stresses. This very significant observation implies that for this material system and stiffener configuration (I-section with 0° filler fibers in the corners), the corners of the column are critical failure regions which fail in an ultimate material strength mode for flange width-to-thickness ratios greater than approximately 20 to 25. For $(b/t)_f$ less than about 20, the flanges are the critical failure zones because of the increased likelihood of delamination. It appears that small values of $(b/t)_f$ are associated with increased interlaminar effects which cause delaminations to occur before the corners become loaded enough to cause a block compression failure. Increasing the flange width-to-thickness ratio, by either increasing b_f, decreasing r_c, or decreasing t leads to reduced interlaminar effects and a correspondingly lower probability for delaminations, which allows the corners to become heavily loaded and fail in a compressive ultimate strength mode. This correlation between $(b/t)_f$ and damage mode suggests why Rehfield and Reddy only observed flange free edge delamination failures in Refs. 9 and 10. The $(b/t)_f$ of all of their I-section specimens was less than six. The observations on the effect of flange width-to-thickness ratio on damage modes made here might not necessarily be extendable to other stiffener shapes and material systems, however. In particular, stiffener sections whose fabrication does not involve the insertion of a plug of 0° fibers into the corners might exhibit very different behavior from that observed in the I-section stiffeners of the present study. The absence of these "licorice sticks" would significantly change the stiffness and strength of the cross section. In addition, for stiffener cross sections with values of b_f/b_w smaller than the values corresponding to the I-section stiffeners of the current work ($b_f/b_w = 1.00$ and 0.60), new failure modes involving rupture of the web might be anticipated.

Buckling stresses σ_{cr} and crippling stresses σ_{cc} for the I-section specimens are tabulated in Table 5, along with flange width-to-thickness ratio and inner corner radius r_c. These are stresses in an average sense, obtained by dividing the appropriate experimental load by the original specimen cross-sectional area. Buckling stress is plotted versus $(b/t)_f$ in Figure 20, and a very clear relationship between the two is evident: a decrease in flange width-to-thickness ratio produces an increase in the average stress in the specimen at buckling. No such relationship is observed between the crippling stress and flange width-to-thickness ratio. To further illustrate the effect of $(b/t)_f$ on first damage type discussed in the last section, specimens which exhibited a first damage event occurring in a corner are plotted with a "C" in Figure 20, while specimens which showed evidence of a delamination first damage event are plotted with a "D".

3.1.3.2 Inner Corner Radius

The inner corner radius of an I-section column has a small effect on the flange width-to-thickness ratio, and in this way has a minor effect on the buckling stress and first damage mode observed, as already discussed. The most important result of changing r_c on an I-section specimen, however, is to significantly change the cross-sectional area of the corner region, thus altering the amount of 0° fiber filler material present. Changing the inner corner radius from 0.125 inches to 0.250 inches increases the amount of 0° fibers filling the corner region by almost 250 percent for an eight ply specimen. Reference to Table 5 shows that this increase in very stiff corner material manifests itself as a roughly 75 percent increase in average buckling stress and a 50 percent increase in average

Table 5. I-section average buckling and crippling stresses

Specimen designation	$(b/t)_f$[a]	Inner corner radius r_c, in.	Avg. buckling stress σ_{cr}, ksi[b]	Avg. crippling stress σ_{cc}, ksi[b]
I1	27.625	0.125	11.46	38.94
I2	27.625	0.125	10.64	39.30
I3	27.625	0.125	9.55	37.25
I4	15.125	0.125	29.10	43.82
I5	15.125	0.125	29.10	45.35
I6	24.500	0.250	19.50	62.80
I7	24.500	0.250	16.09	66.55
I8	12.000	0.250	52.72	61.68
I9	12.000	0.250	53.40	65.44
I10	13.563	0.125	33.28	44.33
I11[c]	13.563	0.125	28.67	-------
I12	13.563	0.125	27.75	40.97
I13[d]	7.3125	0.125	76.97	78.65
I14[d]	7.3125	0.125	76.57	76.67
I15	13.563	0.125	35.93	38.78
I16	13.563	0.125	32.62	35.11
I17	13.563	0.125	30.85	33.65
I18[d]	7.3125	0.125	87.29	88.97
I19[d]	7.3125	0.125	81.24	81.25

[a] Flange width-to-thickness ratio.

[b] Average stress is defined as the compressive load divided by the original specimen cross-sectional area.

[c] This specimen was not tested to failure.

[d] These specimens did not seem to fail in a crippling mode, so the last column actually displays an average failure stress for these cases.

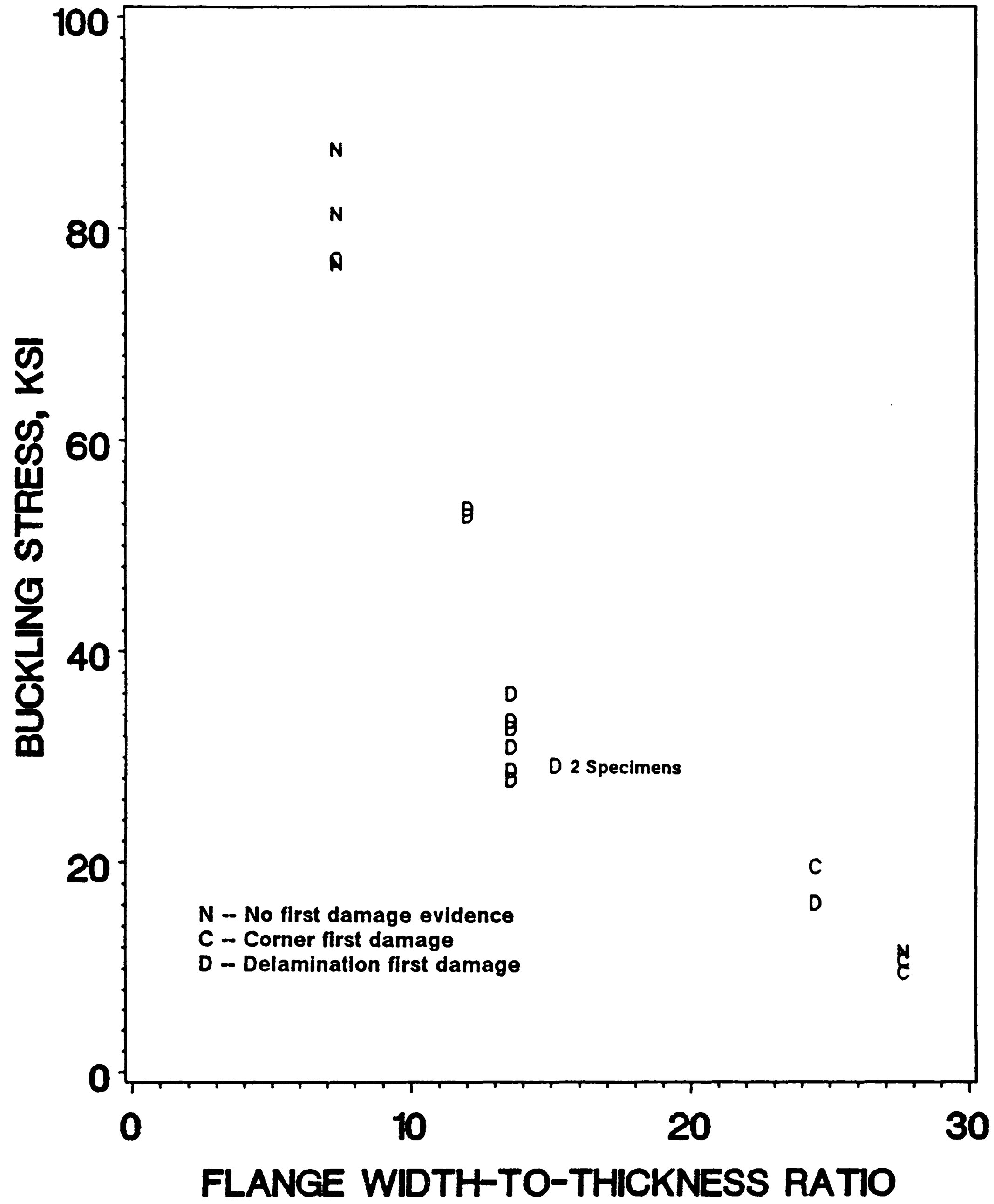

Figure 20. Buckling stress versus flange width-to-thickness ratio, specimens I1-I19

crippling stress for specimens with otherwise identical cross sections. Since the cross-sectional area occupied by the 0° corner filler material is a small proportion of the total specimen cross-sectional area (for all of the I-sections studied, the area of both stiffened corner regions combined never exceeded 30 percent of the total specimen cross-sectional area, and was usually much less), increasing the inner corner radius would appear to be a very efficient way to vastly improve I-section stiffener performance.

3.2 J-Section Specimens

3.2.1 Experimental Results

Fourteen J-section specimens were tested in this study. All of these specimens exhibited local buckling followed by crippling, and thus in the postbuckled state the corners of each specimen were subjected to large compressive membrane strains while the flanges experienced primarily bending strains. Failed specimens J1-J9 and J12 showed the typical characteristics of a crippled thin-walled graphite-epoxy stiffener: a fracture across the entire specimen cross section combined with a small number of flange free edge delaminations involving only one or a few plies. However, in some of these specimens the fracture surface was not perpendicular to the load; that is, different elements of the cross section of a specimen sometimes failed at slightly different axial locations, producing fractures that were skewed with respect to the cross-sectional plane. Such a case is shown in Figure 21. Failures of this type seemed to be the result of different buckling modes occurring in the various plate elements of the same specimen, due to the nonsymmetry of the J-section. The cap flange was in fact observed to buckle with a different number of halfwaves than the two attachment flanges, at least initially, on several occasions; for these specimens (as well as for some of the J-section specimens which had identical buckling modes in all elements), unique cap flange and attachment flange buckling loads were noted. Specimens J10, J11, J13, and J14 exhibited a failure similar to specimens I15-I17 (see Figure 11). A large delamination was observed, involving one ply interface only and running across the entire width of both attachment flanges and along a considerable portion of the length. An example of this type of crippling failure is shown in Figure 22; the lack of any other sort of damage in the attachment flanges, such as broken fibers, is quite conspicuous. The webs and cap flanges of these four specimens exhibited fractures involving broken fibers and delaminations like those seen in all the cross-sectional elements of specimens J1-J9 and J12 discussed above.

The load-shortening curves for the J-section specimens, which have been nondimensionalized in a manner identical to the I-section load-shortening curves, are shown in Figure 23. All specimens show behavior typical of specimens which buckle locally and then fail by crippling; the moire′ interferometry photographs from each test confirm that all of the J-section specimens did in fact buckle in a local mode. Damage events are evident in the load-shortening paths of several of the specimens. Table 6 gives the test results for the J-section specimens. The same types of results are shown in this table as were presented for the I-section specimens in Table 4. For the specimens in which significantly different buckling loads were noted for the cap flange and attachment flanges, two rows of information are given, the first labeled with an "A" for attachment flanges, and the second with a "C" for the cap flange. This procedure was also followed for specimens with different flange width-to-thickness ratios $(b/t)_f$ for the cap and attachment flanges.

3.2.2 Description of Damage Events

Damage initiation in each specimen seemed to occur at one of four locations within the cross section, as indicated in the last column of Table 6. Damage initiation in the corner between the web and cap flange is denoted by CC, a first damage event that occurs in the corner between the web and attachment flanges is denoted by AC, damage initiation at the free edge of the cap flange is

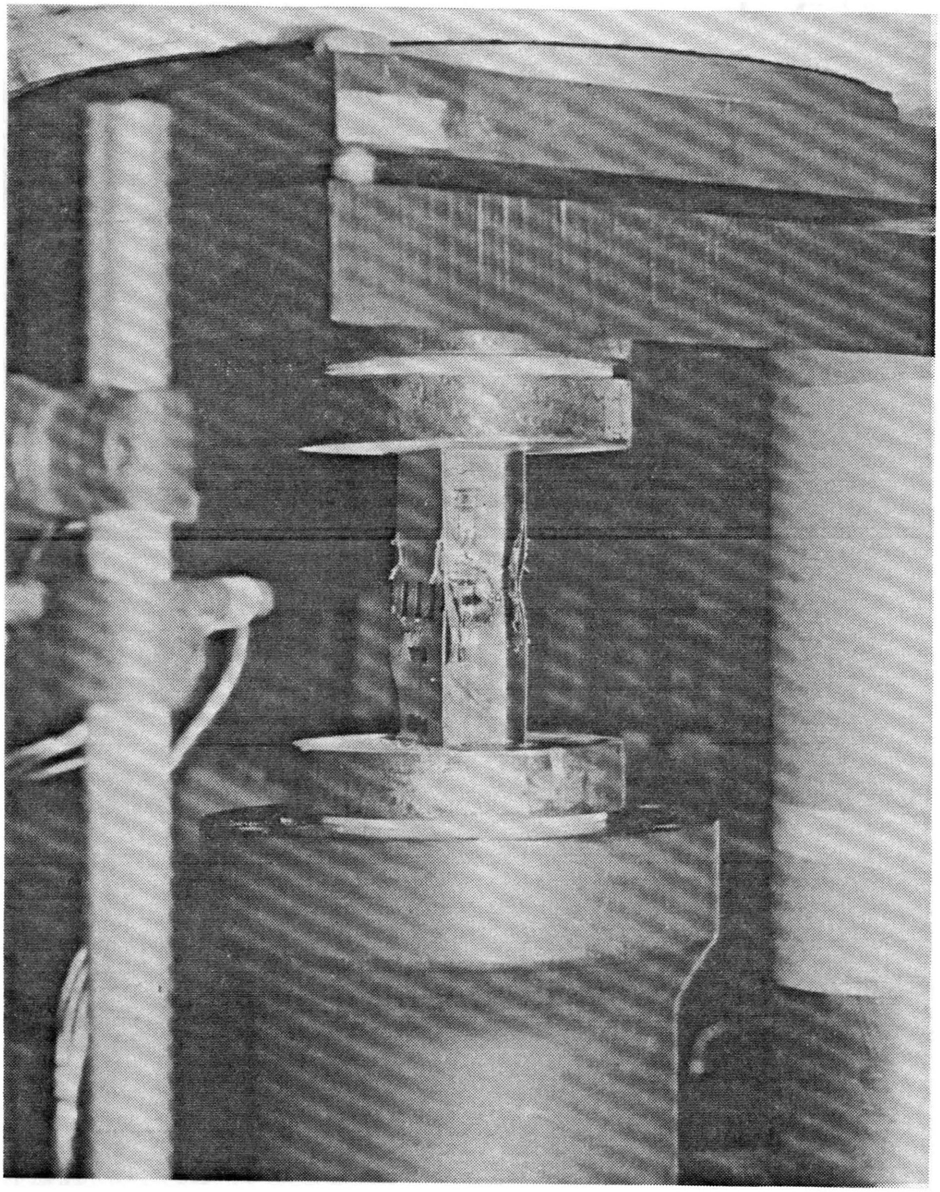

Figure 21. Crippled specimen J4 exhibiting axially uneven fracture

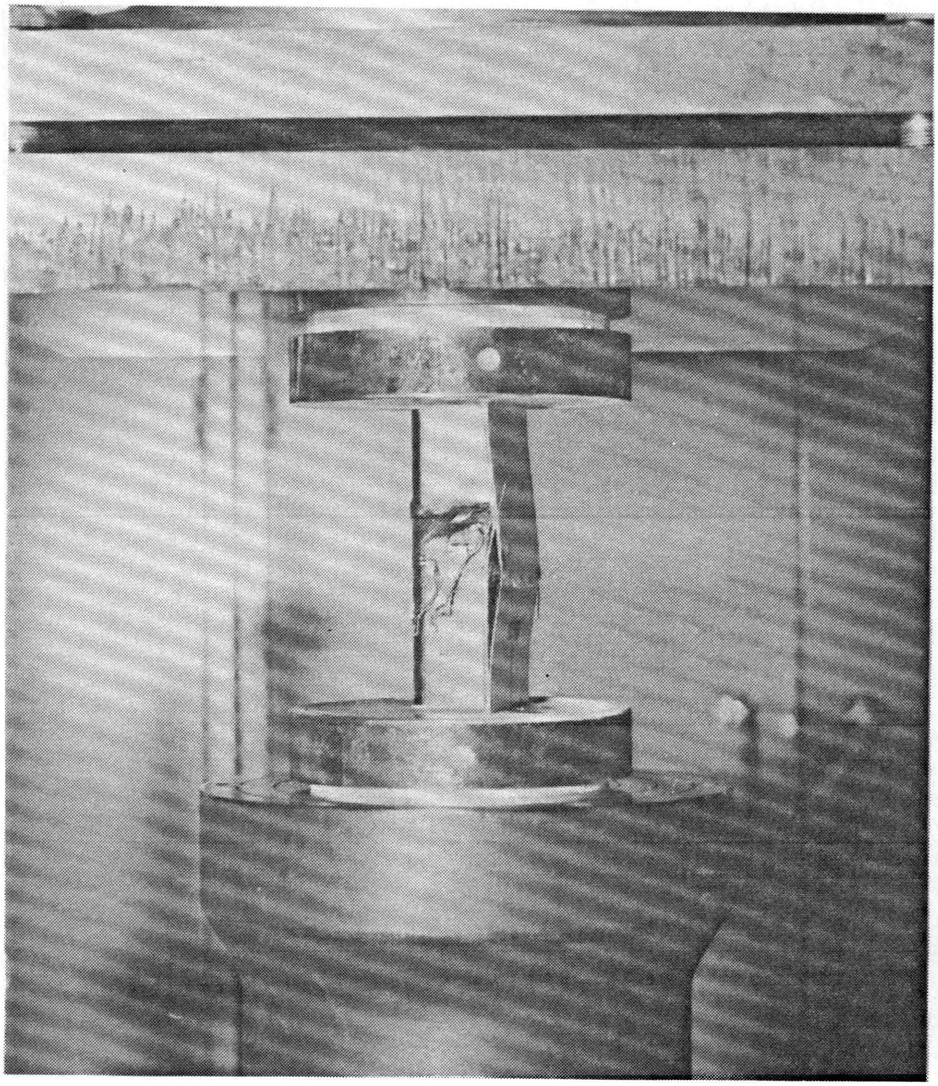

Figure 22. Crippled specimen J13: single delamination of a group of plies through both attachment flanges

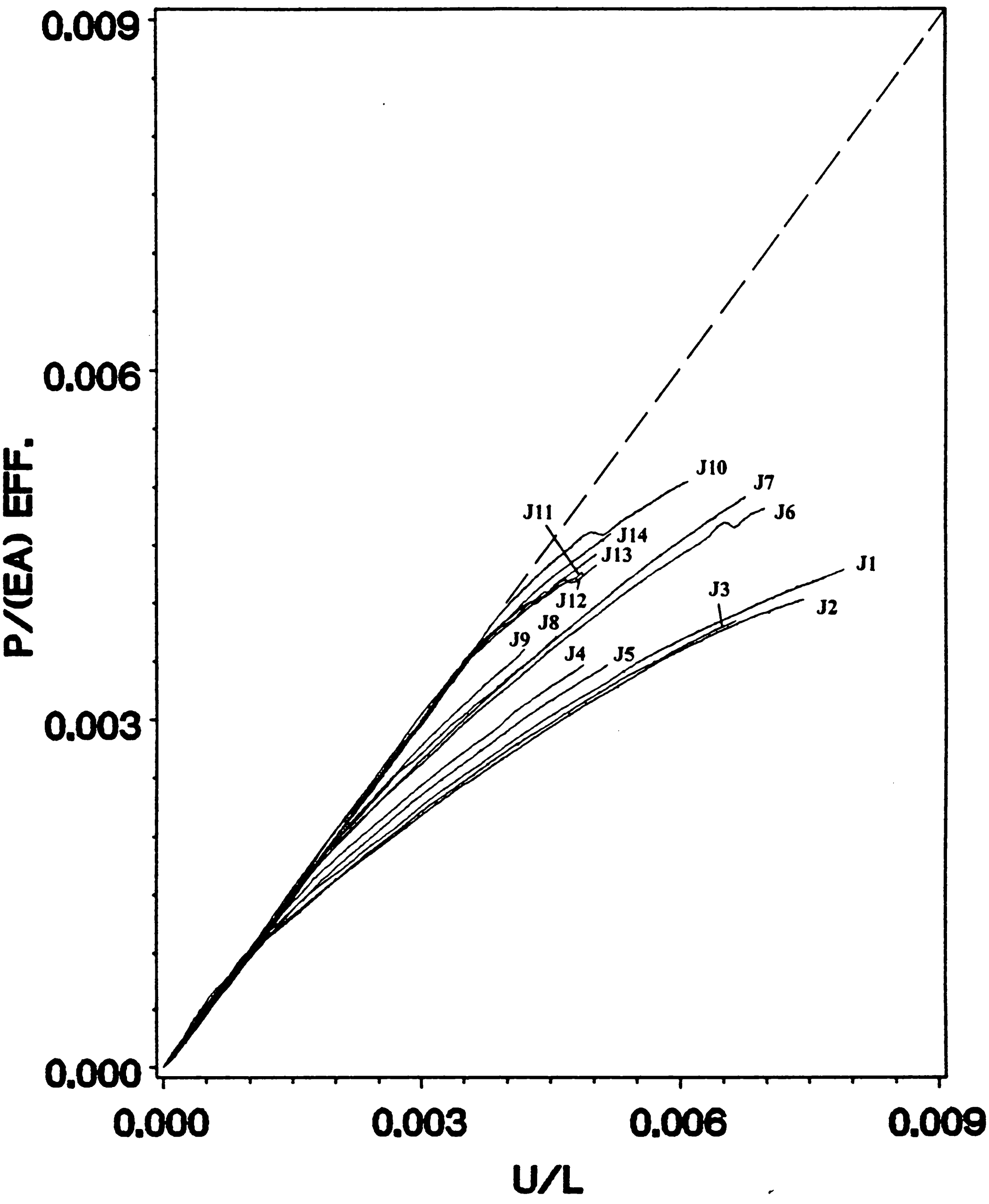

Figure 23. Dimensionless load-shortening plots for J-section specimens

Table 6. J-section experimental results

Specimen designation[a]		$(b/t)_f$[b]	Prebuckling stiffness K, lb./in.	Buckling load P_{cr}, lb.	Buckling strain[c] $\varepsilon_{x_{cr}}$	Crippling load P_{cc}, lb.	Location of first damage[d]
J1	A	27.625	300000	1768	-.0011	7723	N
	C	27.625					
J2	A	27.625	178570	1900	-.0011	7202	U
	C	27.625		1600	-.0009		
J3	A	27.625	117490	1880	-.0011	6335	CC
	C	27.625		1340	-.0008		
J4	A	27.625	300000	1790	-.0011	6252	CFD
	C	15.125		3160	-.0023		
J5	A	27.625	167600	1610	-.0010	5818	N
	C	15.125		2750	-.0020		
J6	A	24.500	425530	4320	-.0021	12281	AC
	C	24.500		3430	-.0016		
J7	A	24.500	227270	3360	-.0016	11166	CFD
	C	24.500		3070	-.0014		
J8	A	24.500	419580	4360	-.0022	9335	CFD
	C	12.000		6360	-.0035		
J9	A	24.500	220590	4250	-.0021	7958	N
	C	12.000		6710	-.0035		
J10	A	13.563	526790	12768	-.0042	15958	AFD
	C	13.563		12143	-.0040		
J11	A	13.563	306120	11063	-.0036	13251	AFD
	C	13.563					
J12	A	13.563	222320	10821	-.0036	13251	AFD
	C	13.563					
J13	A	13.563	546430	11500	-.0040	14500	AFD
	C	7.3125					
J14	A	13.563	310880	10610	-.0037	14311	U
	C	7.3125		10930	-.0038		

[a] Each specimen has two rows of information. The row marked "A" contains data for the attachment flanges in particular as well as global stiffener information such as K, P_{cc}, and location of first damage. The row marked "C" contains width-to-thickness ratio information for the cap flange, and buckling data for this flange if it is different from that for the attachment flanges.

[b] Flange width-to-thickness ratio.

[c] Average axial strain in the cross section at buckling.

[d] This column refers to the suspected nature and location of the first major damage event within the specimen as inferred from experimental data:

CC -- corner damage at web-cap flange junction
AC -- corner damage at web-attachment flange junction
CFD -- cap flange free edge delamination
AFD -- attachment flange free edge delamination
U -- location and nature of damage uncertain
N -- no damage observed prior to failure.

indicated by CFD, and a first damage event that begins at the free edges of one of the attachment flanges is denoted by AFD. Damage in the corners may take the form of a local compressive strength failure of the material due to the high compressive membrane strains which occur in the corner after buckling. Corner damage might also be initiated, though, by a delamination resulting from an increase, or opening, of the angle between a flange and the web during postbuckling. The opening of this angle creates tensile stresses in the curved fibers on the inside of the corner. These curved fibers in tension will try to straighten out, which causes interlaminar normal stresses in the corner and the possibility of a corner opening delamination. Although this corner opening delamination did not seem to be responsible for any of the corner damage in the I-section specimens, not enough data were available to distinguish whether local material failure or corner opening delamination caused the first damage reported for specimens J3 and J6 in Table 6. Damage events which occurred at the free edge of a flange were always due to delamination. In every specimen exhibiting first damage at the free edge of an attachment flange, the damage seems to occur in the same flange -- the one designated number 1 in Figure 1. In addition, the one case (specimen J6) of damage to the corner between the web and the attachment flanges in Table 6 seems to occur on the side of the corner connecting flange number 1 to the web. Finally, several specimens showed damage events of uncertain location and nature or yielded no evidence of damage at all, and these cases are also identified in Table 6.

Specimen J3 is the only J-section specimen in which first damage seemed to take place in the corner between the web and cap flange. Plots of the load versus axial strain for the back-to-back strain gages mounted in the corner nearest the cap flange at an axial location of about $l/3$ are shown in Figure 24. The corner first appears to be damaged at a compressive load of approximately 2800 lbs. No strain gages from any other element of the cross section or any other axial location exhibited discontinuities in the response before ultimate failure. Thus, the corner between the cap flange and the web is the likely location for the damage at 2800 lbs.; but from Figure 24, the axial strain level in the corner at this load is roughly -.0020 in/in, which is quite low. Plots of load versus displacement transducer data presented in Figure 25 may explain why damage occurred at such a low strain level. These plots show that at an axial location of $l/3$, flange displacements were somewhat irregular, being constant over a range of increasing loads, then decreasing, and eventually growing again with further load increases. The normal pattern for flange free edge displacements in an undamaged specimen is continuous and smooth growth, similar to that exhibited by the web of specimen J3 in Figure 25. The irregularities observed in Figure 25 suggest that the mode shapes present in the flanges of the buckled specimen were unstable. Since these irregularities begin to appear at loads below the 2800 lbs at which the damage in the corner near the cap flange occurred, it is possible that these irregular changes in the mode shapes caused the corner damage at 2800 lbs evident in Figure 24.

The only case in which damage first appears in the junction between the web and attachment flanges, or the "attachment corner," is specimen J6. Plots of data from the three axial strain gages mounted around the attachment corner at an axial location of $l/2$ are shown in Figure 26. The gages marked A and B are inside corner gages, and strain gage C is positioned on the attachment flanges over the web. Plots B and C show a discontinuity and a strain increase at a load of 12000 lbs; strain gage A shows a smaller discontinuity at this load than gages B and C. The implication is that some small damage event occurred at a load of 12000 lbs near gage position A, causing a redistribution of load into other undamaged areas of the corner, and thus an increase of compressive membrane strain in locations B and C. Plots of axial back-to-back strain gage data from the attachment flange which connects to the web at the position of strain gage A are shown in Figure 27, and support the idea that damage took place in this corner. At 12000 lbs, the free edge gages show a simple increase in bending with no significant change in the state of membrane strain. In contrast, the gage pair at the center of the flange, which is a position closer to the corner, exhibits a decrease in bending and a drop in the membrane strain, indicative of a load redistribution due to nearby damage.

Specimen J7 will serve as a representative example of those J-section specimens (J4, J7, and J8) whose first damage event is suspected to have been a free edge delamination of the cap flange. Back-to-back axial strain gage data from the free edge of the cap flange at an axial location of $l/3$

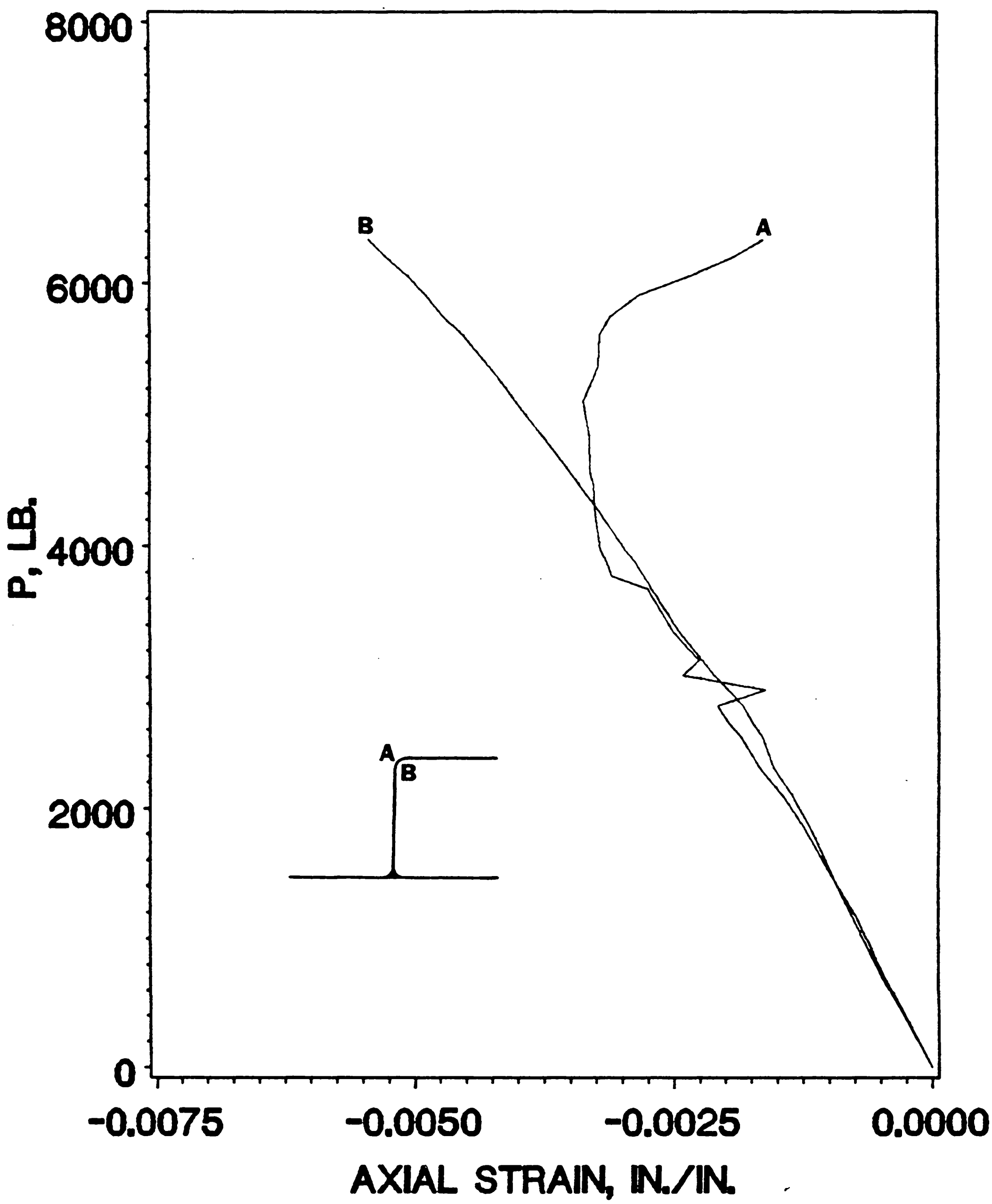

Figure 24. Cap corner axial strains, specimen J3: strain gage data at an axial location of $l/3$

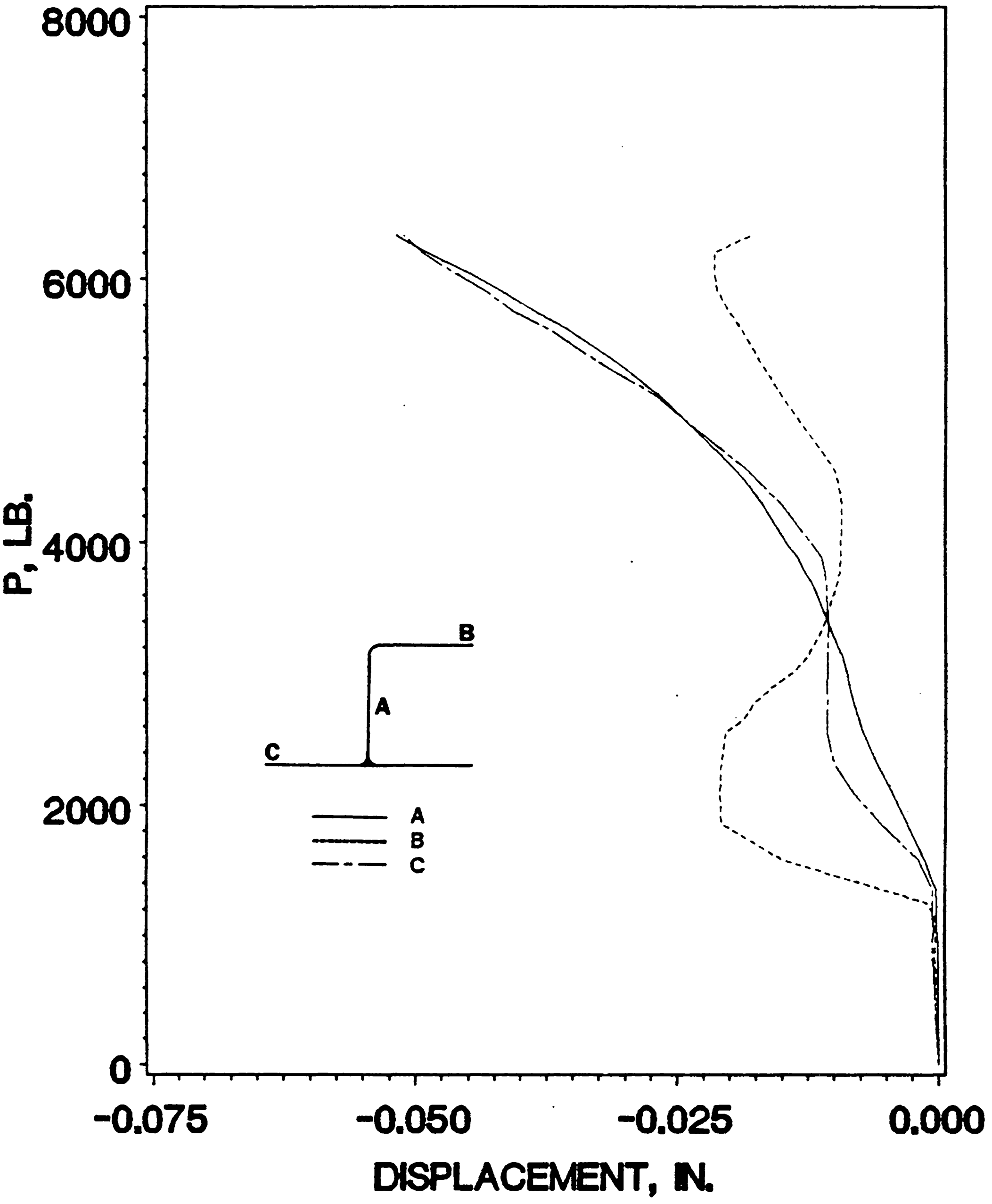

Figure 25. Flange and web displacements, specimen J3: displacement transducer data at an axial location of *l*/3

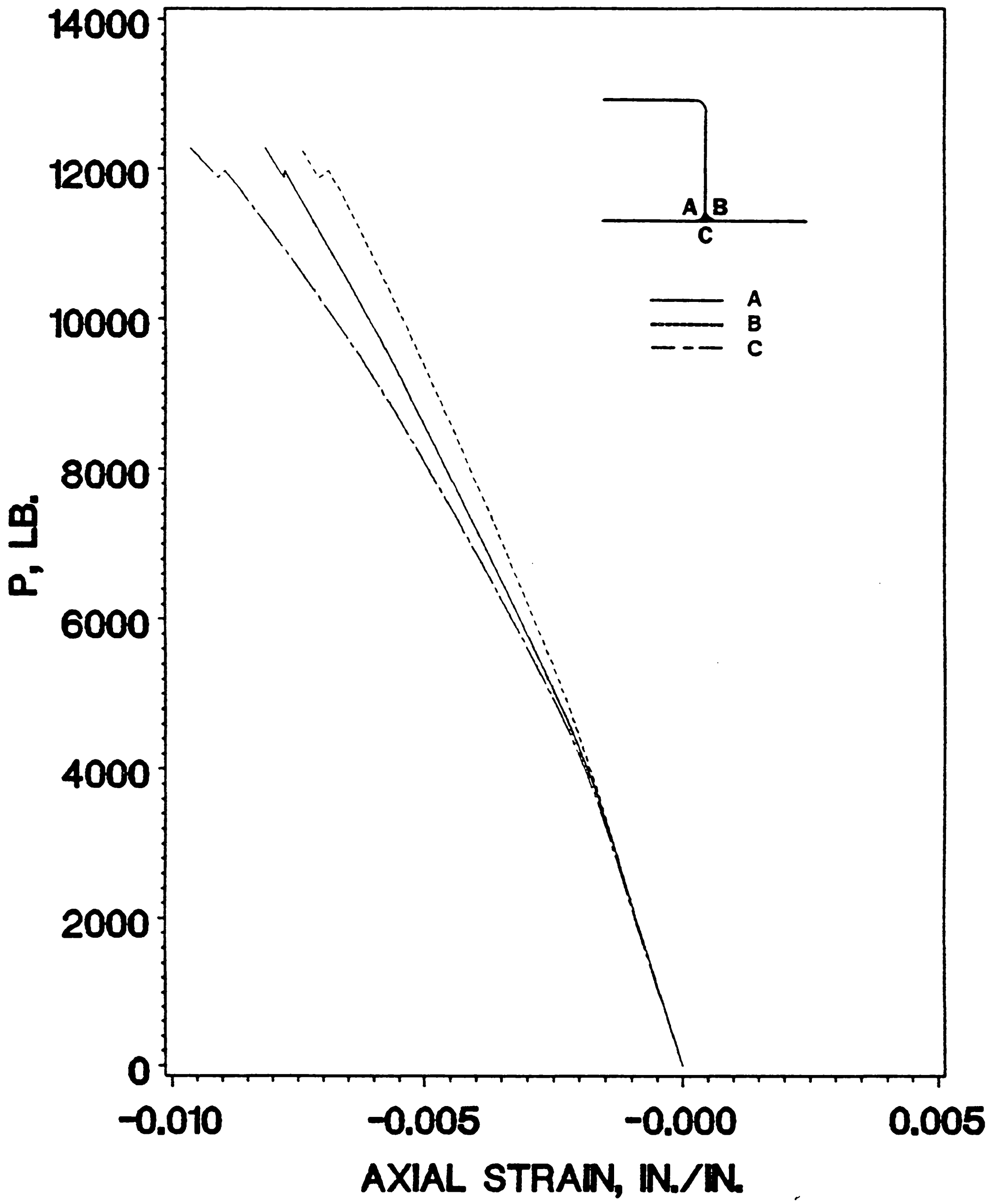

Figure 26. Attachment corner axial strains, specimen J6: strain gage data at an axial location of *l*/2

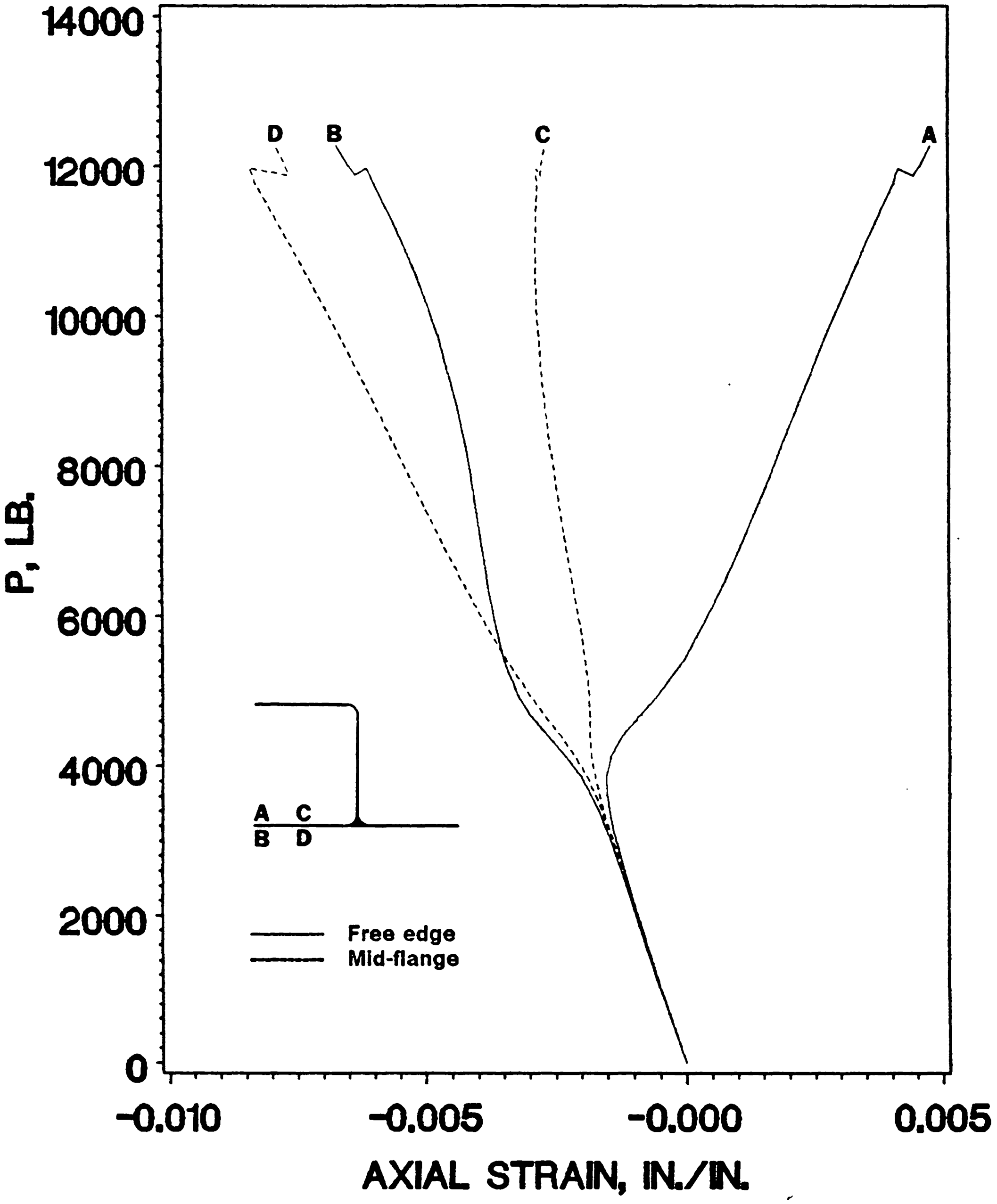

Figure 27. Flange center and free edge axial strains, specimen J6: strain gage data at an axial location of $l/2$

are presented in Figure 28. A discontinuity, indicating damage, is apparent at a load of approximately 9000 lbs. Plots of data from the axial strain gage pair mounted in the corner nearest the cap flange at an axial position of $2l/3$, also given in Figure 28, show no evidence of this damage. If the discontinuity noted in the cap flange gages were due to damage in the corner, it would be logical to expect evidence of this damage to show up in the data from the corner, regardless of the axial position of the corner gages. Since no such evidence is present in the corner data plotted in Figure 28, the damage which occurred at 9000 lbs probably did not initiate in the corner. Plots of lateral strain data from a back-to-back gage pair located at the center of the web and at an axial position of $l/3$ are shown in Figure 29. Damage evidence in the form of a lateral bending increase is visible, but the magnitude of this bending increase is smaller than that of the axial bending increase in the cap flange. This web bending increase seems to represent the response of the web to a loss of some of the rotational restraint exerted upon it by the cap flange, due to the delamination in the cap flange. Axial and lateral strain gage data from all other cross section elements at all axial locations show very small or nonexistent discontinuities at a load of 9000 lbs, which further supports the assertion that the damage seen at this load took place in the cap flange. A final interesting observation on this specimen may be made by referring to Figures 28 and 29. Note that a second damage event is visible in the cap flange free edge axial gages and, to a lesser extent, in the web center lateral gages at a load of about 10500 lbs. The description given above of the stiffener behavior seen during the first damage event remains applicable in every aspect to this second damage event. Thus, it would seem that this second event constitutes a growth of the first cap flange delamination.

To illustrate the J-section stiffener behavior which would lead to the conclusion that first damage was an attachment flange delamination, specimen J13 will be discussed. Back-to-back axial strain gage data from the free edge and the center of the flange designated number 1 in Figure 1 are plotted in Figure 30. All gages on this specimen are at an axial location of $l/2$. A damage event is evident at a load of approximately 12500 lbs. This event causes a strain response discontinuity of considerably smaller magnitude in the other attachment flange, and negligible discontinuities appear in the strain gage data from the web, from the corner nearest the cap flange, and from the cap flange at

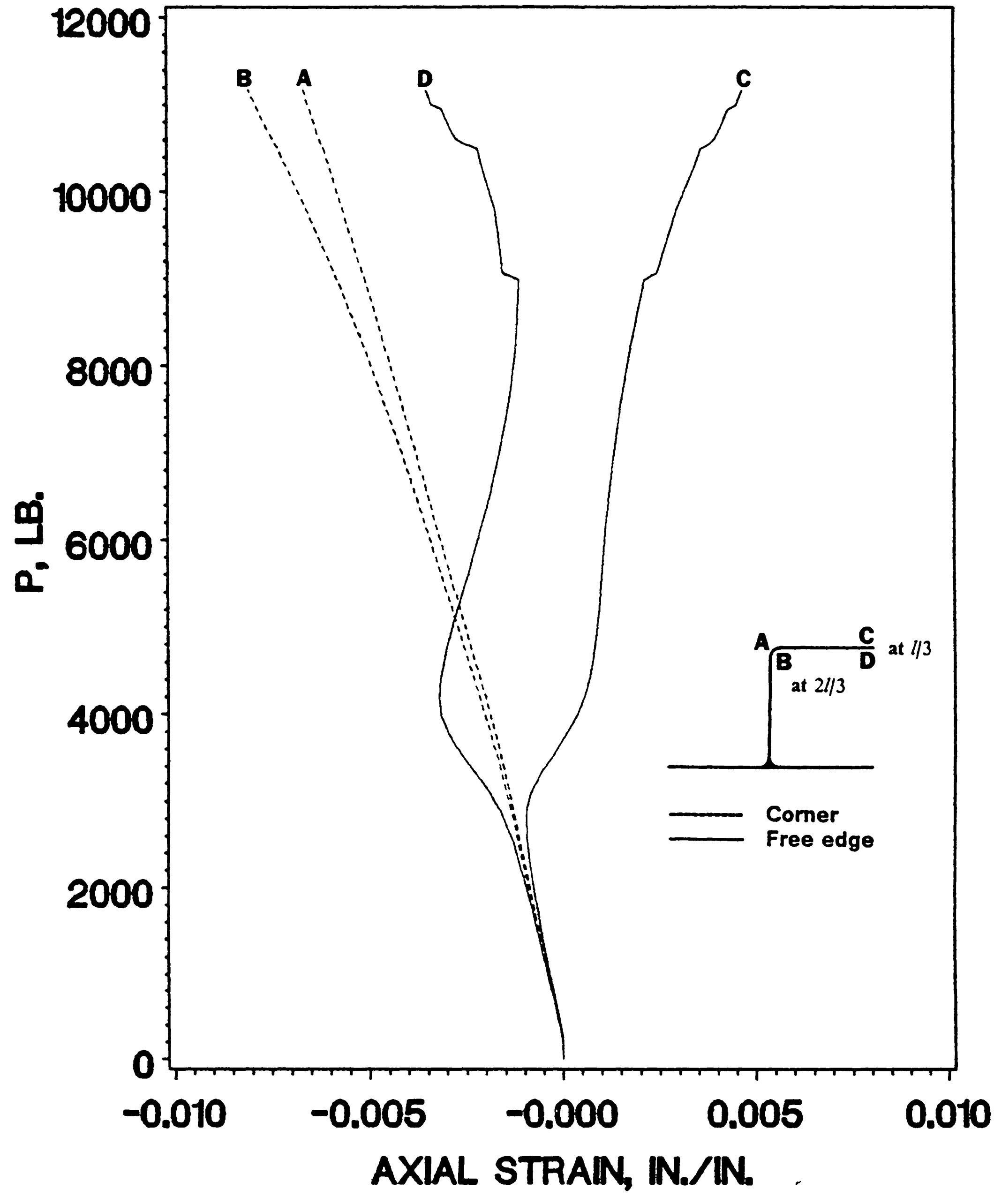

Figure 28. Cap flange free edge and cap corner axial strains, specimen J7: cap flange gages at *l*/3, cap corner gages at 2*l*/3

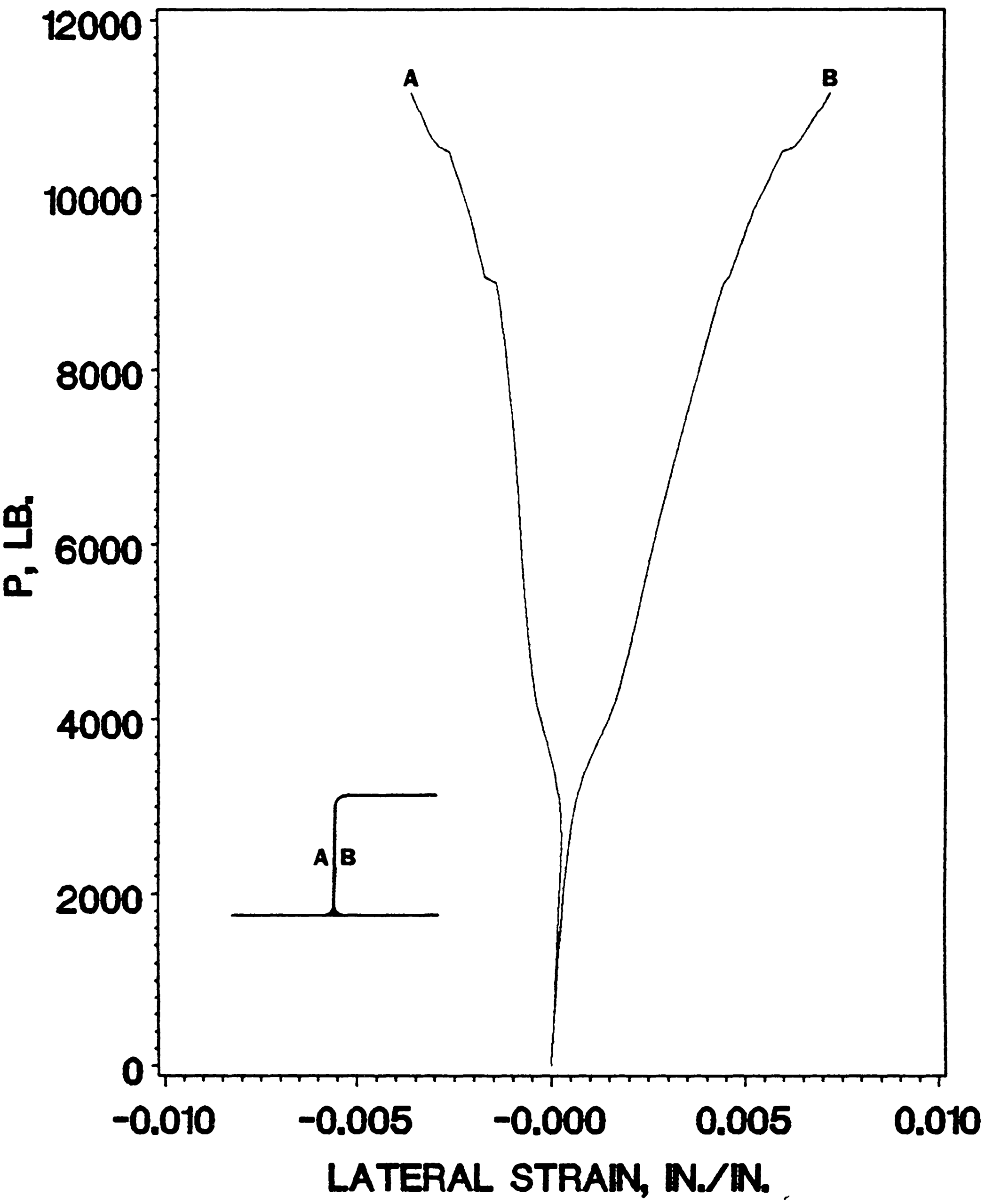

Figure 29. Web center lateral strains, specimen J7: strain gage data at an axial location of *l*/3

the same load. Axial strain data from the three gage positions around the attachment corner are plotted in Figure 31. Gages A and B are inner corner gages, while C was positioned on the attachment flanges over the web junction. Gages A and C show no evidence of damage at 12500 lbs, while the gage in position B exhibits a slight increase in compressive strain, indicative of an increase in loading in this part of the corner. Such an increase in strain and load is consistent with damage occurring in nearby flange number 1. The large magnitude of the discontinuity observed in this flange (Figure 30) when compared to the attachment corner (Figure 31) confirms that this first damage event was an attachment flange free edge delamination.

3.2.3 Effects of Geometric Parameters

3.2.3.1 Flange Width-To-Thickness Ratio

By referring to Table 6, it may be seen that the same general relationship that exists between the flange width-to-thickness ratio $(b/t)_f$ and first damage event for the I-sections also exists for the J-section specimens: the magnitude of $(b/t)_f$ serves as an indicator of the type of damage that will be observed. For some of the J-sections, though, there is the added complication of two different flange width-to-thickness ratios, one for the cap flange and one for the attachment flanges. For this reason, the J-section specimens are best discussed in four groups.

The first group, which includes specimens J1-J3, J6, and J7, is made up of those specimens that have identical flange width-to-thickness ratios in all three flanges of the cross section and satisfy $(b/t)_f > 20$. Both instances of first damage occurring in one of the corners are found in this group (J3 and J6); the group also contains two inconclusive cases (J1 and J2) and one case of flange delamination. It would seem, then, as was observed for the I-sections, that large values of $(b/t)_f$ (i.e., $(b/t)_f$ greater than 20 or 25) imply an increased probability of damage initiation in the corners. The second group of J-section specimens consists of those columns whose attachment flange width-to-

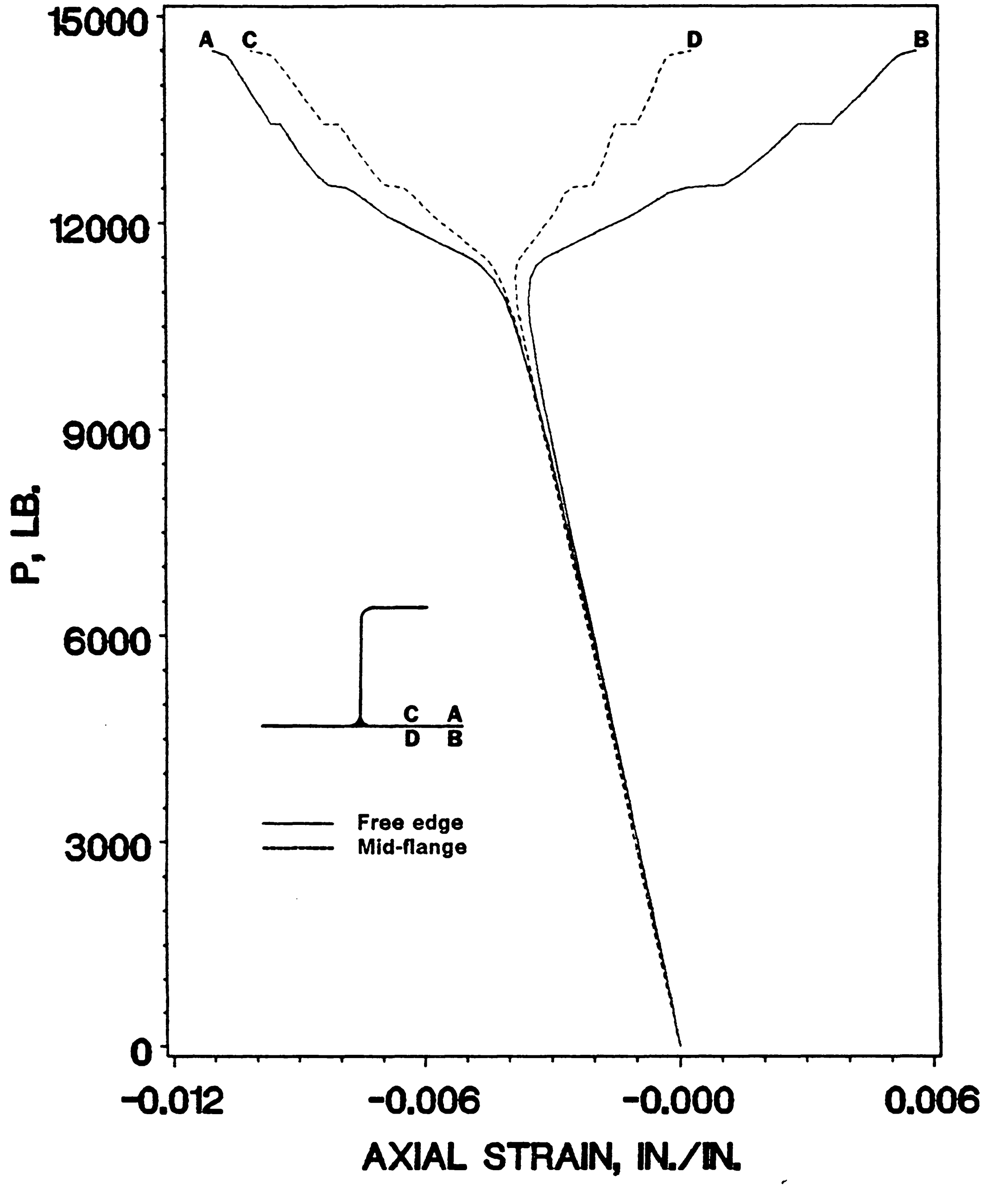

Figure 30. Flange center and free edge axial strains, specimen J13: strain gage data at an axial location of *l*/2

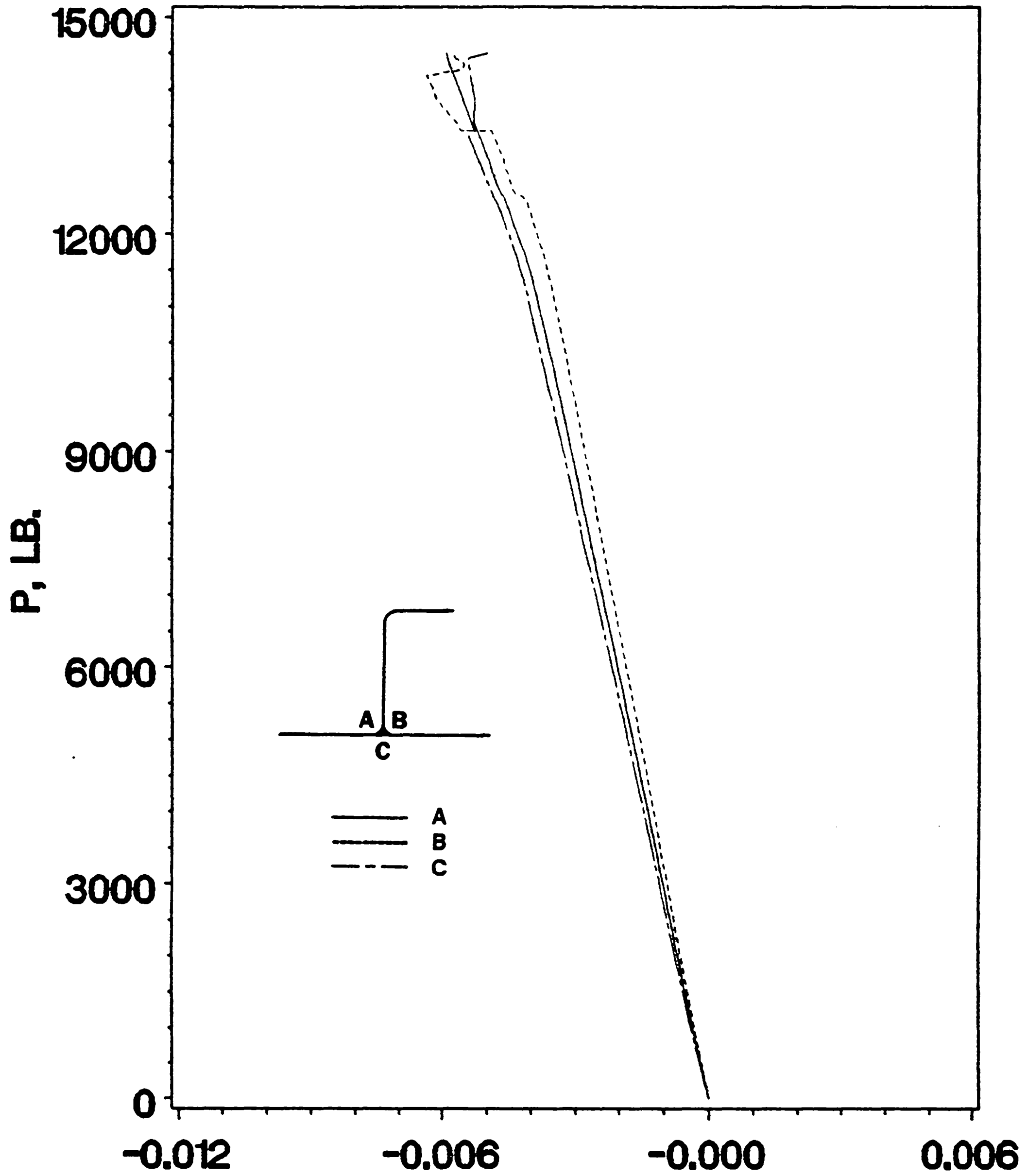

Figure 31. Attachment corner axial strains, specimen J13: strain gage data at an axial location of $l/2$

thickness ratios remain greater than 20, but whose cap flange width-to-thickness ratios are less than 20 and greater than ten, and includes specimens J4, J5, J8, and J9. Two of these four specimens exhibit cap flange delamination as the first damage event, and two show no evidence of damage prior to catastrophic failure. Thus, again consistent with earlier observations, a reduction of $(b/t)_f$ (specifically, the cap flange width-to-thickness ratio) leads to a greater likelihood of damage initiation in a free edge delamination mode (in the cross-sectional element in which $(b/t)_f$ was reduced).

The third group (specimens J10-J12) includes once again specimens in which the width-to-thickness ratios of all three flanges are identical; but in this case, $(b/t)_f < 20$. All three specimens show evidence of damage initiation by free edge delamination, consistent with the low value of $(b/t)_f$. In addition, the damage for all three specimens occurs in the attachment flange identified as number 1 in Figure 1, and always seems to be very closely followed by a second damage event in the cap flange. Evidently, at least for this group of specimens, flange number 1 is for some reason the most heavily loaded in bending, followed by the cap flange, while the remaining attachment flange exhibits somewhat less bending deformation, implying smaller interlaminar stresses and thus a decreased likelihood of delamination. In general, experimental strain data support this conclusion. The fourth group contains two specimens (J13 and J14) whose attachment flange width-to-thickness ratios are less than 20, but whose cap flange width-to-thickness ratios are smaller still, on the order of seven. This small value of $(b/t)_f$ for the cap flange does not, however, cause the first damage event to occur in the cap flange, as might at first be expected based on the I-section specimen results discussed earlier. In fact, the only first damage which could be distinguished in this group was due to free edge delamination of attachment flange number 1 in specimen J13. The data accumulated during both of these tests, though, indicate that the cap flange remained almost completely free of out-of-plane deflection. The cap flanges of these two specimens were heavily loaded in membrane strain, and exhibited very little bending; this lack of bending deformation explains why first delamination damage took place in an attachment flange.

What happened to the cap flanges in the J-section specimens in the fourth group is similar to what occurred in the short column I-section specimens I13, I14, I18, and I19. Reference to Tables 4 and

6 shows that the flange width-to-thickness ratio for all of the flanges of the four short column I-sections is the same as $(b/t)_f$ for the cap flanges of specimens J13 and J14. Clearly, for a very small flange width-to-thickness ratio ($(b/t)_f$ less than about eight), the flange acts more like a stiffening bulb on the end of the web, carrying significant amounts of membrane load, but hardly experiencing any bending at all. Thus, to summarize for both the I- and J-section specimens, for a flange with $(b/t)_f$ between approximately ten and twenty, the likelihood of damage initiation due to free edge delamination in that flange is high. For a flange with $(b/t)_f$ greater than about 25 or less than about eight, damage initiation at some other location in the stiffener, either in a corner or in a different flange with $10 < (b/t)_f < 20$, seems to be more likely.

The average buckling stress and average crippling stress for each J-section specimen are given in Table 7. Inner corner radius and an average flange width-to-thickness ratio $(b/t)_{f_{avg}}$ are also tabulated. The quantity $(b/t)_{f_{avg}}$ is the arithmetic mean of the width-to-thickness ratios of the three flanges in each specimen cross section. The average flange width-to-thickness ratio was found from experience to provide better correlation of a global column response such as average buckling stress than did a simple cap flange or attachment flange width-to-thickness ratio in cases where the cap flange width-to-thickness ratio and attachment flange width-to-thickness ratio were different. (Note that the average flange width-to-thickness ratio and the actual flange width-to-thickness ratio are identical for I-section specimens.) Figure 32 is a plot of the average buckling stress versus $(b/t)_{f_{avg}}$, and exhibits the same trend as Figure 20 for the I-section columns: increased $(b/t)_{f_{avg}}$ implies lower stress in the specimen at buckling. As before, crippling stress does not correlate well with the flange width-to-thickness ratio.

3.2.3.2 Inner Corner Radius

Inner corner radius has a small effect on the type of first damage observed in the J-section specimens through the flange width-to-thickness ratio parameter defined in equation (3.4). As with the

Table 7. J-section average buckling and crippling stresses

Specimen designation	$(b/t)_{f_{avg}}$[a]	Inner corner radius r_c, in.	Avg. buckling stress σ_{cr}, ksi[b]	Avg. crippling stress σ_{cc}, ksi[b]
J1	27.625	0.125	8.69	37.97
J2	27.625	0.125	7.87	35.41
J3	27.625	0.125	6.59	31.15
J4	23.458	0.125	9.76	34.09
J5	23.458	0.125	8.78	31.72
J6	24.500	0.250	15.49	55.47
J7	24.500	0.250	13.87	50.43
J8	20.333	0.250	21.65	46.35
J9	20.333	0.250	21.10	39.51
J10	13.563	0.125	30.53	40.12
J11	13.563	0.125	27.81	33.31
J12	13.563	0.125	27.20	33.31
J13	11.480	0.125	32.14	40.53
J14	11.480	0.125	29.65	40.00

[a] The quantity $(b/t)_{f_{avg}}$ is the arithmetic mean of the width-to-thickness ratios, $(b/t)_f$, of the three flanges in each J-section specimen.

[b] Average stress is defined as the compressive load divided by the original specimen cross-sectional area.

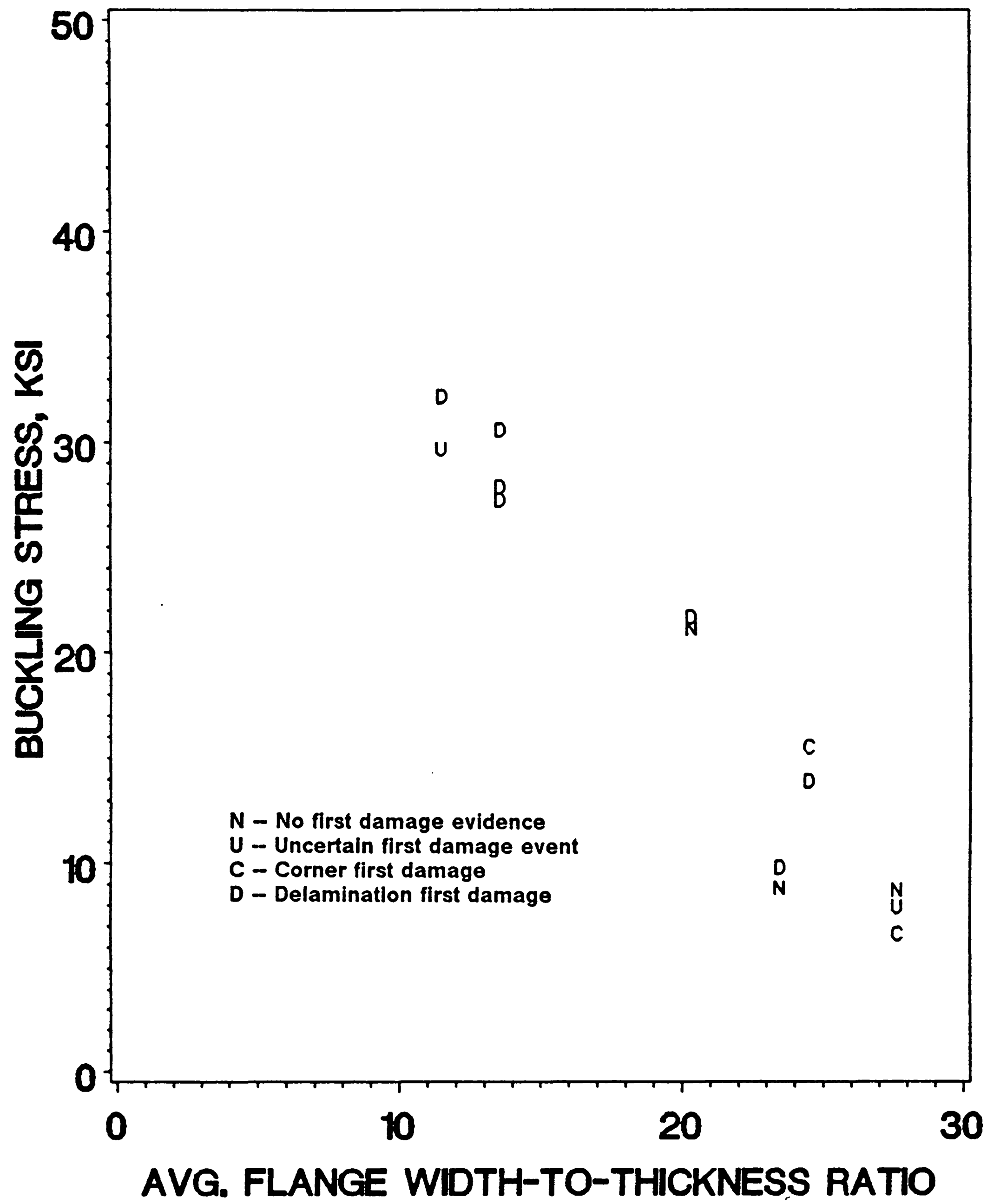

Figure 32. Buckling stress versus average flange width-to-thickness ratio, specimens J1-J14

I-section specimens, though, the most significant effects of the corner radius are upon the average buckling stress and the average crippling stress.

Within the range of r_c considered, increasing the corner radius results in a greater average specimen stress at buckling. This is, in part, due to the additional 0° fiber material needed to fill the larger attachment corner area produced by an increased inner corner radius. This added material provides extra specimen stiffness which increases the buckling load. It does not seem, however, that added material alone can account for the increase in buckling stress observed in Table 7 for a doubling of inner corner radius with all other geometric parameters held unchanged. By comparing specimens J1-J3 with J6 and J7, and J4 and J5 with J8 and J9, an average increase in buckling stress of 110 percent is obtained. The two filled corner regions of the I-section specimens make up a larger proportion of total specimen cross-sectional area than does the one filled attachment corner of the J-section specimens; yet, an identical increase in r_c produces a 75 percent increase in σ_{cr} in the I-sections versus a 110 percent jump in σ_{cr} for the J-section columns. Evidently, added attachment corner material is not the only mechanism which increases the average buckling stress in J-section specimens with an inner corner radius of 0.250 inches. Logically, this additional buckling resistance must be coming from the increase in r_c of the corner at the cap flange connection to the web. This corner, rather than being a filled region like the attachment corner, is basically made of laminate shaped into one quarter of a circular cylinder. Thus, for the range of r_c considered, an increase in the radius of this cylindrical corner (while keeping the thickness constant) also seems to be a factor contributing to a greater average stress in the stiffener at buckling.

An increase in r_c from 0.125 inches to 0.250 inches in a J-section specimen, all other parameters remaining constant, also produces a greater average crippling stress, as may be seen in Table 7. However, the relatively modest increase in σ_{cc} observed (approximately 40 percent on average) is similar to that seen in Table 5 for the I-section specimens (roughly 50 percent on average), and is thus apparently mostly due to the additional amount of 0° fiber corner filler material implied by such an inner corner radius increase. As with the I-section specimens, increasing r_c in a J-section column seems to be an efficient way to improve stiffener buckling and crippling performance.

3.3 Channel and Zee Section Specimens

3.3.1 Experimental Results

Two channel and one zee section specimens were tested in this study. In addition, limited information was available about the graphite-epoxy crippling specimens studied in Ref. 8, and so these specimens are at times included in the discussion. The specimen designation, cross section type, flange width, inner corner radius, layup, and length for each of the specimens which failed in a crippling mode in Ref. 8 is given in Table 8. These specimens were fabricated from the same material system, AS4/3502, and formed from the same three layups as the specimens in the current program; the definitions of the various geometric parameters are shown in Figure 1.

Dimensionless load-shortening curves for specimens C1, C2, and Z1 are presented in Figure 33, and for the specimens from Ref. 8 in Figures 34 and 35. The curves in Figure 33 were nondimensionalized in the same way as the load-shortening data for the I- and J-section stiffeners of the current work. The load-shortening plots from Ref. 8 were nondimensionalized by using the exposed length, *l*, of each specimen, rather than the total length *L*. All of the specimens exhibit load-shortening behavior typical of thin-walled columns which buckle locally and then cripple. All channel and zee specimens from both studies were confirmed to have buckled locally by examination of photographs of the moire′ fringe patterns, and every failed specimen showed the fracture through the cross section accompanied by flange free edge delaminations along one or a few ply interfaces that is typical of crippling failure in most graphite-epoxy columns.

Experimental results for the channel and zee section specimens are presented in Table 9. No detailed first damage analysis was performed for the Ref. 8 specimens. The categories of information presented are identical to those used earlier for the I- and J-section specimens in Tables 4 and 6, respectively, and the information was derived from the raw experimental data in the same way.

Table 8. Channel and zee section specimens from Ref. 8

Specimen designation[a]	Cross section	Flange width b_f, in.	Corner radius r_c, in.	Layup[b]	Gage length l, in.
C3 (1-3) C1-3	Channel	1.25	0.125	L8	3.0
C4 (1-4) C1-4	Channel	1.25	0.125	L8	4.0
C5 (1-5) C1-5	Channel	1.25	0.250	L8	4.0
C6 (1-6) C1-6	Channel	1.25	0.125	L8	18.0
C7 (1-7) C1-7A	Channel	1.25	0.125	L16A	4.0
C8 (1-8) C1-8B	Channel	1.25	0.125	L16B	4.0
C9 (1-9) C1-9	Channel	0.75	0.125	L8	12.0
Z2 (1-11) Z1-2	Zee	1.25	0.250	L8	3.0
Z3 (1-12) Z1-3	Zee	1.25	0.125	L8	4.0
Z4 (1-13) Z1-4	Zee	1.25	0.250	L8	4.0
Z5 (1-14) Z1-5	Zee	1.25	0.250	L8	23.0
Z6 (1-15) Z1-6A	Zee	1.25	0.125	L16A	4.0
Z7 (1-16) Z1-7B	Zee	1.25	0.125	L16B	4.0
Z8 (1-17) Z1-8	Zee	0.75	0.250	L8	15.0

[a] All specimens have a web width, b_w, of 1.25 inches, and are made from AS4/3502 graphite-epoxy. Specimen designations in parentheses are those used in Ref. 8.

[b] Layup L8 denotes $[\pm 45/0/90]_S$, layup L16A denotes $[\pm 45/0/90]_{2S}$, and layup L16B refers to $[\pm 45/\mp 45/90/0_3]_S$.

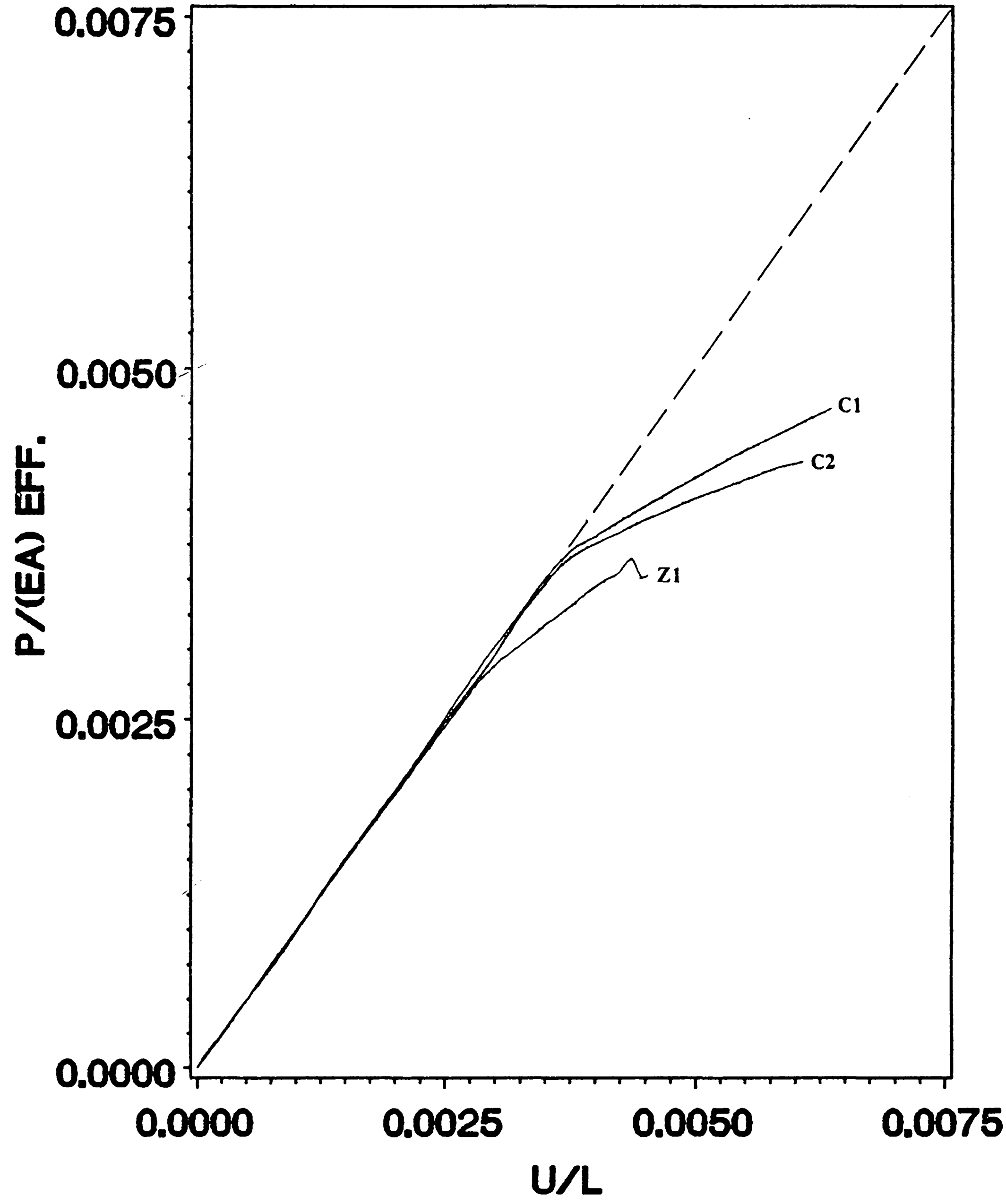

Figure 33. Dimensionless load-shortening plots, channel and zee specimens: from present study

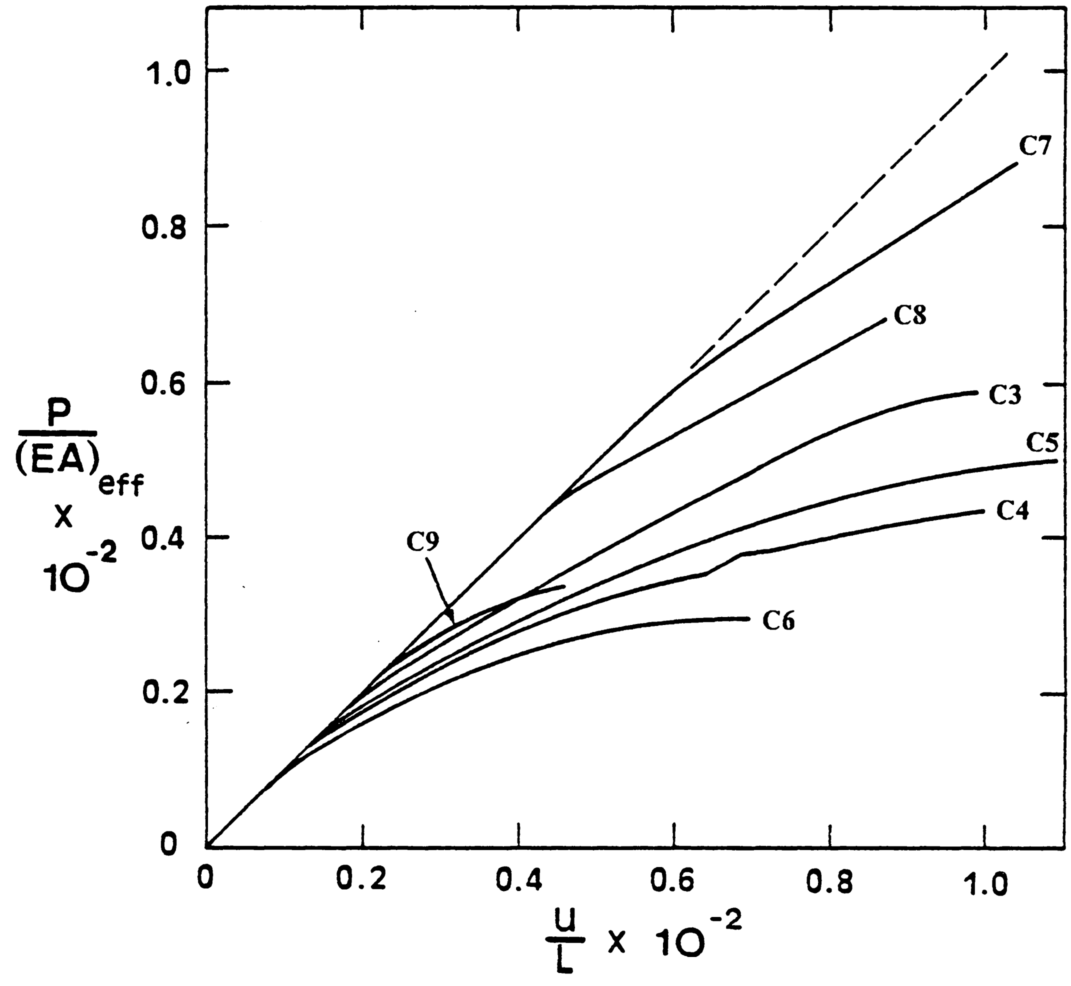

Figure 34. Dimensionless load-shortening plots, Ref. 8 channel specimens

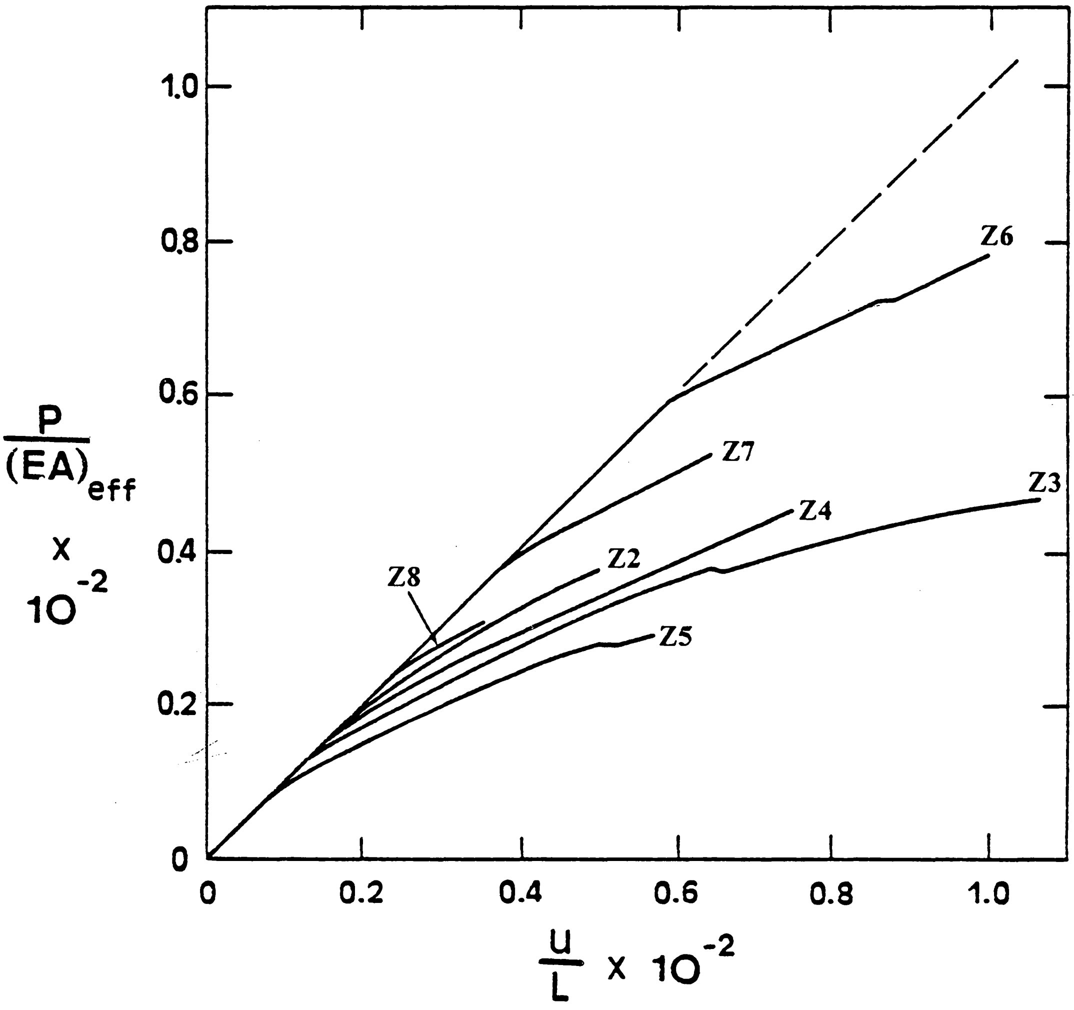

Figure 35. Dimensionless load-shortening plots, Ref. 8 zee specimens

Table 9. Channel and zee section experimental results

Specimen designation	$(b/t)_f$[a]	Prebuckling stiffness K, lb./in.	Buckling load P_{cr}, lb.	Buckling strain[b] $\varepsilon_{x_{cr}}$	Crippling load P_{cc}, lb.	Location of first damage[c]
C1[d]	8.8750	120540	2640	-.0042	3409	N
C2[d]	8.8750	69640	2500	-.0040	3022	N
C3 C1-3	27.625	228230	1120	--------	4239	--
C4 C1-4	27.625	223530	1180	--------	3947	--
C5 C1-5	24.500	209100	1250	--------	4247	--
C6 C1-6	27.625	54420	920	--------	2903	--
C7 C1-7A	13.563	351000	8300	--------	12426	--
C8 C1-8B	13.563	467000	8330	--------	13284	--
C9 C1-9	15.125	64430	1730	--------	2627	--
Z1[d]	13.563	129310	7080	-.0033	9207	COD
Z2 Z1-2	24.500	249730	1275	--------	3226	--
Z3 Z1-3	27.625	214130	1200	--------	3685	--
Z4 Z1-4	24.500	202930	1160	--------	4326	--
Z5 Z1-5	24.500	45740	975	--------	3076	--
Z6 Z1-6A	13.563	365250	8400	--------	12121	--
Z7 Z1-7B	13.563	507000	7900	--------	10675	--
Z8 Z1-8	12.000	51070	1925	--------	2367	--

[a] Flange width-to-thickness ratio.

[b] Average axial strain in the cross section at buckling. Data unavailable for Ref. 8 specimens.

[c] This column refers to the suspected nature and location of first damage within the specimen as inferred from experimental data:
COD -- corner opening delamination
N -- no damage observed prior to failure.
Data was unavailable for Ref. 8 specimens.

[d] Specimens tested as a part of the current study. All other specimens are from Ref. 8.

3.3.2 Description of Damage Events

Since specimens C1 and C2 exhibited no detectable damage events prior to failure, and no damage event information was available on the specimens from Ref. 8, only the damage initiation mode of specimen Z1 needs to be discussed. The initial damage appears to be a corner opening delamination in specimen Z1 at a load of approximately 8400 lbs. Figure 36 shows plots of data obtained from back-to-back axial and lateral strain gage pairs mounted in one of the corners of the zee section at an axial position of $l/2$, in which the discontinuities caused by this damage event are evident. Plots of data from strain gages and displacement transducers from all other elements of the cross section and all other axial positions show little or no evidence of damage at this load. The damage event, then, took place in this corner. The axial gage pair in Figure 36 indicates a slight decrease in the amount of axial membrane strain, and thus the amount of axial load, being supported by this corner, which would be consistent with damage in the corner. The laterally mounted gages show a sharp increase in lateral tensile strain in the corner. This tensile strain jump, combined with the relatively low axial membrane strain level in the corner at $P = 8400$ lbs ($\varepsilon_x = -.0040$ in/in), suggests that the damage was due to a corner opening delamination and not a local material ultimate strength failure.

3.3.3 Effects of Geometric Parameters

3.3.3.1 Flange Width-To-Thickness Ratio

Average buckling stresses and average crippling stresses for all zees and channels from both studies are presented in Table 10, along with $(b/t)_f$ and r_c for each specimen. The stresses were determined by dividing the buckling and crippling load for each specimen in Table 9 by the original specimen cross-sectional area. Figure 37 shows the average buckling stress plotted against the flange width-

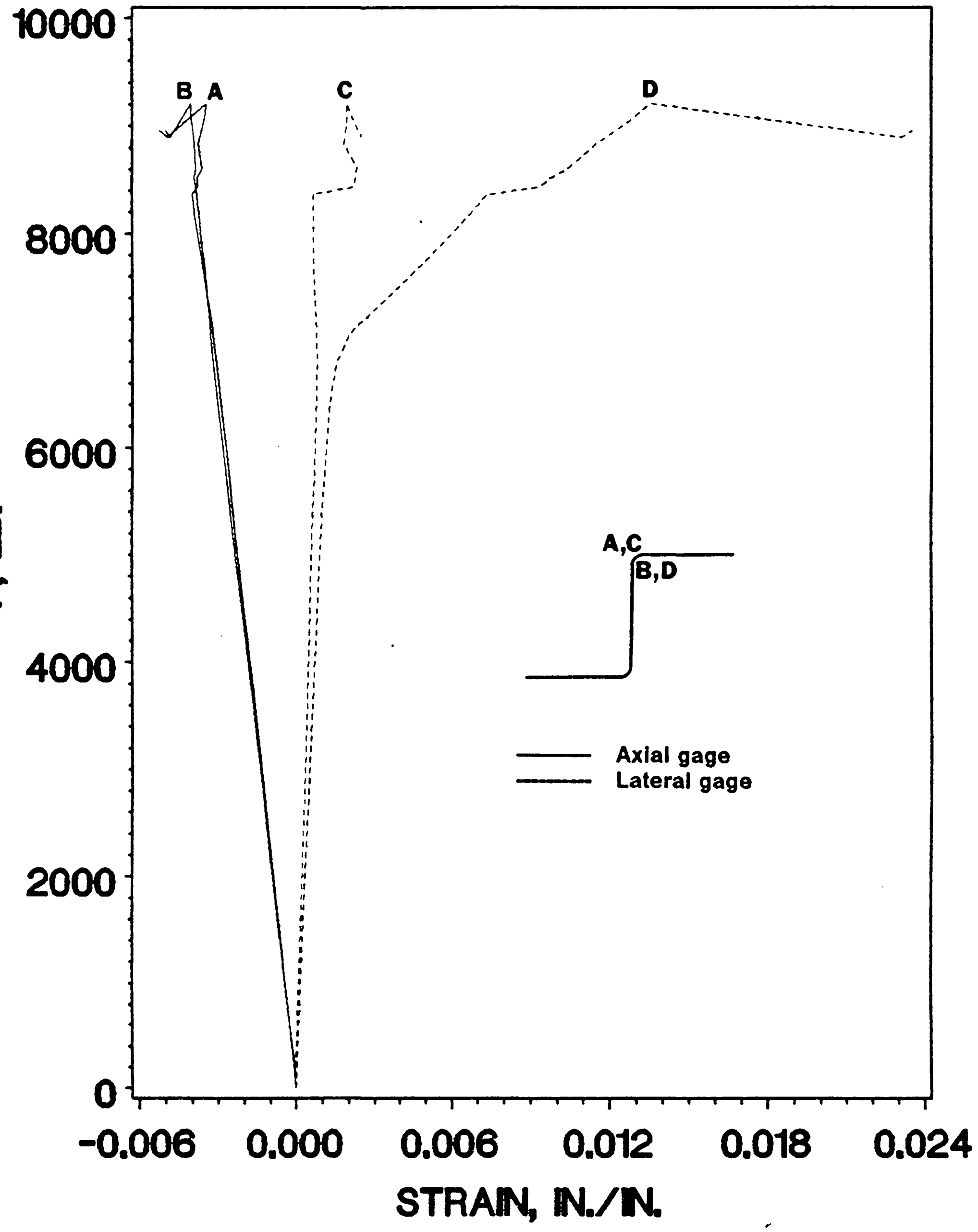

Figure 36. Corner axial and lateral strains, specimen Z1: strain gage data at an axial location of $l/2$

to-thickness ratio. The same sort of trend observed for the I- and J-section stiffeners in Figures 20 and 32 is visible in this figure: as the $(b/t)_f$ of a channel or zee stiffener is decreased, the average stress in the specimen at buckling tends to increase. Also similar to the results for I- and J-section columns is the lack of any consistent relationship between $(b/t)_f$ and σ_{cc} .

3.3.3.2 Inner Corner Radius

In assessing the effects of r_c on channel and zee specimen behavior, it is best to compare the response of specimens which have cross section geometries differing only in inner corner radius, as was done previously for the I- and J-sections. By referring to Tables 1 and 8, it may be seen that only two such comparisons can be made. Specimens C3, C4, and C6 from Ref. 8 are channels that have the same cross section (with an inner corner radius of 0.125 inches) and differ only in length; specimen C5 is identical in cross section to C3, C4, and C6 with the exception of an r_c of 0.250 inches. There are some length effects visible in the values of σ_{cr} and σ_{cc} in Table 10 for specimens C3, C4, and C6. Despite these effects, it is apparent in comparing these three specimens to specimen C5 that no significant results are produced in the average buckling or crippling stress by changing r_c . The second comparison contrasts the behavior of specimens Z2, Z4, and Z5, three zee section specimens which differ only in length and have inner corner radii of 0.250 inches, with the response of specimen Z3, a zee section identical to the other three except for an r_c equal to 0.125 inches. Although length effects are evident in Table 10 in the values of σ_{cr} and σ_{cc} for specimens Z2, Z4, and Z5, it once again seems that a change in inner corner radius produces no significant effects on the average buckling stress and average crippling stress in zee and channel section stiffeners. This conclusion is quite different from the result presented in Section 3.2.3.2, where it was found that an increase in the r_c of the corner between the web and cap flange in a J-section specimen (a corner which is identical to the corners in channel and zee sections) seemed to contribute to a consistent and large increase in the specimen average buckling stress.

Table 10. Channel and zee section average buckling and crippling stresses

Specimen designation	$(b/t)_f$[a]	Inner corner radius r_c, in.	Avg. buckling stress σ_{cr}, ksi[b]	Avg. crippling stress σ_{cc}, ksi[b]
C1[c]	8.8750	0.125	31.06	40.11
C2[c]	8.8750	0.125	29.41	35.55
C3	27.625	0.125	7.72	29.23
C4	27.625	0.125	8.14	27.22
C5	24.500	0.250	8.88	30.18
C6	27.625	0.125	6.34	20.02
C7	13.563	0.125	28.75	43.04
C8	13.563	0.125	28.85	46.01
C9	15.125	0.125	16.48	25.02
Z1[c]	13.563	0.125	24.52	31.89
Z2	24.500	0.250	9.06	22.93
Z3	27.625	0.125	8.28	25.41
Z4	24.500	0.250	8.24	30.75
Z5	24.500	0.250	6.93	21.86
Z6	13.563	0.125	29.10	41.98
Z7	13.563	0.125	27.36	36.98
Z8	12.000	0.250	19.12	23.51

[a] Flange width-to-thickness ratio.

[b] Average stress is defined as the compressive load divided by the original specimen cross-sectional area.

[c] Specimens tested as a part of the current study. All other specimens are from Ref. 8.

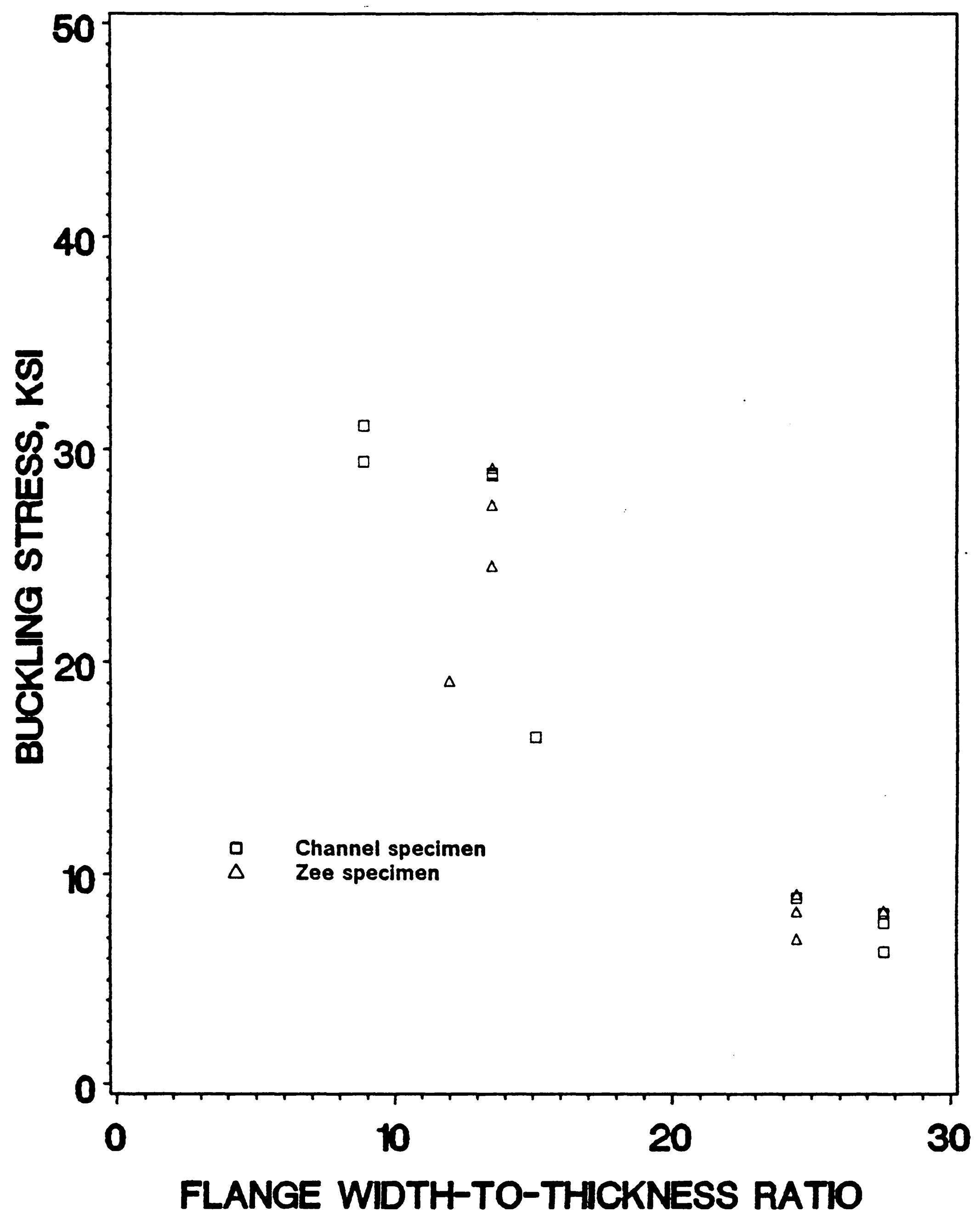

Figure 37. Buckling stress versus flange width-to-thickness ratio for channels and zees: specimens C1-C9, Z1-Z8

Chapter 4

Analysis and Correlation With Experiment

It was recognized in Ref. 8 that, due to the complexity and abruptness of the crippling process in graphite-epoxy thin-walled columns, any experimental study of such structures should be supplemented by an analytical program which examines the full range of stiffener response, including the postbuckled regime. A direct benefit of such a combined experimental and analytical approach is that the experiments provide examples against which to test the validity of the analytical technique or model. This verified analysis methodology may then be used to gain additional insight into the problem, by providing information which was not directly obtainable or observable during the experiments.

4.1 Analysis Methodology

Because of the relative complexity of the thin-walled shell structures under consideration in the current program, the only tractable technique which can be used to study analytically each structure as a whole (rather than as a collection of individually analyzed plate elements) is the finite element method. The two-dimensional finite element shell analysis code STAGS (STructural Analysis of General Shells)[13] was chosen for this purpose. This code has the capability to perform a variety of linear and nonlinear analyses on a wide selection of built-up shell structures, including the geometrically nonlinear static analysis required for the specimens in this study. It is, however, limited by its adherence to classical two-dimensional shell theory based on the Kirchhoff hypothesis, which assumes that every straight line originally normal to the middle surface remains straight and normal to the deflected middle surface and does not change in length. For such an assumption, the through-the-thickness shearing strains and normal strain vanish. In addition, the normal stress in the thickness direction is assumed to be negligibly small. Thus, the through-the-thickness stresses, which include interlaminar stresses, are assumed to be zero. It is possible, however, to estimate the interlaminar stresses from a STAGS solution; this procedure is discussed in Chapter 5.

4.2 *Bifurcation Buckling Analysis*

A complete nonlinear STAGS analysis of a structure like one of the stiffeners of the present study is expensive and requires a great deal of computer time. Thus, before each such analysis was performed, a series of simpler, cheaper bifurcation buckling analyses was executed using STAGS to develop a finite element model for the specimen of interest which was as accurate as possible. A bifurcation buckling analysis involves the solution of an eigenvalue problem which yields buckling loads (eigenvalues) and the corresponding mode shapes (eigenvectors). The performance of a potential model of a given specimen was judged by comparing the buckling load P_{cr}, the prebuckling stiffness K, and the buckling mode shape predicted by the bifurcation buckling analysis of that model to the experimental response of the specimen. In general, if the buckling load determined by bifurcation analysis was within ten percent of experiment, the prebuckling stiffness was within one percent, and the buckling mode obtained from STAGS had the same number of halfwaves as was observed during the experiment, the model was considered to be of adequate fidelity for use in the nonlinear analysis.

There were a number of features which could be altered in an attempt to improve the accuracy of a potential model. A STAGS model of a stiffener specimen was created by joining together several "shell units" of basic geometries, such as flat plates and portions of circular cylinders, until the overall shape of the structure was produced. For example, a zee section was created by properly joining three flat plate shell units (two flanges and a web) to two quarter circular cylinders (the corners of the section), as shown in Figure 38. Within each shell unit of a model, a finite element mesh or grid was defined. For every STAGS run performed throughout this study, the finite element used was the 411 element from the STAGS finite element library. The 411 element is a quadrilateral element, with a total of 32 degrees of freedom defined at four corner nodes and four midside nodes, as shown in Figure 39. The degrees of freedom defined in Figure 39 result in a cubic representation of the out-of-plane displacement, and in polynomials for the in-plane displacements which are cubic in one direction and quadratic in the other. One obvious way to improve the agreement between STAGS bifurcation model results and specimen experimental response was to increase the number of finite elements used, or refine the mesh defined in each shell unit. This approach to model improvement was expensive, however; and often, too coarse a grid was not the main reason for disparity between a STAGS model and experiment. Other factors responsible for such differences included the assumed model boundary conditions and the material properties used.

4.2.1 Boundary Conditions

Approximately one inch of each end of every specimen tested was supported by an aluminum-filled epoxy potting material and a steel or aluminum ring, as shown in Figure 2; the central, unsupported portion of each specimen is referred to as the gage length, *l*, of the specimen. The aluminum-filled epoxy compound produced uncertain, but nearly clamped, boundary conditions at the ends of the

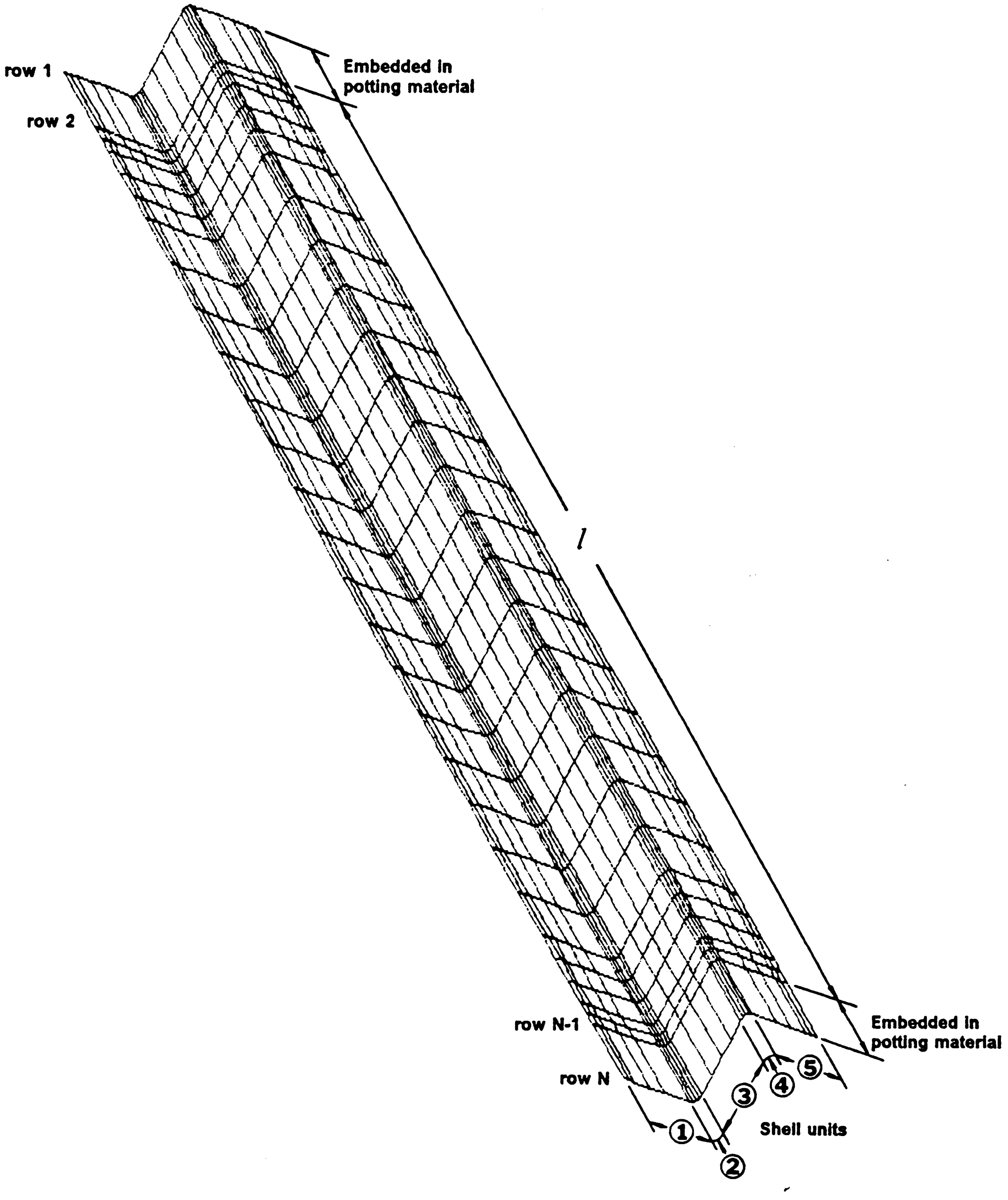

Figure 38. STAGS finite element model geometry for a zee section

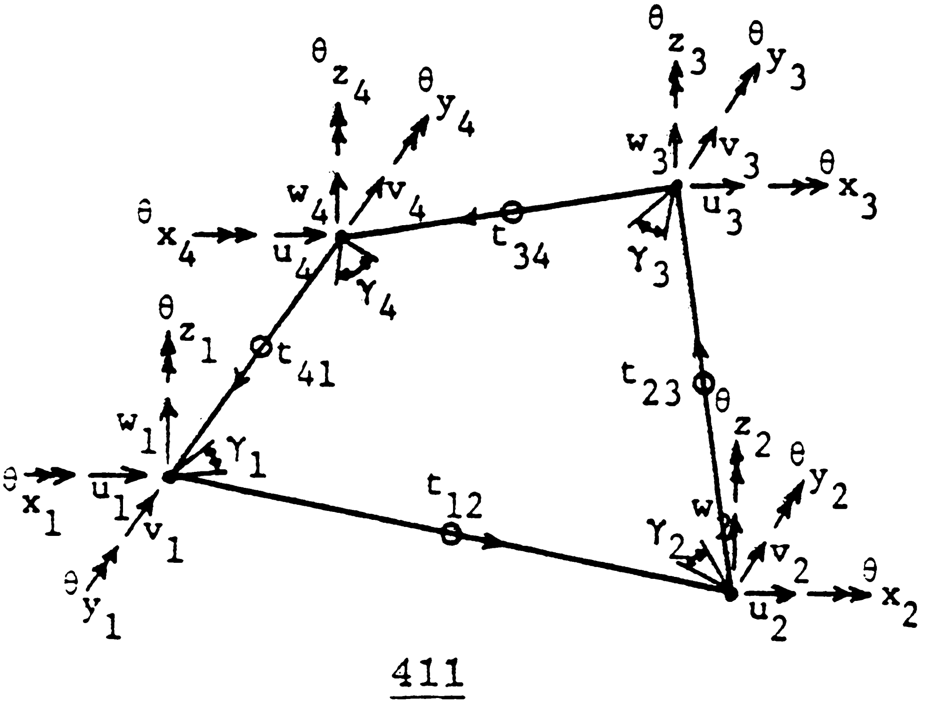

Figure 39. Degrees of freedom for the STAGS 411 finite element

specimen gage length; it was assumed that the specimen was subjected to completely clamped conditions at the ends where contact was made with the test machine platens. The total length of the specimen, including the portions embedded in the potting, was represented in each STAGS model, as shown in Figure 38. Clamped conditions were enforced at all finite element corner nodes at the ends of every model, while the restraints imposed on the corner nodes at the two interior potting surfaces were considered somewhat variable. It was possible with STAGS to constrain, individually or in any combination, the three displacements in, and the three rotations about, the nodal x, y, and z coordinate directions along any row or column of the corner nodes. This capability was used to enforce the boundary conditions along the rows of nodes corresponding to the ends of the gage length. The out-of-plane displacement at the gage length ends of each shell unit was always restrained to zero and the axial in-plane displacement (i.e., displacement in the direction of loading) at the ends of the gage length was always free for every STAGS model run. The freedom or restraint of the lateral in-plane displacement and all three rotations at these interior potting surfaces varied with the specimen analyzed.

4.2.2 Material Properties

Some limited variation of the nominal material properties was performed. Adjustment of material properties is justified by two observations. First, referring to Table 3, it is quite clear that sizable variations in total thickness from the nominal values ($t_{nom} = 0.04$ in. for eight ply specimens, $t_{nom} = 0.08$ in. for sixteen plies) occurred among the experimental specimens. These variations are most likely due to excesses or deficits of matrix material, and, if it is assumed that the volume of graphite fiber remained the same as in the nominal case, they imply changes in the fiber volume fraction, v_f, of the composite, where v_f is the ratio of the fiber volume V_f to the total volume of the composite material V. If a composite plate of in-plane dimensions a and b and thickness t_{nom} undergoes a change in volume V due only to a change in thickness from t_{nom} to t, while the volume of fibers V_f remains constant, then

$$V_f = v_{f_{nom}}(a \times b \times t_{nom}) = v_f(a \times b \times t) \tag{4.1}$$

and thus

$$v_f = \frac{v_{f_{nom}} t_{nom}}{t}, \tag{4.2}$$

which defines the new fiber volume fraction corresponding to the thickness change. For AS4/3502, with a fiber Young's modulus $E_f = 33.0$ msi, a matrix modulus $E_m = 1.33$ msi,[8] and a nominal value for E_1 of 18.5 msi, the nominal value of v_f may be obtained from the rule of mixtures

$$E_1 = E_f v_f + E_m v_m = E_f v_f + E_m(1 - v_f) \tag{4.3}$$

as $v_{f_{nom}} = 0.5422$. This is the fiber volume fraction corresponding to $t_{ply_{nom}} = 0.005$ in. For specimens with a thickness different from t_{nom}, the new fiber volume fraction v_f was found from equation (4.2) and then substituted into equation (4.3) to yield a new E_1 for use in STAGS analysis. It was assumed that a change in thickness and thus a change in v_f would produce negligible effects on E_2 and G_{12} ,[15] so these properties were not varied from their nominal values for any STAGS models. Since no data on individual fiber and matrix Poisson's ratios were available, the effect of fiber volume fraction on v_{12} was ignored.

4.2.3 Corner Details

The second justification for adjusting the material properties used in STAGS runs was the complete uncertainty of the value of fiber volume fraction in both corner regions of the I-section specimens and in the attachment corner of the J-section specimens caused by the lack of knowledge of the actual amount of unidirectional filler material inserted during fabrication. These corner regions were modeled in STAGS as three plates (the web and two flanges) meeting to form two right angles, with a beam (representing the 0° filler material) of the same cross section as the 0° filled area defined to exist at the same location. The material properties of this beam could be defined independently of the material properties of the rest of the elements of the STAGS model. The properties E_2, G_{12}, and ν_{12} for the beam were held constant at nominal values for all STAGS runs but, since v_f in the 0° filled corners of each specimen could assume virtually any value from zero to one, E_1 was allowed to vary in the beam elements from E_m to E_f, and the value producing the best bifurcation buckling results in comparison to experiment was chosen for use in the nonlinear model of the specimen under consideration.

Nominal values of b_w, b_f, r_c, and l, as given in Tables 1 and 8, were used in all STAGS models, both during development and during the actual nonlinear runs. Measured specimen average thicknesses, as listed in Table 3, were used in most cases when known.

4.3 Nonlinear Analysis

Once a STAGS model which exhibited adequate correlation with experiment in K, P_{cr}, and buckling mode shape was assembled based on the results of bifurcation buckling analyses, a nonlinear analysis of the specimen was performed. The only change made to the accepted model was to add very small initial geometric imperfections, to ensure that bending would be triggered for axial compressive loading. If the actual initial imperfections of the experimental specimen were known, they were added to the model. If the initial geometric imperfections of the physical specimen were not known, then an approximation of the experimentally observed buckling mode, in the form of a two-dimensional trigonometric function with an amplitude of one ply thickness or less, was incorporated into at least one of the flat plate elements of the cross section.

Because a nonlinear analysis of a structure as complex as one of the stiffeners in this study takes a considerable amount of computer time (a typical analysis performed for the current work had approximately 5000 degrees of freedom and required about 20000 CPU seconds to complete on a CDC CY-860 machine), it is usually accomplished in several stages, or "runs," of user-determined time duration. At the end of each analysis stage, solution data are automatically stored to provide the basis for a "restart" of the analysis in the next run. This procedure facilitates the detection and correction of possible computational difficulties which would otherwise waste valuable computer time. The solution method chosen for the current work is an adaptation of the commonly used modified Newton-Raphson technique, in which the analysis is carried out as a series of linearized incremental steps, with iterations performed during each step to correct the linearization error. The stiffness matrix is not necessarily updated with every incremented step, but it is updated when the convergence of the iterations becomes difficult or impossible. Typically, the modified Newton-Raphson technique employs the load as the incremented parameter; the adapted version used in the present study increments an "arc-length" or path length parameter, as proposed by Riks[16]. This path length parameter is actually a vector with load and displacement components, and thus the so-called Riks method bears similarities to both load and displacement controlled analyses. The main advantages of the Riks method are its increased efficiency and its ability to track nonlinear response through limit points.

Since STAGS has no programmed capability to predict failure of a structure, each nonlinear analysis performed for the current study was deemed complete when it had progressed far enough to include the entire range of load-shortening response observed during the corresponding experiment. Once the analysis was terminated, the stored restart data from the various "runs" involved in the total nonlinear analysis were used to generate analytical surface strain and displacement distributions for a number of loads at which strain gage and DCDT information had been sampled during the test, as a means for later comparison of experiment and analysis. Several examples of such comparisons are discussed in the next section. In addition, in-plane stress data were obtained from STAGS for each analytical model either at the load corresponding to the first damage event observed during the testing of the physical specimen, or at the crippling load if no evidence of damage had been found. These stress data were then used to evaluate a number of plane stress failure criteria. The results of this failure analysis are presented in Section 4.5.

4.4 *Results of Analysis and Correlation With Experiment*

Nonlinear analyses were attempted for six specimens (I2, I10, I16, J5, and Z1 from the present study, and Z6 from Ref. 8). The analysis of specimen J5 was not completed due to numerical difficulties caused by the presence of at least one bifurcation point in the postbuckled region of the primary equilibrium path. The other five analyses were completed; the results of three of these analyses are discussed here. For each example, relevant details of the model are presented, followed by examination of the correlation between analysis and experiment. This correlation is evaluated both on a global scale, in terms of load-shortening behavior, and on a local basis, by comparing cross-sectional axial surface strain distributions.

4.4.1 Specimen Z6

Specimen Z6 from the experimental program detailed in Ref. 8 was the first specimen subjected to a complete nonlinear STAGS analysis as a part of the current study. For this reason, extra care was taken to verify both the experimental and analytical results for this specimen. To confirm the original experimental response, a second stiffener of identical geometry and layup was tested. In addition, nonlinear analyses were performed on two nearly identical models of specimen Z6. The models differed only in their initial geometric imperfections. The analysis identified as Run 1 had an initial imperfection applied to both flanges and the web with the same shape as the expected buckling mode and an amplitude of one ply thickness (0.005 inch). The second analysis, referred to as Run 2, incorporated this same imperfection shape and amplitude in one flange only. Comparison of the results from these two nonlinear analyses yielded some valuable information on the general imperfection sensitivity of the specimens in this study, which was helpful in assigning initial geometric imperfections to later analytical models.

The undeformed geometry of the model used for both analyses of specimen Z6 is presented in Figure 40, and shows the finite element discretization used. Nominal material properties and ply thickness were used in both analyses, and at the ends of the gage length of each shell unit, the out-of-plane displacement and in-plane lateral displacement were defined to be zero. Axial in-plane (i.e., load direction) displacement and all three rotations remained free along the specimen gage length ends. Specimen Z6 exhibited a one-halfwave buckling mode, shown in Figure 41, during both experiments and both analyses. Experimental and analytical load-shortening responses are presented in Figure 42. The results of both of the experiments and both nonlinear analyses are given. The filled symbols represent specimen failure. Although the replicate specimen failed at a slightly lower load than specimen Z6, the overall agreement between the experimental behavior of the two specimens is excellent, and thus only the response of the original specimen will be discussed. Analytical Runs 1 and 2 agree with each other in prebuckling, but differ in the postbuckled portion of the load-shortening curve. Since the two models differ only in the initial imperfection defined, the lack of correlation between STAGS Run 1 and Run 2 must be due solely to this imperfection change. As is evident from Figure 42, removing the initial imperfection from one of the flanges raised the buckling load obtained from the load-shortening curve of the nonlinear analysis. The load-shortening plots from both nonlinear analyses exhibit similar slopes or "stiffnesses" after buckling, and so it seems that the effect of a variation in initial imperfection is chiefly on the buckling load only, and diminishes in the postbuckled region. Experiment and analysis show excellent correlation in Figure 42 through the entire range of load up to and including buckling. The buckling load of 8300 lbs. from STAGS Run 1 compares very favorably with the experimental value of 8400 lbs. from Table 9. The buckling load of 9000 lbs. obtained from the second nonlinear analysis does not correlate as well. In postbuckling, there is less agreement between analysis and experiment, some of which may be due to initial imperfection differences between analysis and experiment. The experimental specimens are more compliant in postbuckling than are the analytical models, though, and this difference suggests that there are other reasons for the lack of correlation in postbuckling. Specimen Z6 has a flange width-to-thickness ratio $(b/t)_f$ of 13.563; and, as was observed in Chapter 3, for such a low value of $(b/t)_f$ the effects of through-the-thickness shear may not be negligible. STAGS, however, because it is based on the Kirchhoff hypothesis, neglects transverse shearing deformations. This neglecting of transverse shearing deformations apparently causes both STAGS models to be stiffer than the physical specimen in postbuckling, and leads at least in part to the lack of correlation between experiment and analysis visible in Figure 42. In addition, the restraint exerted upon the physical specimen by the potting material at the ends of the gage length could not be quantitatively determined, and thus the boundary conditions enforced in the STAGS models at the rows of nodes corresponding to the gage length ends might be incorrect. It is known that for plate problems, variations of the in-plane boundary conditions can have significant effects on the postbuckling response,[17] and thus inaccurate modeling of these end conditions in the STAGS models could also contribute to the observed lack of postbuckling correlation for specimen Z6.

Plots of axial surface strains versus contour coordinate, s, at an axial location of $l/2$ are shown in Figures 43-45 for increasing load. The distributions from both analyses are presented; only the strain gage data from the original specimen Z6 are given, since the data from both experiments are similar. The vertical dashed lines in these three figures indicate the boundaries between the shell units of the STAGS models. For example, the leftmost dashed line is the junction between the first flange and the first circular cylindrical corner; the next dotted line marks the end of the curved corner and the beginning of the web. Figure 43 shows the surface strain distributions at $P = 3563.64$ lbs. At this prebuckled load $(P/P_{cr} = 0.424)$, a nearly uniform state of membrane strain exists, and correlation among the two analyses and the experiment is excellent. The surface strain distributions for a load very near the experimental buckling load, $P = 8365.96$ lbs. $(P/P_{cr} = 0.996)$, are presented in Figure 44. Correlation between experimental and analytical results in the web and corners remains good at this load, but is somewhat degraded at the flange free edges. At this load

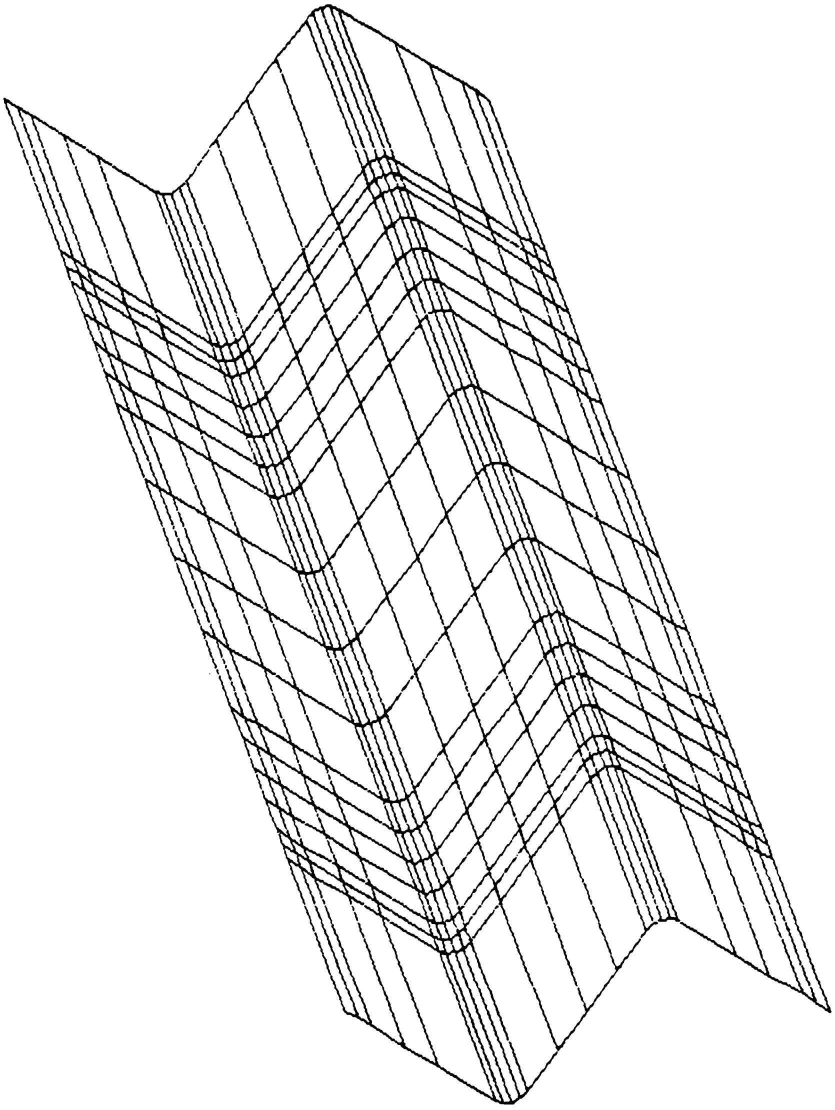

Figure 40. STAGS model geometry and finite element mesh for specimen Z6

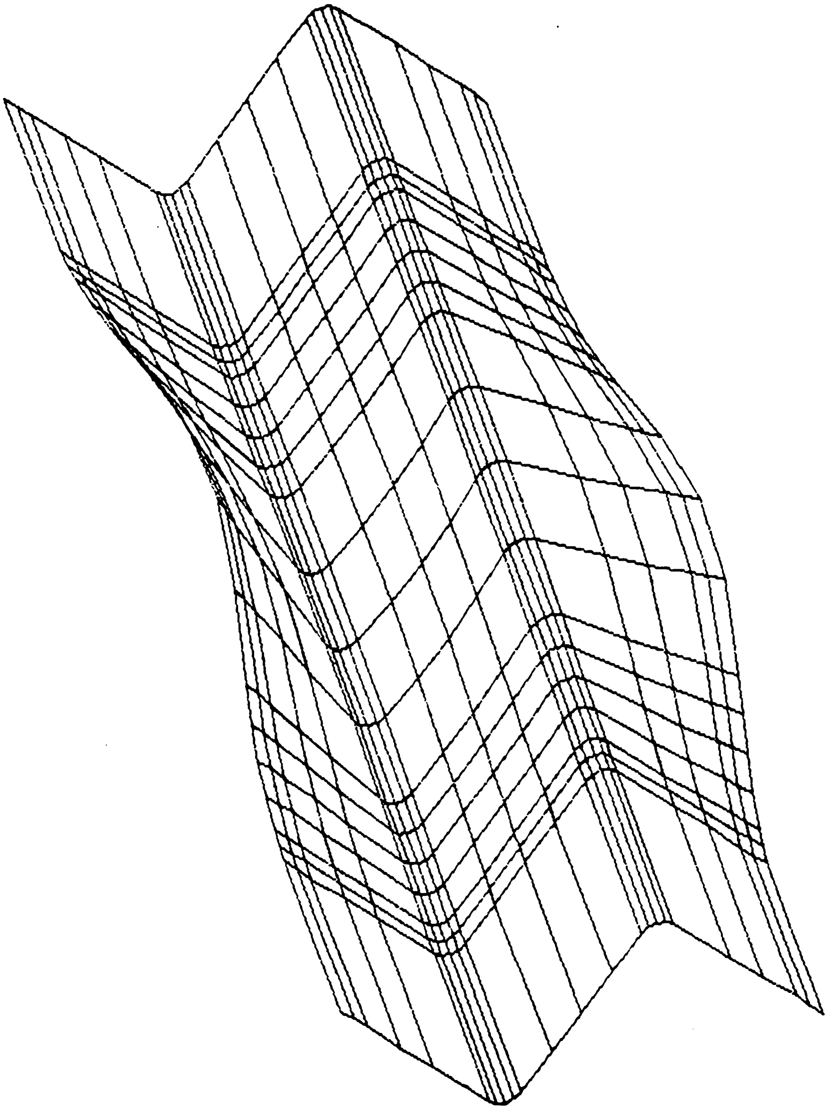

Figure 41. Buckling mode of specimen Z6

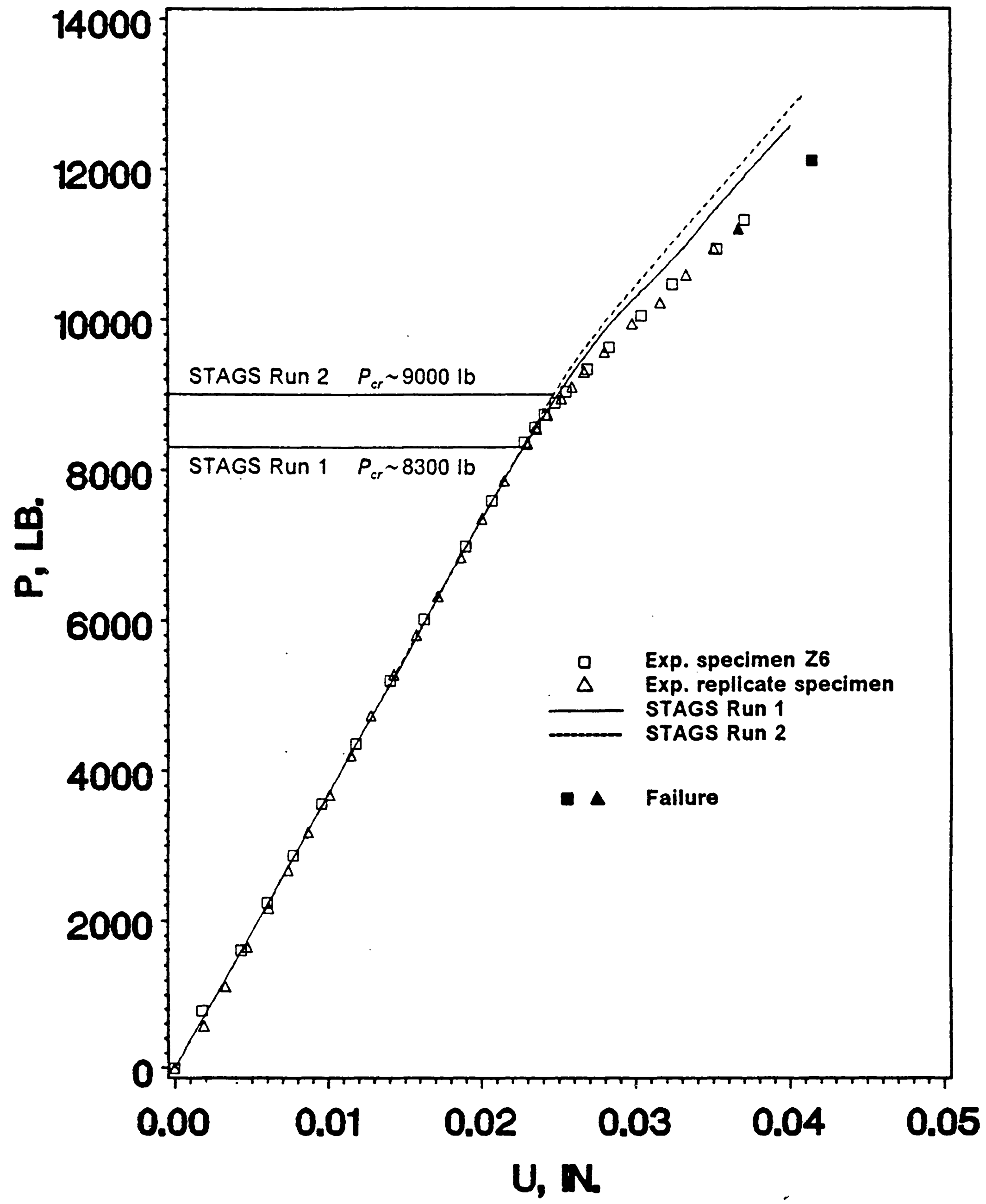

Figure 42. Load-shortening curves for specimen Z6 of Ref. 8 and replicate: both experiments and STAGS nonlinear Runs 1 and 2

(i.e., near buckling), some of this lack of correlation is probably due to differences in initial geometric imperfections. It is quite obvious in this figure that the leftmost flange of the model for STAGS Run 2 was the flange from which the initial imperfection of STAGS Run 1 was removed. The removal of this imperfection causes a decrease in bending in all cross-sectional elements of the second model compared to the first model at the same load, as would be suggested by the higher buckling load for Run 2 shown in Figure 42. Surface strain distributions corresponding to the experimental crippling load ($P_{cc}/P_{cr} = 1.443$) are shown in Figure 45. Correlation between analysis and experiment is still fair in the corners and the web of specimen Z6; but at the free edges of the flanges, the physical specimen exhibits considerably more bending than do the STAGS analyses. As was observed in relation to the load-shortening curve for this specimen in Figure 42, this lack of correlation is at least partly due to neglecting of transverse shearing deformations by STAGS, which causes the nonlinear analytical models to be stiffer in postbuckling, and therefore to show less bending than was seen in the flanges and web of the corresponding experiment. The lack of agreement may also be due to inaccuracies in the boundary conditions enforced at the ends of the gage length in the STAGS models. An additional conclusion which was drawn from Figure 42 and is borne out in Figure 45 is that the effects of the differences in the initial geometric imperfections defined in the two STAGS models seem to decay with increasing load after the specimen has buckled.

4.4.2 Specimen I2

The finite element discretization scheme used to model specimen I2 is shown in the undeformed geometry plot from STAGS in Figure 46. As was discussed in Section 4.2.3, each corner of this I-section column is modeled as three flat plates (the web and two flanges) meeting at initially right angles combined with a beam having the cross-sectional properties (area, moments of inertia, and location of centroid) of the 0° filled region of the physical specimen. The beams do not appear in Figure 46. Figure 47 shows the idealized corner region that was used to generate the beam cross-

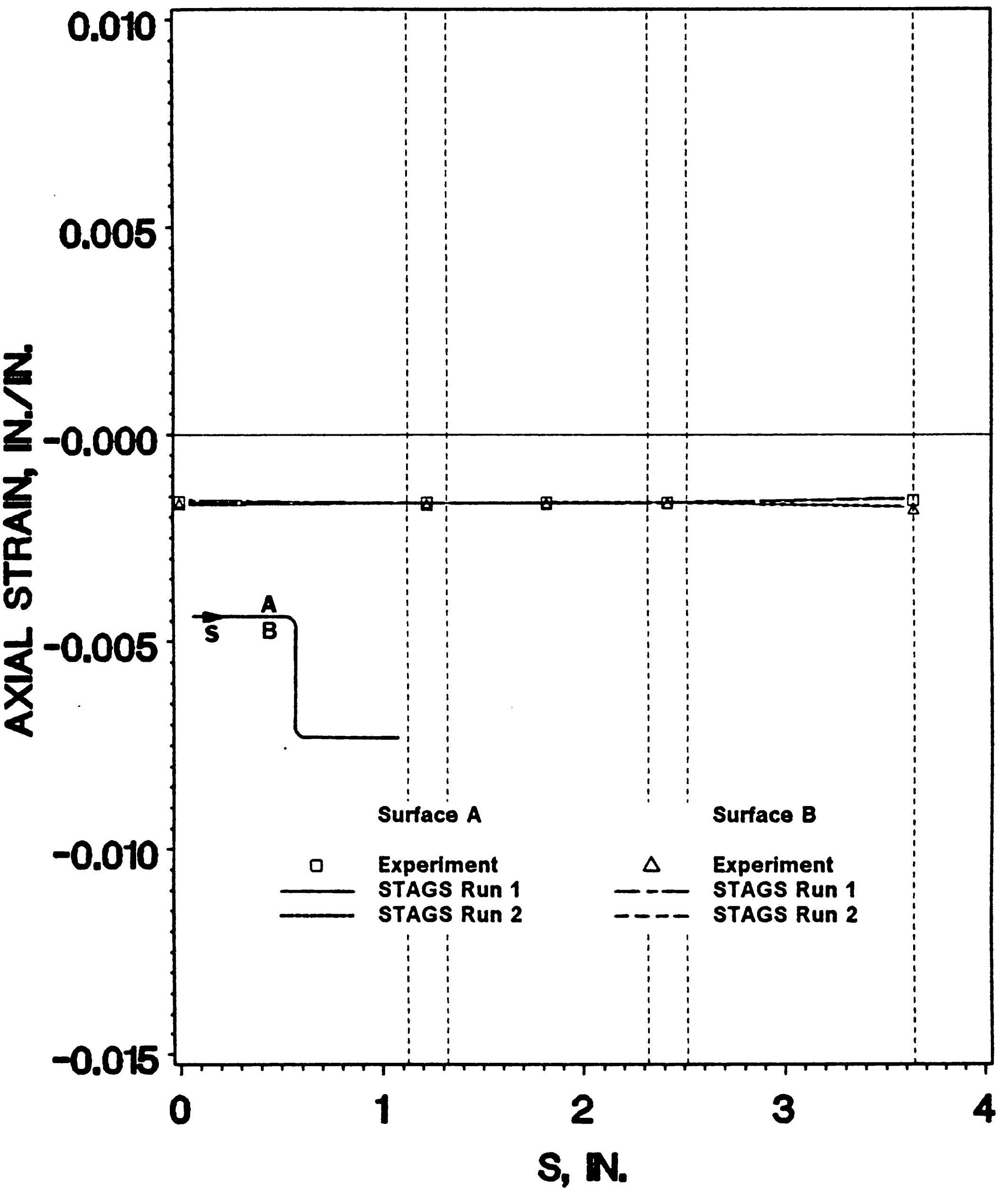

Figure 43. Axial surface strains for specimen Z6 at P = 3563.64 lb: experiment and STAGS nonlinear Runs 1 and 2 at $l/2$, prior to buckling ($P/P_{cr} = 0.424$)

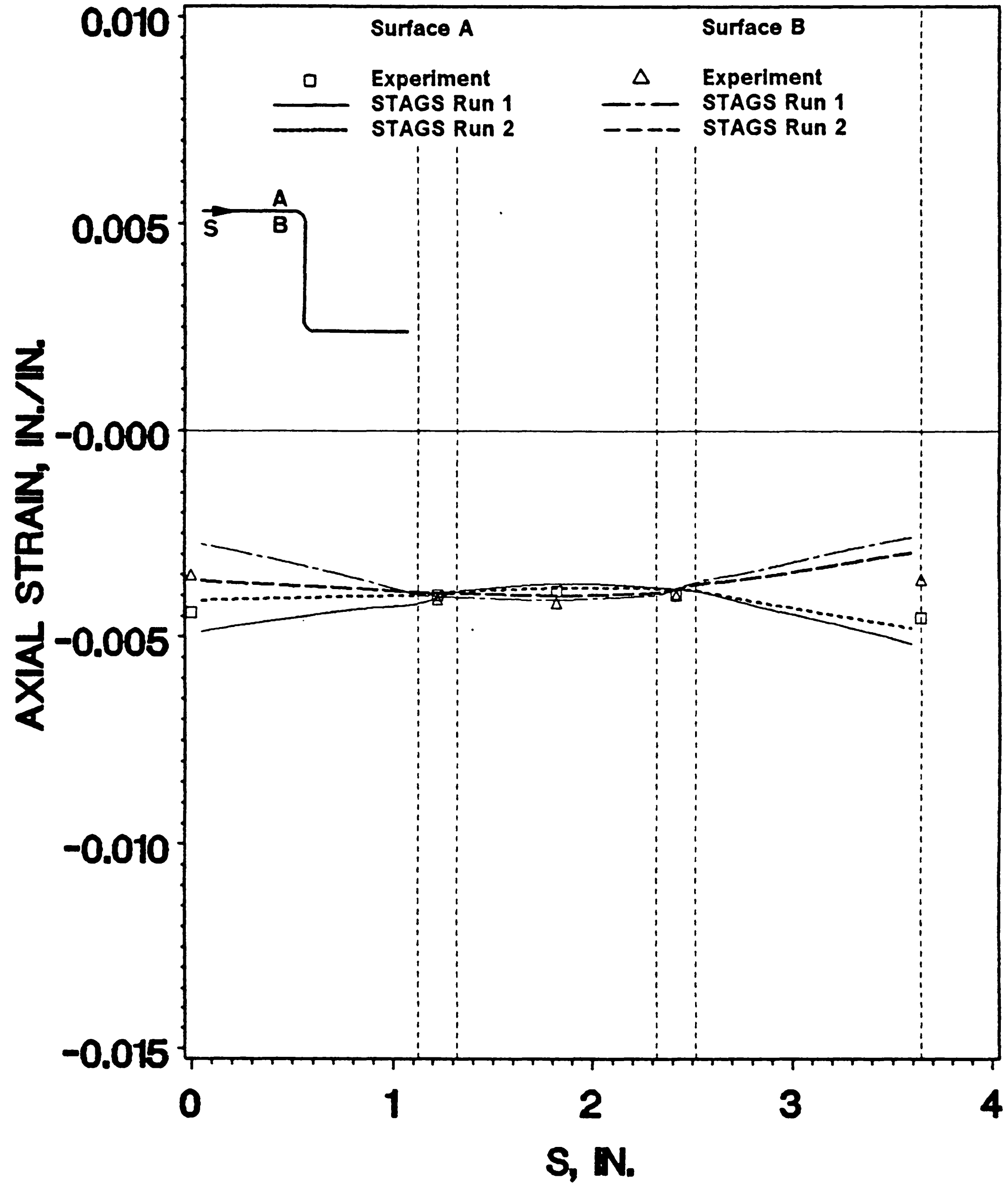

Figure 44. Axial surface strains for specimen Z6 at P = 8365.96 lb: experiment and STAGS nonlinear Runs 1 and 2 at $l/2$, near buckling load ($P/P_{cr} = 0.996$)

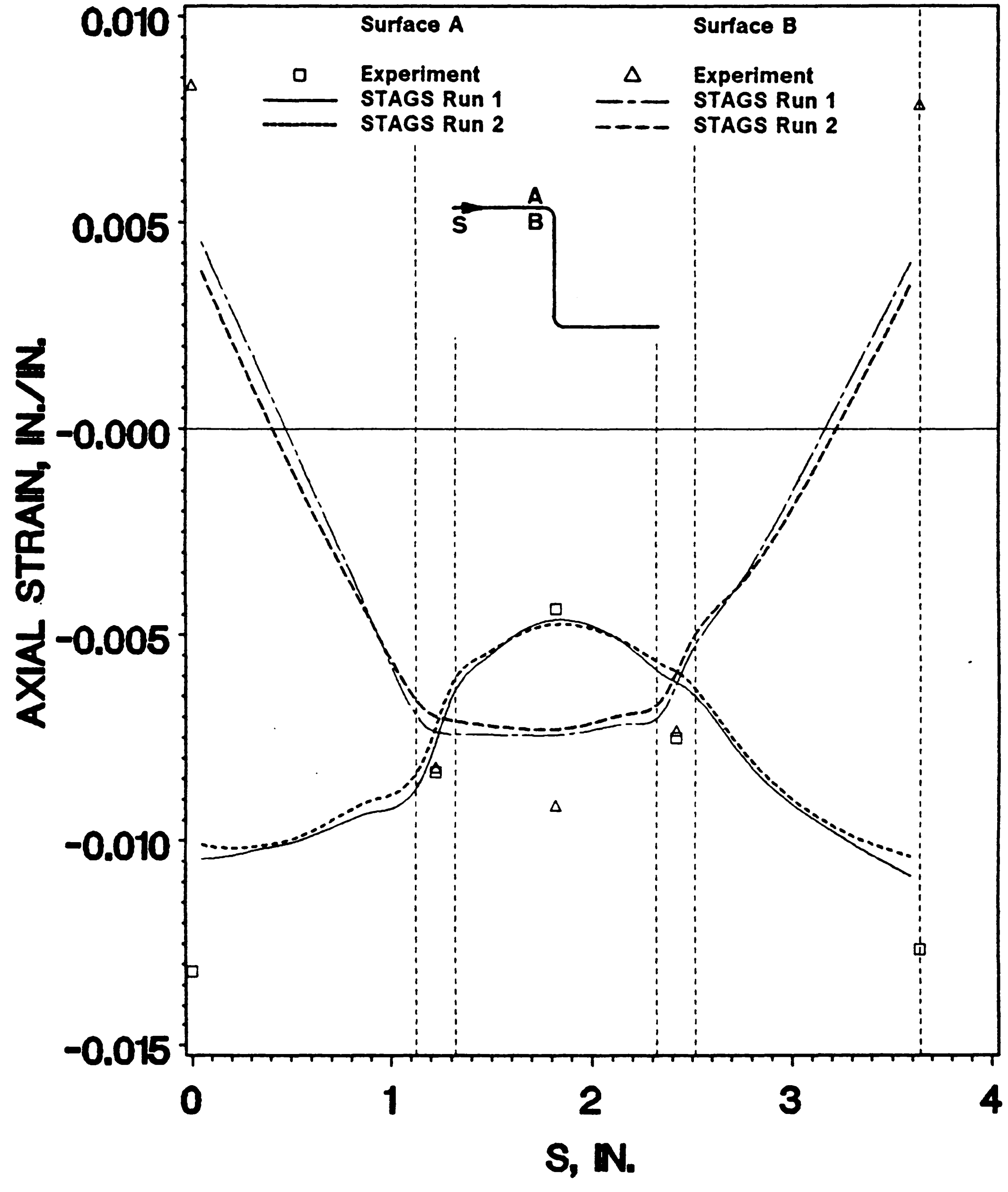

Figure 45. Axial surface strains for specimen Z6 at P = 12121.1 lb: experiment and STAGS nonlinear Runs 1 and 2 at $l/2$, at crippling load (P_{cc}/P_{cr} = 1.443)

sectional properties. The "X" represents the point at which the midplanes of the web and the two flanges, in both the physical specimen and the STAGS model, intersect. The beam in the STAGS model is defined to have displacement compatibility with this point; the eccentricity between the beam centroid and this junction point is taken into account in the analysis. This approximation of the corner region by a discrete beam would not be expected to significantly degrade the correlation between experiment and analysis for global response measures such as the buckling load and the load-shortening curve, but it would be expected to have a greater influence on the accuracy of analytical surface strains near the corners.

The measured average specimen thickness as given in Table 3 was used for the nonlinear analysis of specimen I2. Bifurcation buckling model development runs suggested that values of $E_1 = 18.7$ msi for the filled corner regions and 17.0 msi elsewhere would provide the best correlation with experiment. At the ends of the specimen gage length, the out-of-plane displacement, the in-plane lateral displacement, and the out-of-plane rotation about the line defined by the intersection of the potting material with the specimen were constrained to zero; axial (i.e., load direction) displacement and the two remaining rotations were left free.

The buckling mode obtained from the finite element model of specimen I2 is presented in Figure 48, and the two-halfwave mode shape shown is the same as that observed during testing of the physical specimen. The load-shortening curve from the nonlinear STAGS analysis, represented by a solid line, is compared to experiment, represented by open squares, in Figure 49. The filled symbol represents specimen failure. As with specimen Z6, correlation is excellent through the entire prebuckling range up to buckling; but unlike specimen Z6, in which a significant loss of agreement between experiment and analysis occurred almost immediately after buckling (see Figure 42), correlation remains quite good for specimen I2 through initial postbuckling. This difference seems to be due to the decreased influence of transverse shear deformations on the response of specimen I2. Since the flange width-to-thickness ratio of specimen I2 is 27.625, compared to 13.563 for specimen Z6, specimen I2 exhibits less transverse shearing effects than specimen Z6. Thus, the STAGS postbuckling analysis, which ignores transverse shear effects, is more applicable to specimen I2 than

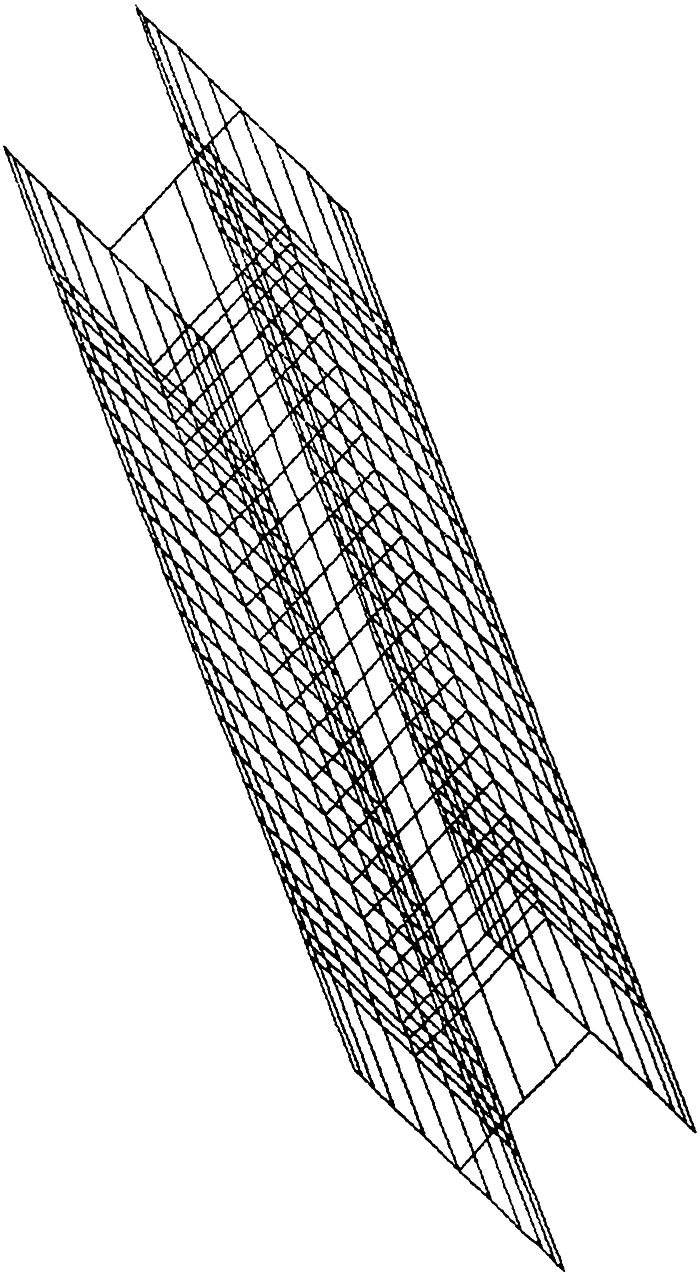

Figure 46. STAGS model geometry and finite element mesh for specimen I2

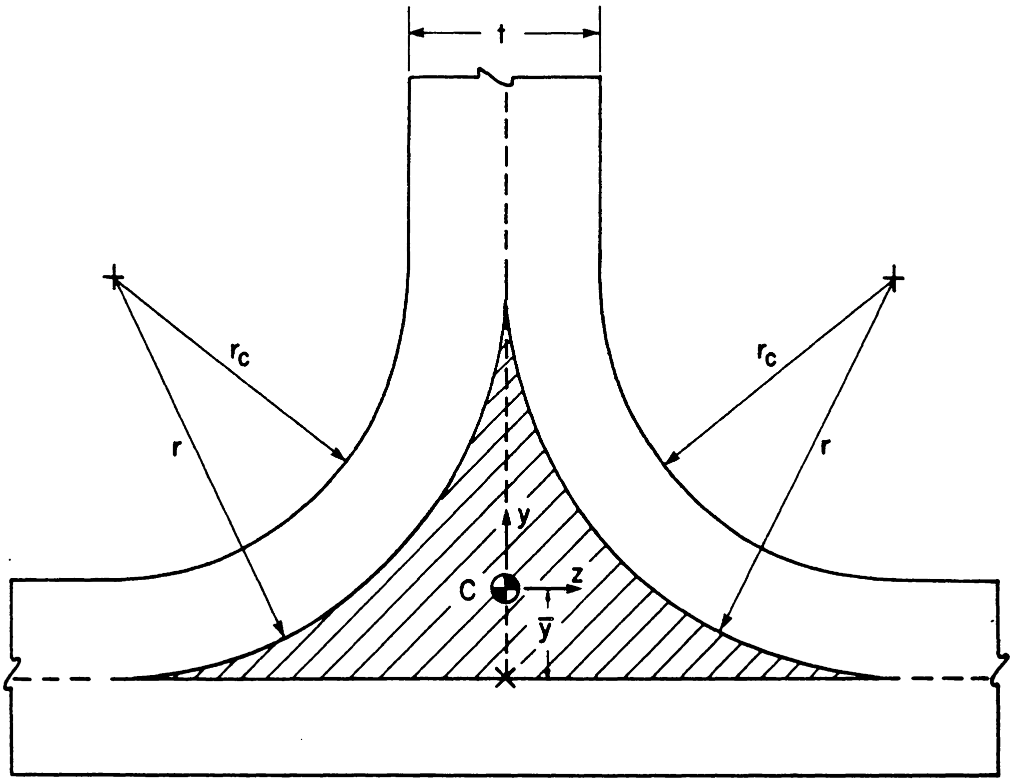

FOR THE SHADED REGION:

$$r = r_c + \frac{t}{2}$$

$$\bar{y} = 0.22\,r \qquad A = 2r^2\left(1 - \frac{\pi}{4}\right)$$

$$I_{yy} = 0.0350\,r^4 \qquad I_{zz} = 0.0142\,r^4$$

$$J \sim I_{yy} + I_{zz} = 0.0492\,r^4$$

Figure 47. Detail of filled corner region of I- and J-section specimens

to Z6. The buckling load of approximately 2900 lbs. predicted by STAGS for specimen I2 is in excellent agreement with the experimental value of $P_{cr} = 2786$ lbs.

A series of plots of axial surface strain distributions versus the contour coordinate, s, for specimen I2 at an axial location of $l/3$ is shown in Figures 50-52 for increasing values of compressive load. As in Figures 43-45 for specimen Z6, the vertical dashed lines in these plots mark the boundaries between the shell units of the STAGS model. Figure 50 shows the analytical and experimental strain distributions at a load of 994.87 lbs., which is in the early prebuckling load range ($P/P_{cr} = 0.357$); the nearly uniform membrane strain level is expected at this low load, and excellent correlation between analysis and experiment is seen. The experimentally and analytically determined axial surface strains near the experimental buckling load ($P/P_{cr} = 0.995$) are presented in Figure 51. Correlation remains quite good, although the excess stiffness inherent in the STAGS model due to neglecting the transverse shearing deformations is apparently beginning to manifest itself as a noticeable discrepancy in the amount of bending observed at the flange free edges. This discrepancy could also be due, however, to a difference between the initial geometric imperfections incorporated in the STAGS model and the initial imperfections of the physical specimen, or to the possibility that the buckling mode wave peaks seen in experiment occurred in slightly different axial locations than those observed in the analysis, although the physical specimen and analytical model were observed to have had the same number of halfwaves. Such minor shape differences would result in the STAGS nonlinear model and the experimental specimen having different distributions of membrane and bending strains at the same axial location. Whatever the cause, the discrepancy in strain values continues to grow with increasing load, as is evident in Figure 52. The strain distributions shown in this figure correspond to $P_{cc} = 10289.02$ lbs., which is the crippling load for specimen I2 ($P_{cc}/P_{cr} = 3.693$). Although the general shape of the analytical and experimental strain distributions correlate, substantial differences exist at the flange free edges between the actual values of strain observed experimentally and those predicted by STAGS, due in part to either one or a combination of the reasons discussed above in reference to Figure 51. In addition, inaccurate modeling of the in-plane boundary conditions at the ends of the gage length of specimen I2 in the

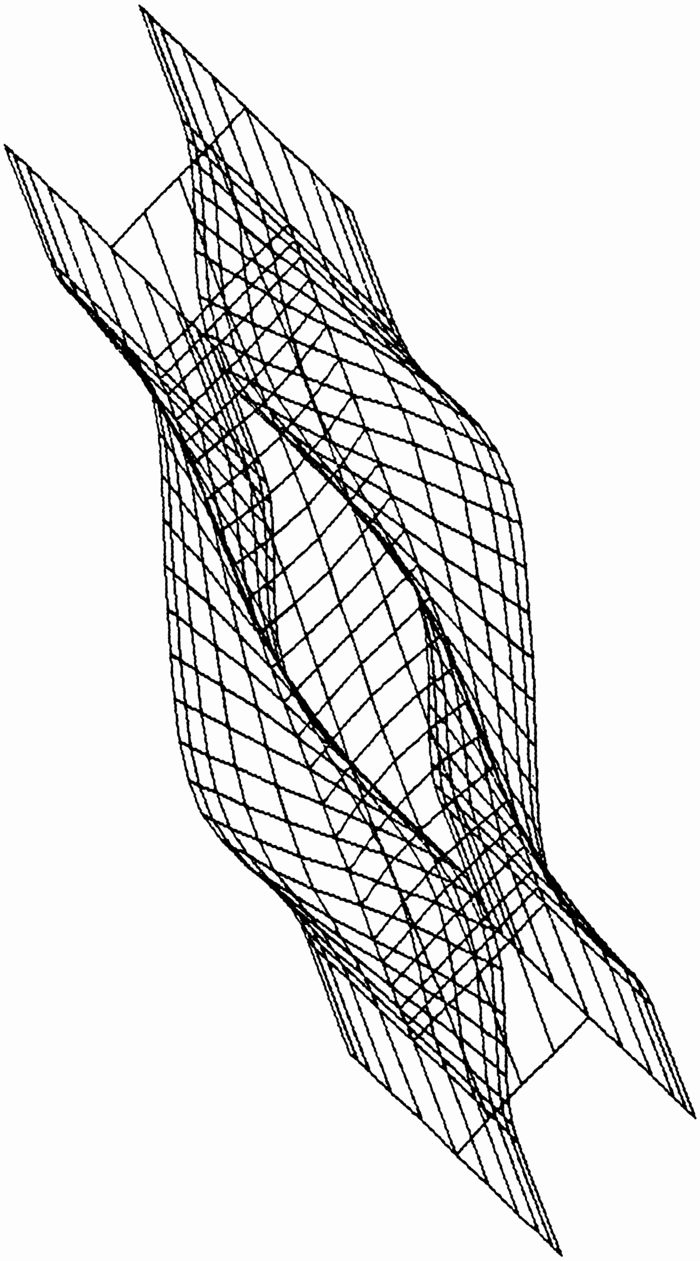

Figure 48. Buckling mode of specimen I2

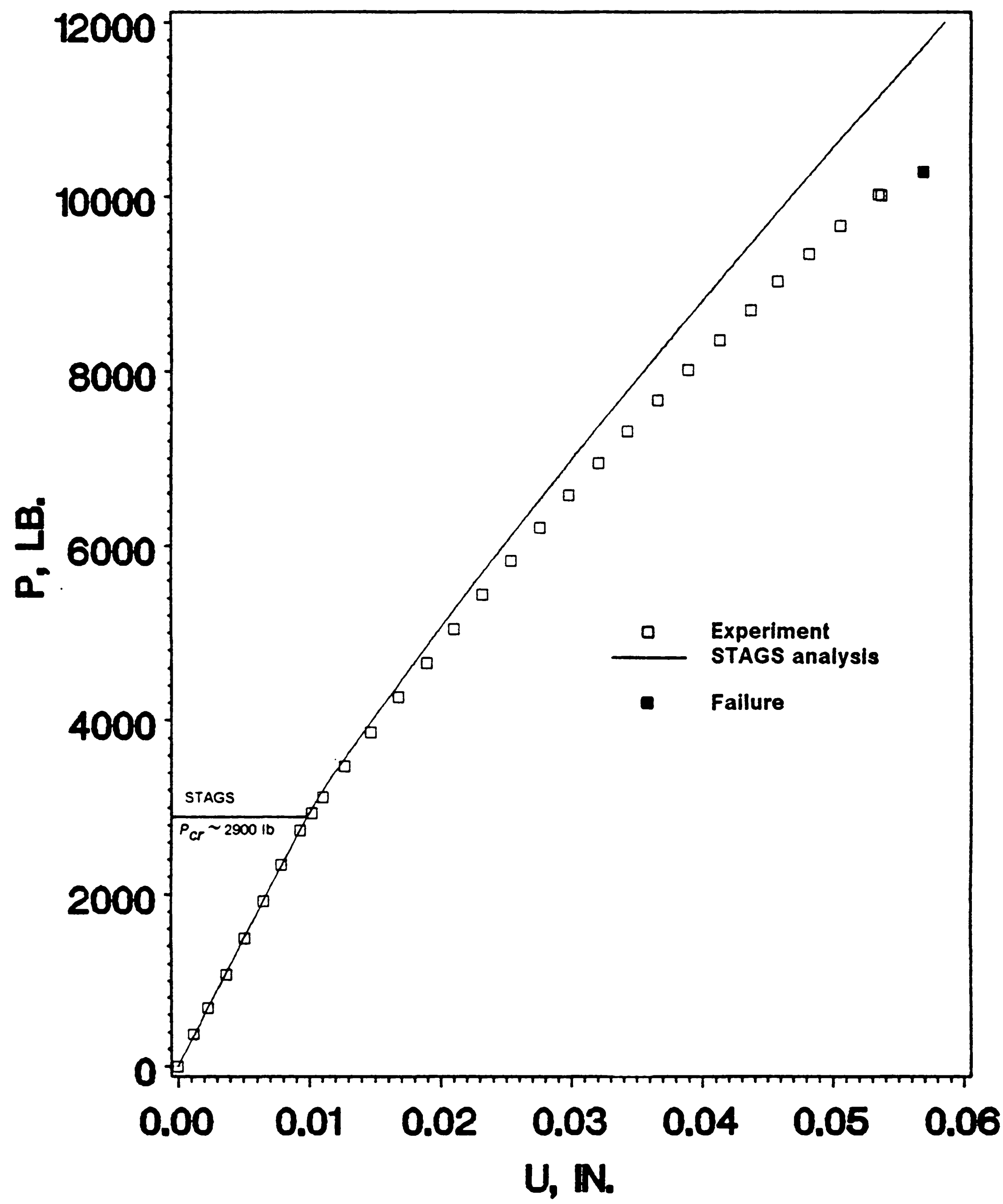

Figure 49. Load-shortening curves for specimen I2: experiment and STAGS nonlinear analysis

STAGS analysis could cause a loss of agreement in postbuckling. Also contributing to the overall lack of correlation at this load, especially in the corners, are the modeling deficiencies in the corner regions and the damage which occurred in the corners of experimental specimen I2 as noted in Table 4 and discussed in Chapter 3.

4.4.3 Specimen I16

The finite element discretization chosen for the STAGS model of specimen I16 is shown in Figure 53. The corners were modeled in the same fashion as the corners of specimen I2. The actual average measured thickness as given in Table 3 was used; substitution of this thickness into equation (4.2) gives a $v_f = 0.4929$, which through equation (4.3) provides an $E_1 = 16.94$ msi, which was used in all five of the plate element shell units in the STAGS model. Bifurcation buckling model development runs implied that the best agreement with experiment would be obtained if in the 0° fiber-filled corner regions, $E_1 = 7$ msi. This low figure seems to suggest that a large surplus of matrix material existed in the corners of the specimen. The only constraint enforced upon the nodes at the ends of the specimen gage length was on the out-of-plane displacement; all other degrees of freedom at these ends were left free.

The buckling mode which developed during the nonlinear analysis of specimen I16 is shown in Figure 54; the two-halfwave mode shape shown correlates with the mode observed during testing of the physical specimen. The load versus end shortening curves from experiment and analysis of this specimen are presented in Figure 55. Typical of all the STAGS nonlinear analyses performed for this study, correlation is excellent until the buckling load is reached, and it then degrades with increasing load. The analysis of specimen I16, however, has the worst postbuckling agreement with experiment of the three specimens which have been discussed. The value of $(b/t)_f$ for specimen I16, from Table 4, is 13.563, and for this relatively low value of flange width-to-thickness ratio, neglecting transverse shearing deformations by STAGS is probably in part what causes the STAGS

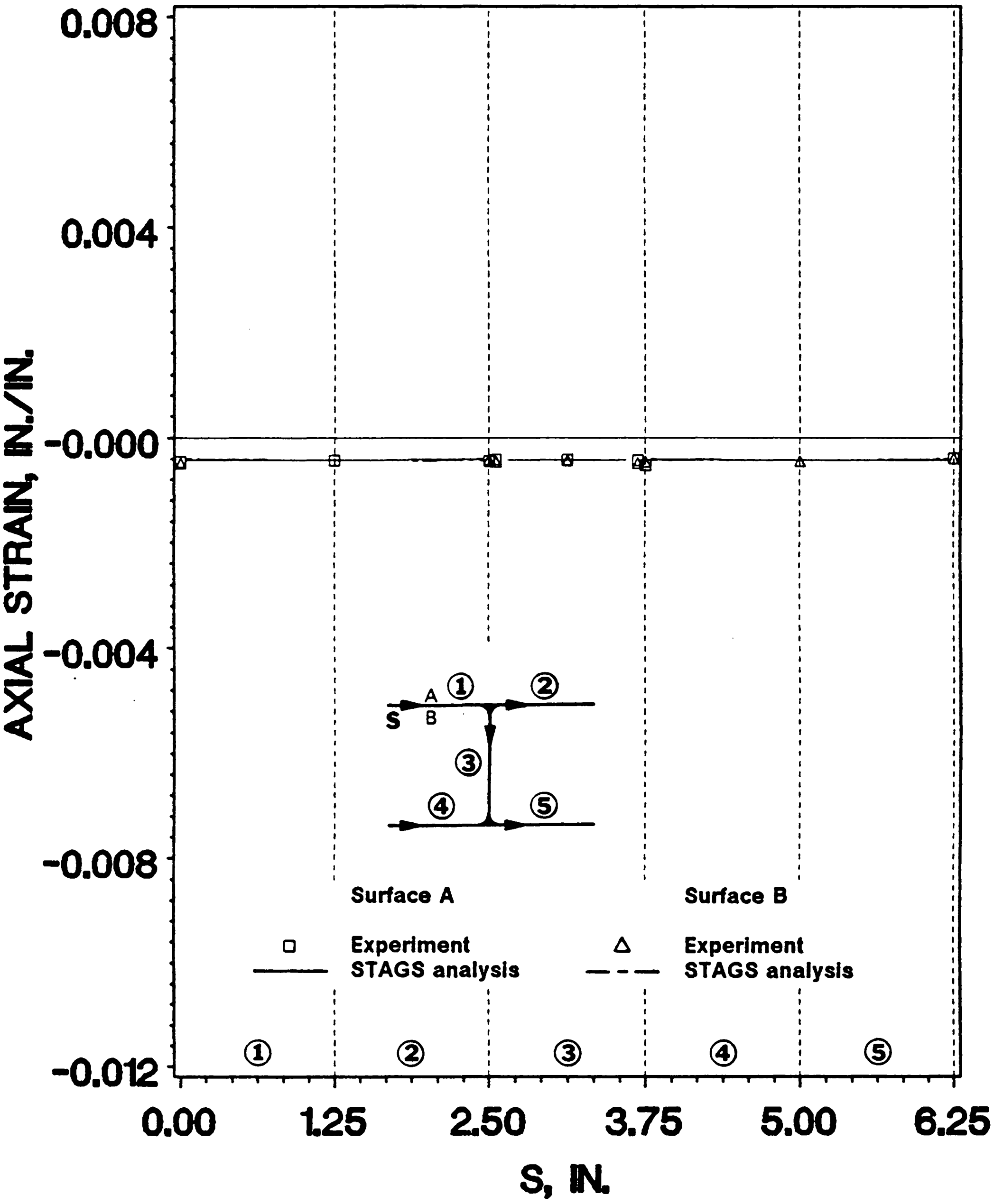

Figure 50. Axial surface strains for specimen I2 at P = 994.87 lb: experiment and STAGS nonlinear analysis at $l/3$, prior to buckling ($P/P_{cr} = 0.357$)

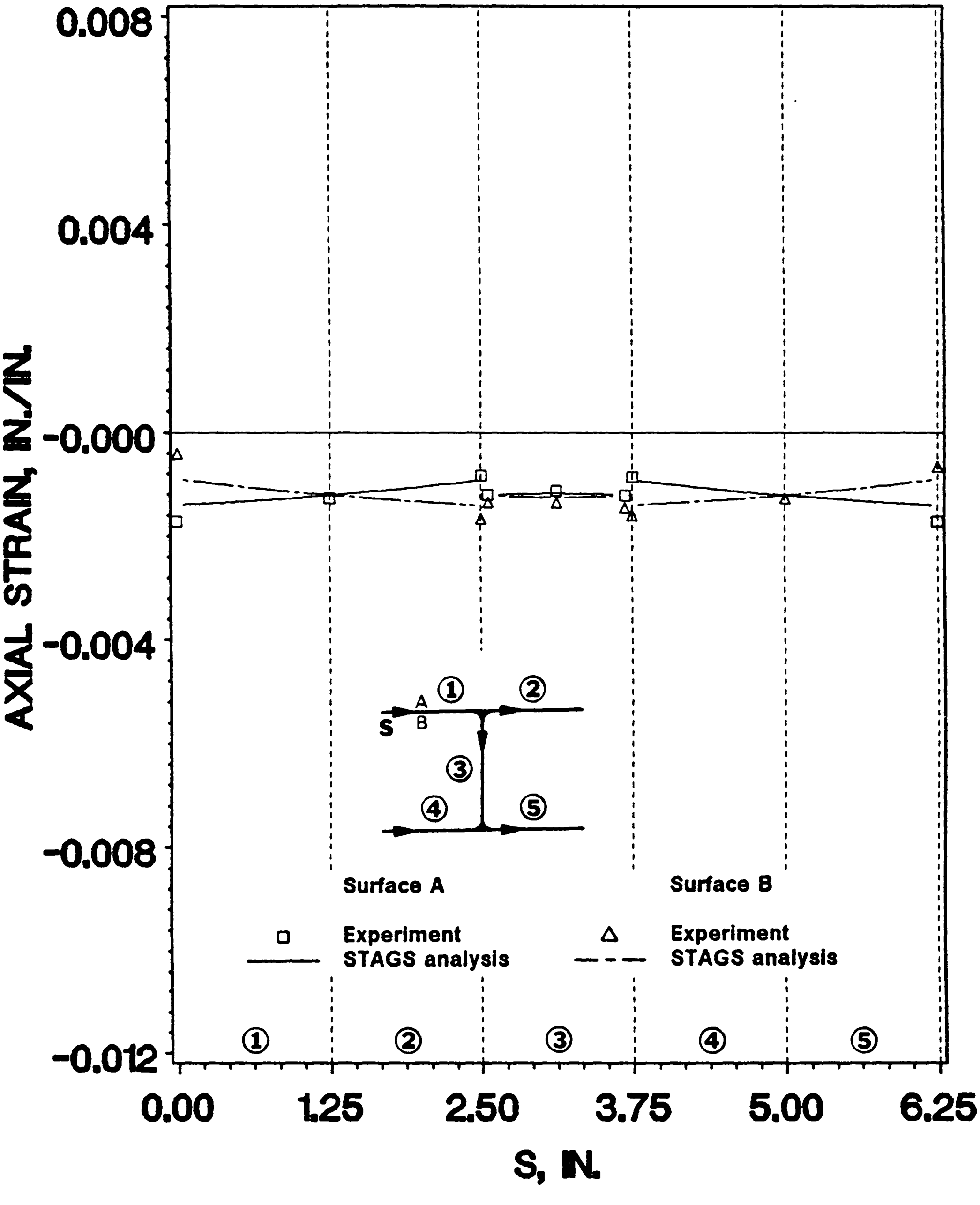

Figure 51. Axial surface strains for specimen I2 at P = 2772.79 lb: experiment and STAGS nonlinear analysis at $l/3$, near buckling load ($P/P_{cr} = 0.995$)

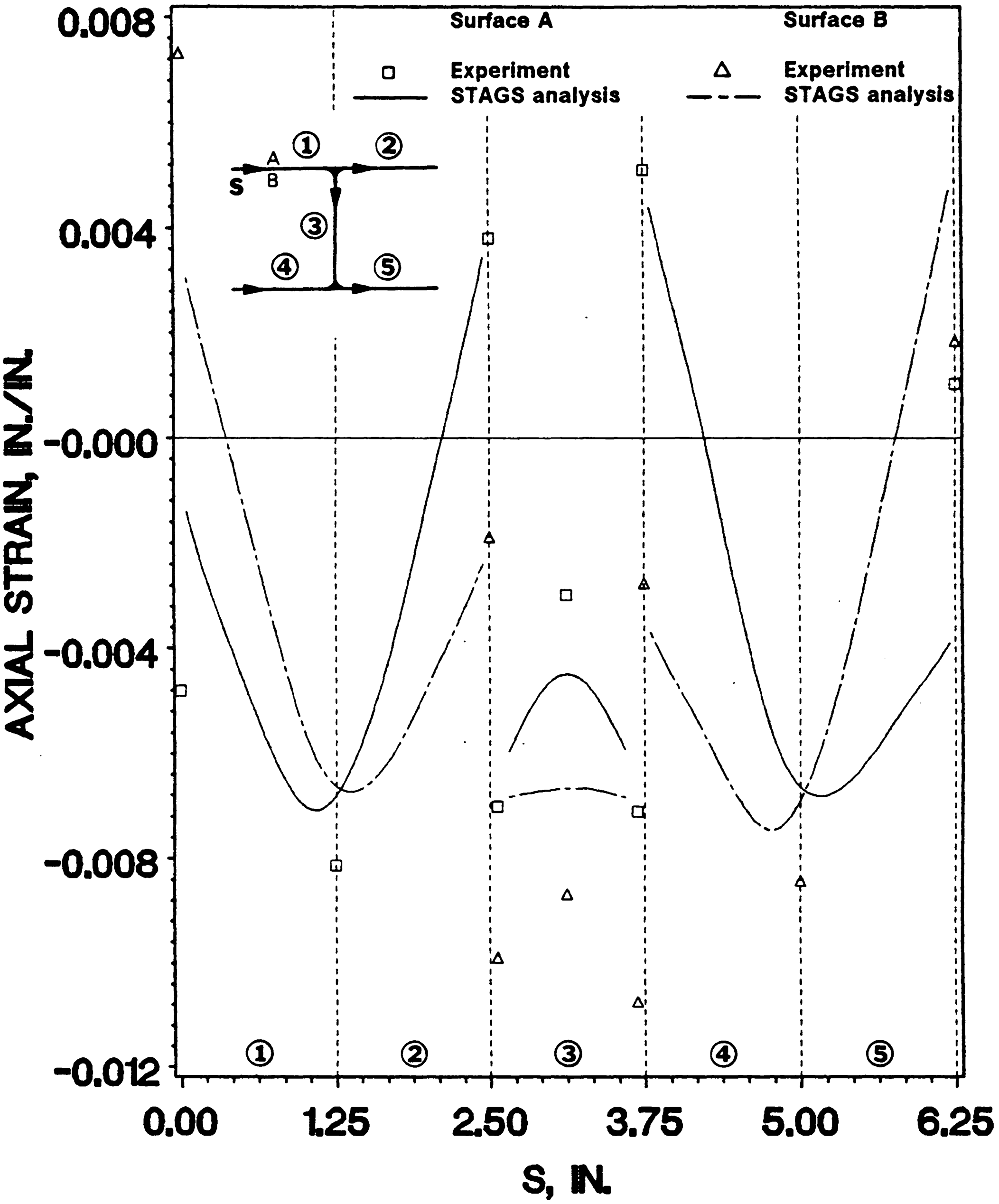

Figure 52. Axial surface strains for specimen I2 at P = 10289.02 lb: experiment and STAGS nonlinear analysis at $l/3$, at crippling load ($P_{cc}/P_{cr} = 3.693$)

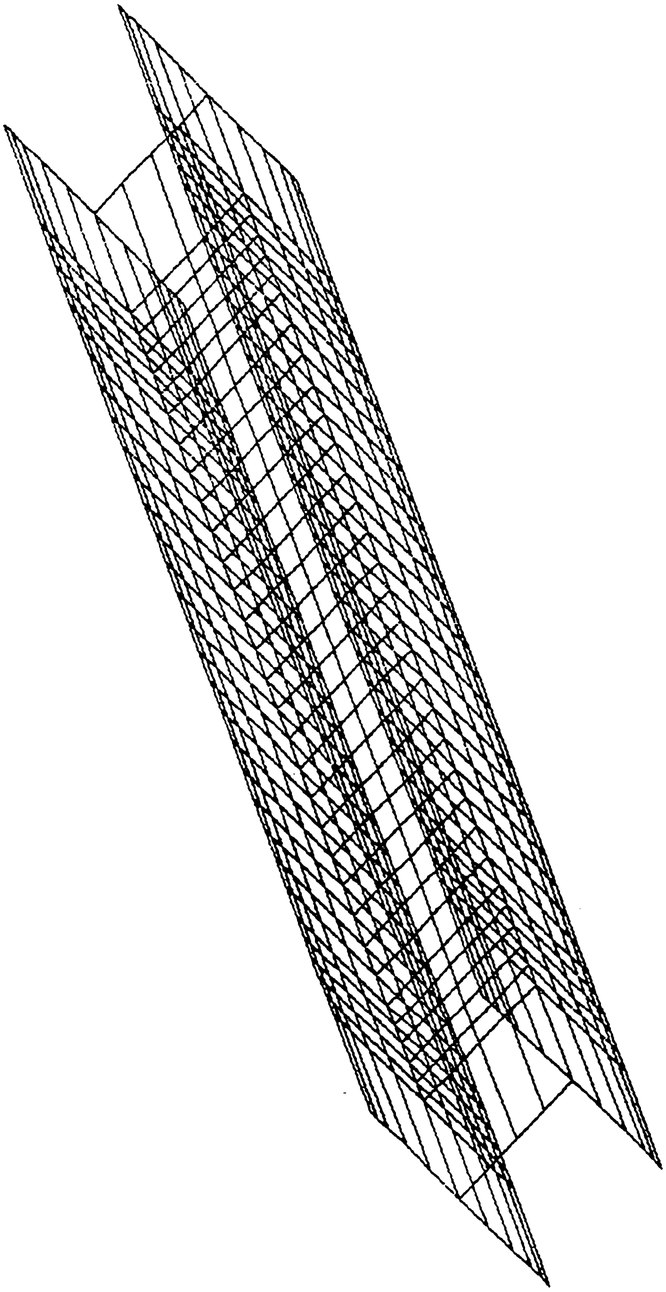

Figure 53. STAGS model geometry and finite element mesh for specimen I16

model to be considerably stiffer in postbuckling than the physical specimen. This behavior is similar to the response noted in the load-shortening diagram of specimen Z6 (Figure 42), which also has $(b/t)_f = 13.563$. The lack of postbuckling correlation is significantly greater, though, in specimen I16, which is an I-section made from the L16B layup, than it is for specimen Z6, which is a zee fabricated from the L16A stacking sequence. This difference is at least partly due to the damage which occurred in specimen I16 in postbuckling, as documented in Table 4, but might also be due to the differences in cross-sectional shape or layup between these two specimens. Since fairly good results were obtained from the analysis of another I-section, specimen I2, it seems likely that the lack of correlation between experiment and analysis visible in the postbuckled region of specimen I16 in Figure 55 as compared to the response of specimen Z6 in Figure 42 may be partly caused not by the I-section shape but by the presence of the L16B layup. The L16B layup differs from the L16A layup in having a higher percentage of 0° plies and also in having all the 0° plies grouped together at the center of the laminate. Incorrect modeling of the end conditions at the gage length ends of specimen I16 in the STAGS analysis could also account for some of the lack of agreement in Figure 55. As a final observation on this figure, the buckling load of 17050 lbs. obtained from STAGS is in very good agreement with the experimental value of 16536 lbs. for specimen I16.

The axial surface strain distributions for specimen I16 at an axial position of approximately $l/3$ are shown in Figures 56-58 for increasing values of compressive load. Cross-sectional strain distributions at a load of 7931.24 lbs are presented in Figure 56. Since this is a loading condition prior to buckling ($P/P_{cr} = 0.480$), a nearly uniform state of membrane strain is evident, and correlation between experiment and analysis is very good. At a load of $P = 16530.64$ lbs., which is roughly equal to the experimental buckling load ($P/P_{cr} = 1.000$), the correlation seen in Figure 57 between the axial surface strains recorded during the testing of specimen I16 and the strains determined by nonlinear analysis remains relatively good, although some discrepancies are visible at the free edges of flange shell units 4 and 5. When the crippling load is reached only 1200 pounds later ($P_{cc}/P_{cr} = 1.076$), the free edges of the flanges show very large differences between the values of surface strain observed in experiment and predicted by analysis, as shown in Figure 58. This lack

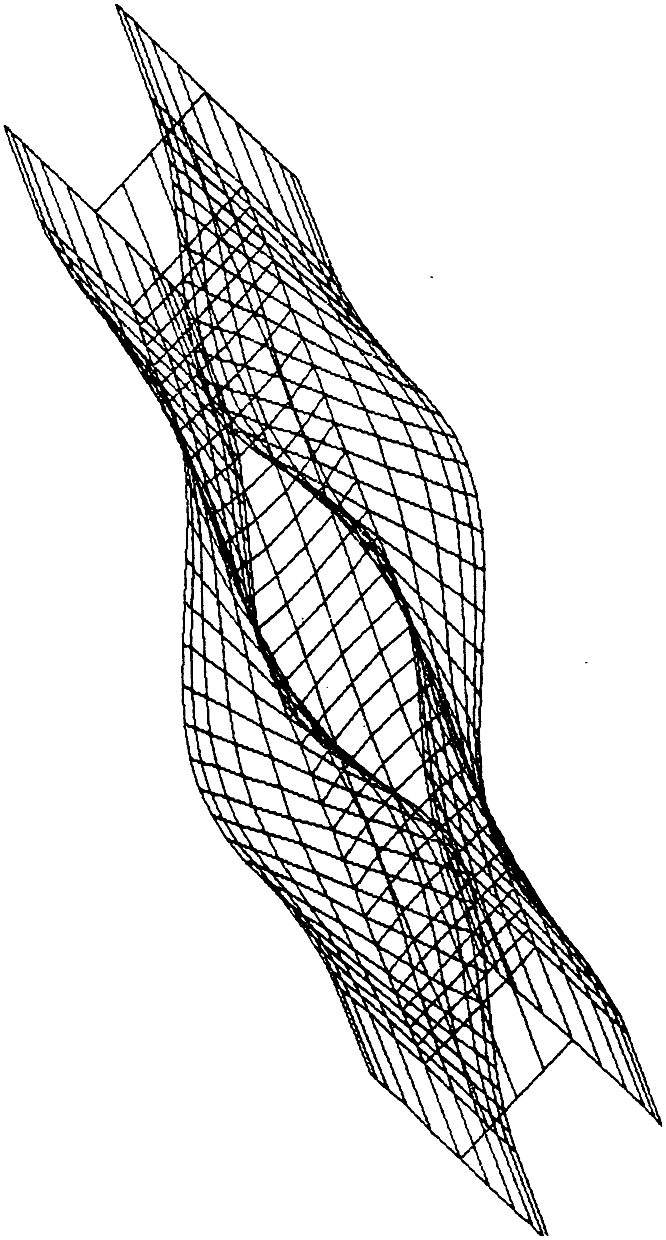

Figure 54. Buckling mode of specimen I16

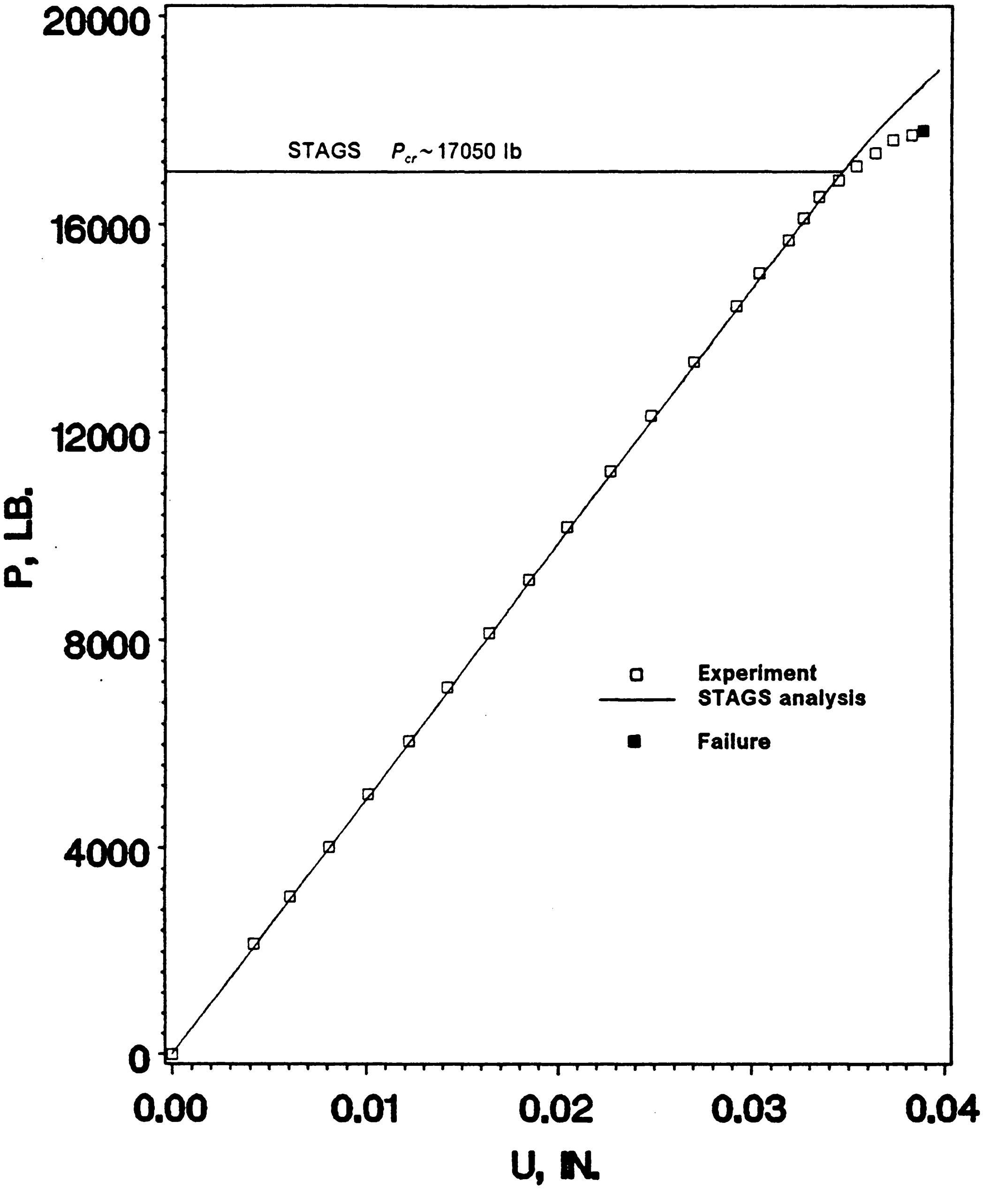

Figure 55. Load-shortening curves for specimen I16: experiment and STAGS nonlinear analysis

of correlation is probably mostly due to the damage which occurred in specimen I16 prior to crippling failure, as was mentioned earlier in reference to the load-shortening curves in Figure 55. The influence of transverse shearing effects in the flanges of the physical specimen, which causes the STAGS model to seem too stiff and thus to exhibit less flange bending than was experimentally observed, also probably contributes to the observed lack of correlation, as might the boundary condition modeling problem discussed previously. The difference between experiment and analysis noted in Figure 58 may also be partly due to the same sort of subtle differences in the axial locations of buckling wave crests between the analytical model and the physical specimen which were discussed in reference to specimen I2 in the last section.

4.5 Plane Stress Failure Analysis

As was mentioned in Section 4.3, a plane stress failure analysis was performed for each of the five specimens analyzed. The STAGS code was used to generate in-plane stress data at the load corresponding to the first observed damage event for each of specimens Z1, I2, I10, and I16. Since no detailed information about damage initiation within specimen Z6 was available, the STAGS in-plane stress data were obtained for this specimen at the crippling load. The in-plane stresses in principal material directions, σ_{11}, σ_{22}, and σ_{12}, where the 1-direction is parallel to the fibers and the 2-direction perpendicular to the fibers, were obtained at the top and bottom of each ply through the thickness of the laminate at the centroid of selected finite elements in each of the nonlinear models. The locations of all of the finite elements chosen for failure analysis were selected consistent with the observation in Ref. 8 and in the present study that failure seems to initiate at either the corners or the flange free edges of the stiffener specimens. For the two zee section specimens analyzed, Z1 and Z6, the elements which were evaluated for failure were chosen from one of the corners and from the flange nearest that corner at a buckle wave crest. For the three I-section specimens I2, I10, and I16, elements were selected for analysis at a buckle wave crest from the web

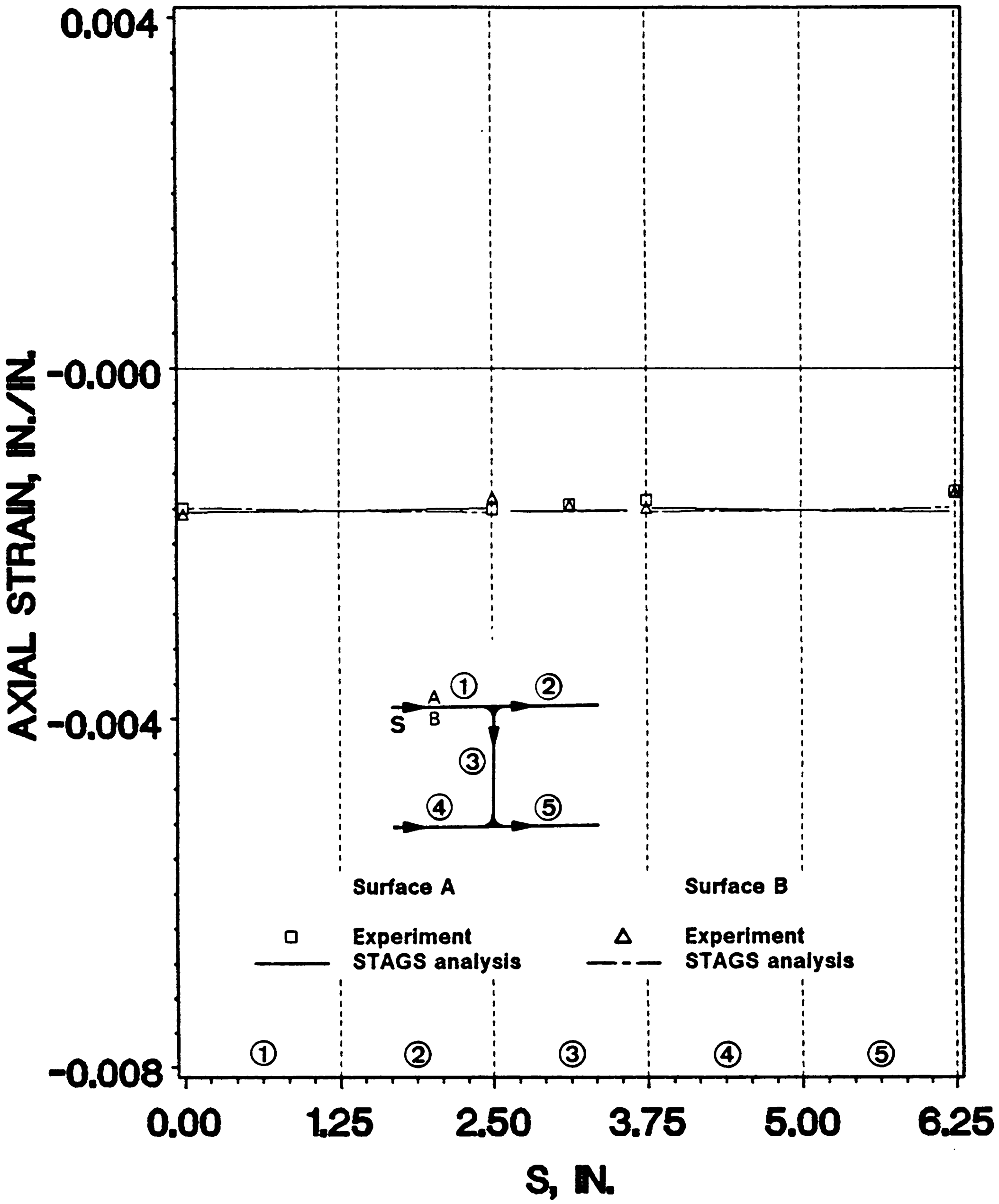

Figure 56. Axial surface strains for specimen 116 at P = 7931.24 lb: experiment and STAGS nonlinear analysis near $l/3$, prior to buckling ($P/P_{cr} = 0.480$)

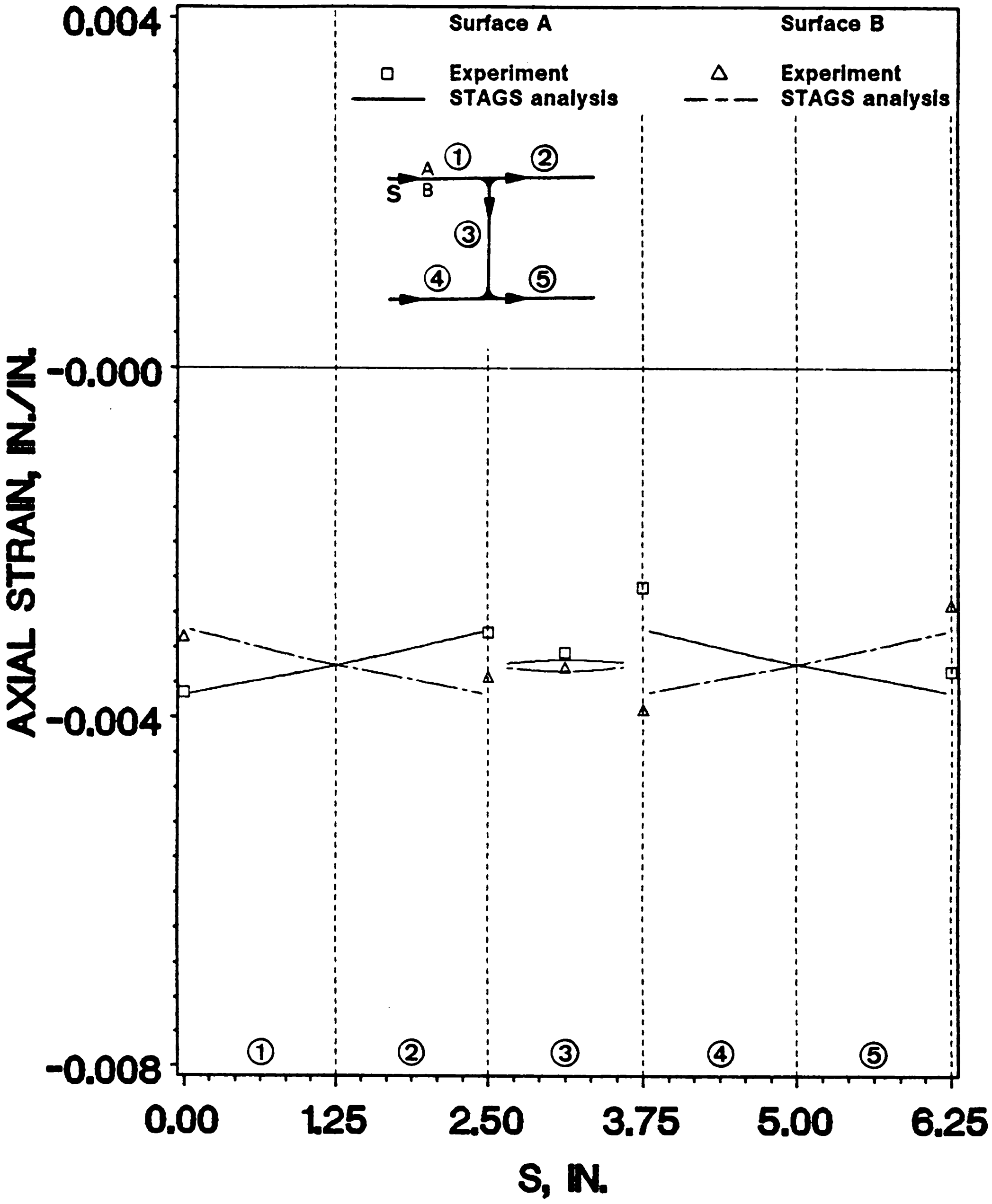

Figure 57. Axial surface strains for specimen I16 at P = 16530.64 lb: experiment and STAGS nonlinear analysis near $l/3$, at buckling load ($P/P_{cr} = 1.000$)

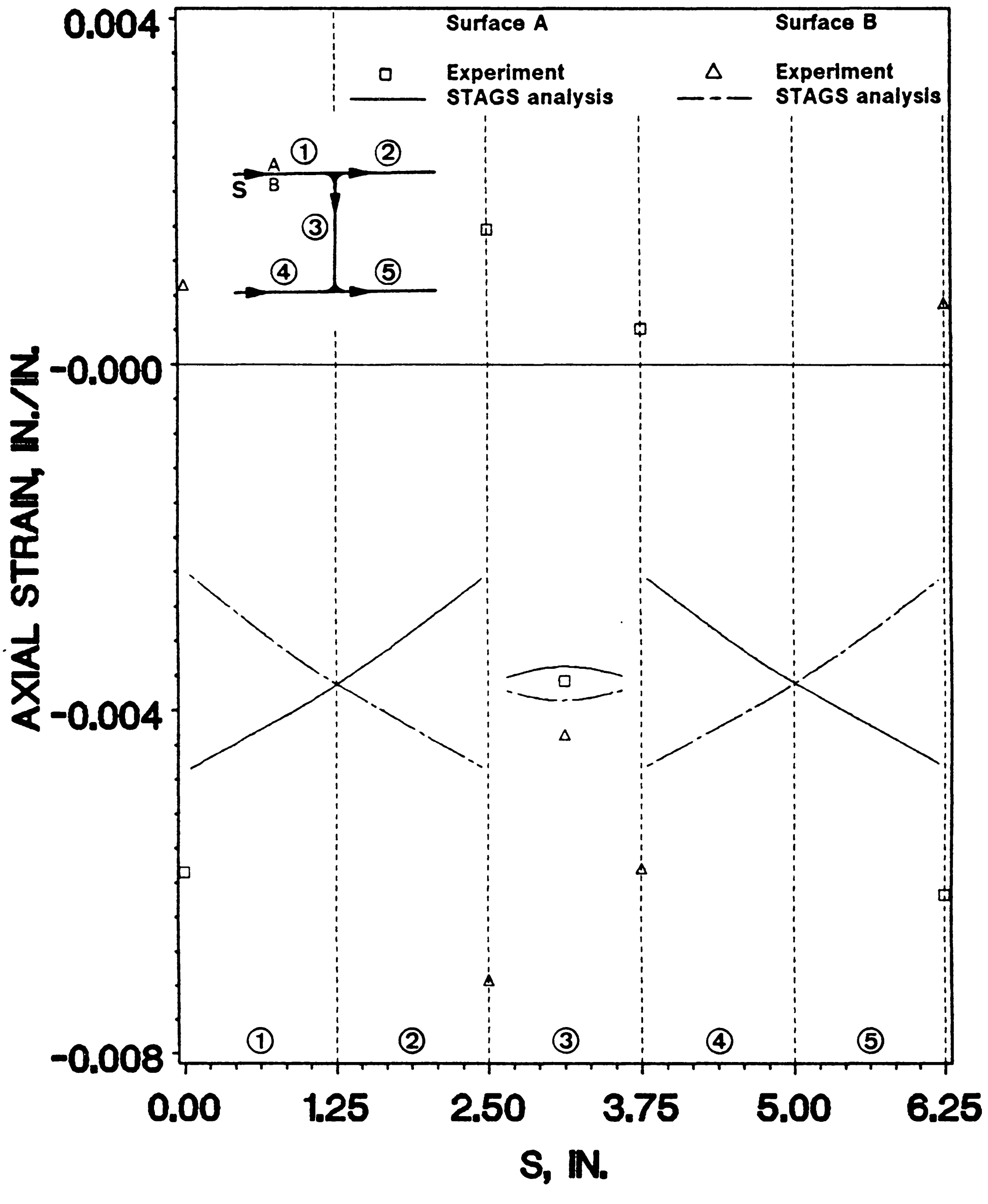

Figure 58. Axial surface strains for specimen 116 at P = 17797.55 lb: experiment and STAGS nonlinear analysis near $l/3$, at crippling load ($P_{cc}/P_{cr} = 1.076$)

near one of the corners and from the two flanges which were joined to the web at that corner. For all five specimens, the elements chosen for study were located at or very near the axial location of experimental failure.

The in-plane stress data described above were used to evaluate six different plane stress failure criteria. The failure criteria used in the current work are the Tsai-Hill and Tsai-Wu (tensor polynomial) failure criteria specialized to the plane stress condition, and the four quadratic plane stress failure criteria proposed by Hashin[18]. The Hashin criteria are the tensile fiber, compressive fiber, tensile matrix, and compressive matrix modes. The formulas for these failure criteria are given in Appendix A. The left-hand side of each of these failure criteria is a function involving material strength parameters and in-plane stresses; this function will have a value less than one prior to failure, greater than one after failure, and equal to unity at failure. Let X denote a fiber-direction strength, Y a strength in the direction perpendicular to the fibers, and S the in-plane shear strength, and let subscripts t and c denote tension and compression, respectively. The material strength parameters used in the present study are $X_t = 210.0$ ksi, $X_c = -210.0$ ksi, $Y_t = 7.54$ ksi, $Y_c = -29.9$ ksi, and $S = 13.5$ ksi, and were obtained from Ref. 19 for the AS/3501 graphite-epoxy material system, which is similar to the AS4/3502 graphite-epoxy utilized in the present study. For each of specimens Z1, Z6, I2, I10, and I16, the in-plane stresses at the top and bottom surface of each lamina through the thickness of the laminate at the centroid of every selected finite element were substituted into the appropriate plane stress failure criteria. The results of this process are presented in Table 11. For each specimen analyzed, Table 11 lists the load at which the failure analysis was performed, the maximum value of each failure criterion, the orientation of the ply in which the maximum occurred, and the general location within the specimen of the finite element in which the maximum was found. Results are given only for the compressive fiber and matrix modes of Hashin and for the Tsai-Hill failure criterion. The tensile fiber and matrix mode criteria were not critical, since the two in-plane normal stresses σ_{11} and σ_{22} were usually compressive, and these criteria always yielded results far less than 1.0. The Tsai-Wu (tensor polynomial) criterion also consistently produced values well below 1.0.

Table 11. **Results of plane stress failure analysis**

Specimen designation	Load P, lb.	Failure criterion[a]	Max. value of criterion[b], dimensionless	Ply orientation for max. value[c]	Location of max. value
Z1	8375	CFM	0.805	0°	Corner
		CMM	0.544	45°	Flange free edge
		THT	0.667	45°	Flange free edge
Z6[d]	12121	CFM	1.138	0°	Corner
		CMM	0.935	45°	Flange free edge
		THT	1.300	0°	Corner
I2	10000	CFM	1.348	0°	Web near corner
		CMM	1.445	45°	Web near corner
		THT	1.915	45°	Web near corner
I10	18750	CFM	0.881	0°	Flange near corner
		CMM	0.583	45°	Flange free edge
		THT	0.830	45°	Flange free edge
I16	17570	CFM	0.990	0°	Entire flange
		CMM	0.940	45°	Flange free edge
		THT	1.238	45°	Flange free edge

[a] The failure criteria listed are:

CFM -- Hashin's compressive fiber mode failure criterion
CMM -- Hashin's compressive matrix mode failure criterion
THT -- Tsai-Hill failure criterion

The formulas for these criteria are listed in Appendix A.

[b] The material strength parameters used are $X_t = 210.0$ ksi, $X_c = -210.0$ ksi, $Y_t = 7.54$ ksi, $Y_c = -29.9$ ksi, and $S = 13.5$ ksi.

[c] Orientation of ply in which the maximum value of the criterion listed occurred.

[d] This specimen was tested in Ref. 8 and was analyzed at the crippling load. The failure analyses for the other specimens shown were performed at the load corresponding to the first damage event within each specimen.

The results given by the compressive fiber and matrix mode and Tsai-Hill failure criteria are most conservative for specimen I2, which has a flange width-to-thickness ratio of 27.625. The maximum value of each criterion for this specimen is greater than unity, which implies that all of these criteria predict failure to occur at a load lower than that at which damage actually began to initiate within specimen I2. For the other four specimens analyzed, which have flange width-to-thickness ratios of 13.563, the majority of the maximum failure indices in Table 11 are less than 1.0, indicating no failure. Thus, failure or damage is predicted to occur at a load greater than that observed experimentally. Since the experimental observations suggest that the crippling failure process of an I-section specimen with large flange width-to-thickness ratio $(b/t)_f$ is initiated in the corners of the specimen, it may be that the lack of fidelity in the modeling of the corner regions of specimen I2 in the STAGS analysis accounts, at least in part, for the inaccuracy of the damage prediction. For specimens with smaller flange width-to-thickness ratios, it is likely that through-the-thickness deformations and interlaminar stresses are significant, but the lack of an estimate of the thickness-direction stress components precludes an evaluation of failure initiation by delamination. Thus, the inaccuracy of the failure analyses of specimens Z1, Z6, I10, and I16 may be due to the inability to evaluate delamination.

While the failure initiation loads and modes predicted by this plane stress failure analysis may not be very accurate, the cross-sectional locations of the maximum failure criteria values within each specimen analyzed correlate well with the experimental observations of failure locations in Chapter 3. For specimen I2, analysis predicts the first damage event to occur in the web near the juncture of the web and flanges which, for the relatively rough finite element modeling in the corners, is equivalent to a failure occurring in the corner, and this is also believed to be the site of failure initiation during the testing of the specimen. In specimens I10 and I16, the first damage event was suspected to be due to a delamination at some location within a flange, and, although the correct mode of damage (delamination) cannot be predicted by plane stress failure criteria, Table 11 shows that the failure indices CFM and THT are near critical in the flanges of these specimens. The largest value of a failure index from the analysis of specimen Z1 occurs in a corner in the compressive fiber mode. Like the three I-section specimens, the location of damage initiation predicted for specimen Z1 by plane stress failure analysis is in agreement with experimental observations, but the mode predicted is incorrect. Damage seemed to initiate in specimen Z1 due to a corner opening delamination. No experimental damage initiation information was available for specimen Z6.

Of the three failure criteria listed in Table 11, the Tsai-Hill criterion tends to be the most conservative. The average of the five maximum values of this criterion reported in Table 11 is 1.190, which indicates that for these specimens, the Tsai-Hill failure criterion generally underestimates the load at which the first damage event occurs. The compressive matrix mode of Hashin, in contrast, tends to overestimate the damage loads of the specimens analyzed, with an average maximum value of 0.889, and is the most nonconservative criterion of the three criteria tabulated. Hashin's compressive fiber mode criterion, although it is somewhat nonconservative in specific cases, correlates fairly well with experimental observations for the specimens studied in the present work; the average of the five maximum values given in Table 11 is 1.032. Thus, it would seem that if interlaminar stress information is not available, a reasonable approximation of the load and location of damage initiation or crippling failure for stiffeners with geometries and material properties similar to those in this study might be obtained from Hashin's compressive fiber mode failure criterion. Reference to equation (A.2) in Appendix A shows that this criterion is in fact just a simple maximum fiber-direction compressive stress criterion, $\sigma_{11}/X_c = 1$. It must be emphasized, however, that plane stress failure criteria are less than optimum when composite stiffener crippling is considered, as such criteria are unable to predict important modes of damage initiation due to delamination.

Chapter 5

Interlaminar Stress Postprocessor Development

A postprocessor to the STAGS code, which was to calculate interlaminar stresses from the finite element nodal solution data, was partially developed during the current research. The derivation of the formulas for the interlaminar stresses is given here, followed by a description of a numerical method for deriving high order derivative information from discrete data via the Discrete Fourier Transform and the Fourier series. High order derivatives of the displacements are required for the interlaminar stress equations.

5.1 Derivation of the Interlaminar Stress Equations

Equations for the interlaminar stresses σ_z, σ_{zx}, and σ_{zy} are derived for a flat laminated plate of uniform thickness t as shown in Figure 59. The plate is assumed to be mid-plane symmetric, and the mid-plane coincides with the x-y plane of a right-handed Cartesian coordinate system (x, y, z). The N component laminae are parallel to the x-y plane and are assumed to be homogeneous and orthotropic. Laminae are numbered 1 through N from the bottom ($z = -t/2$) to the top ($z = +t/2$) of the laminate. Adjacent laminae are assumed to be perfectly bonded to each other. The interface between laminae k and $k+1$, where $k = 1, 2, \ldots, \mathrm{N}-1$, is identified as the $k+1$ interface and occurs at the location $z = z_{k+1}$. The thickness of the k^{th} lamina is $t_k = z_{k+1} - z_k$. Let u, v, and w denote the respective displacements in the x-, y-, and z-coordinate directions. In what follows, lamina dependent quantities include a superscripted lamina number enclosed in parentheses; laminate independent variables have no superscript.

The derivation of the interlaminar stress equations begins with the elasticity equations of equilibrium for a typical lamina k within the laminated plate. Including the influence of the product of in-plane stresses and out-of-plane rotations on the z-direction equilibrium equation, these equations are

$$\sigma^{(k)}_{x,x} + \sigma^{(k)}_{yx,y} + \sigma^{(k)}_{zx,z} = 0 \tag{5.1}$$

$$\sigma^{(k)}_{xy,x} + \sigma^{(k)}_{y,y} + \sigma^{(k)}_{zy,z} = 0 \tag{5.2}$$

$$\sigma^{(k)}_{xz,x} + \sigma^{(k)}_{yz,y} + \sigma^{(k)}_{z,z} + \sigma^{(k)}_{x} w_{,xx} + 2\sigma^{(k)}_{xy} w_{,xy} + \sigma^{(k)}_{y} w_{,yy} = 0\,, \tag{5.3}$$

in which body forces are neglected, and the comma convention is used to denote partial differentiation. Equations (5.1-3) are integrated through the thickness from z_k to z_{k+1} to yield

$$N^{(k)}_{x,x} + N^{(k)}_{xy,y} + t^{(k)}_{2} - t^{(k)}_{1} = 0 \tag{5.4}$$

$$N^{(k)}_{xy,x} + N^{(k)}_{y,y} + s^{(k)}_{2} - s^{(k)}_{1} = 0 \tag{5.5}$$

$$Q^{(k)}_{x,x} + Q^{(k)}_{y,y} + N^{(k)}_{x} w_{,xx} + 2N^{(k)}_{xy} w_{,xy} + N^{(k)}_{y} w_{,yy} + p^{(k)}_{2} - p^{(k)}_{1} = 0 \tag{5.6}$$

where the lamina stress resultants are defined by

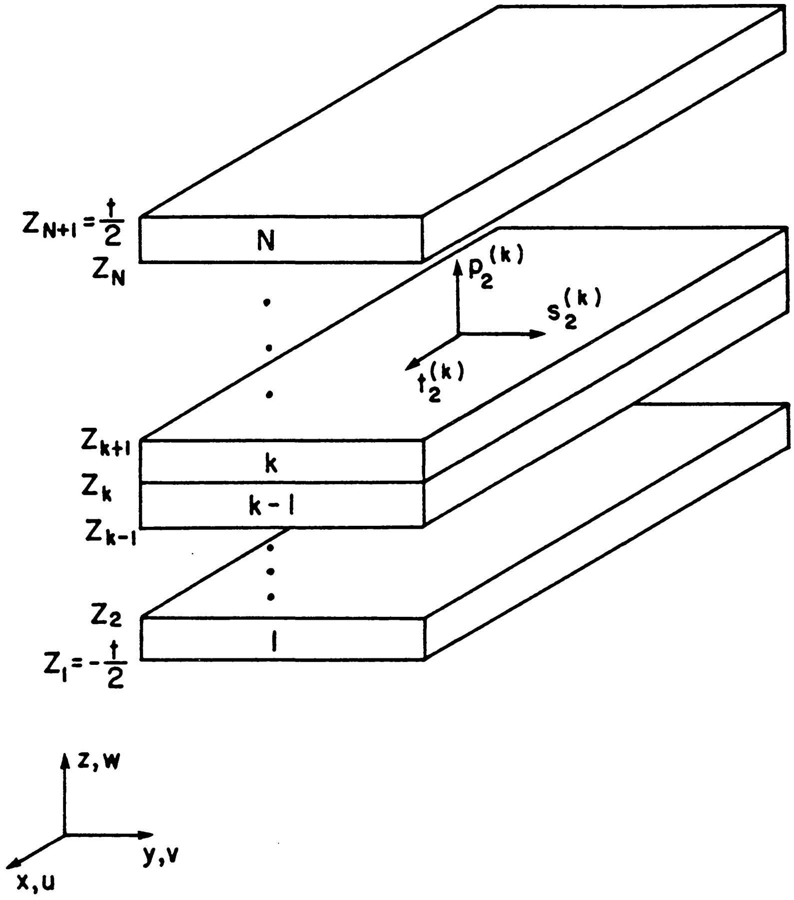

Figure 59. Laminated plate and interlaminar stresses at k + 1 interface

$$(N_x, N_y, N_{xy}, Q_x, Q_y)^{(k)} = \int_{z_k}^{z_{k+1}} (\sigma_x, \sigma_y, \sigma_{xy}, \sigma_{xz}, \sigma_{yz})^{(k)} dz \tag{5.7}$$

and the surface tractions $t^{(k)}$, $s^{(k)}$, and $p^{(k)}$ are defined by

$$(t_2, s_2, p_2)^{(k)} = (\sigma_{zx}, \sigma_{zy}, \sigma_z)^{(k)} \quad \text{at} \quad z = z_{k+1} \tag{5.8}$$

$$(t_1, s_1, p_1)^{(k)} = (\sigma_{zx}, \sigma_{zy}, \sigma_z)^{(k)} \quad \text{at} \quad z = z_k. \tag{5.9}$$

The tractions on the upper surface ($z = z_{k+1}$) of the k^{th} lamina are shown in Figure 59. The out-of-plane displacement w is assumed to be independent of the thickness coordinate z, consistent with plate theory.

It is convenient to eliminate the derivatives of the shear resultants $Q^{(k)}_{x,x}$ and $Q^{(k)}_{y,y}$ from equation (5.6). This is done by multiplying equations (5.1) and (5.2) by z and then integrating them through the thickness of the lamina from z_k to z_{k+1} to give

$$M^{(k)}_{x,x} + M^{(k)}_{yx,y} + z_{k+1}t^{(k)}_2 - z_k t^{(k)}_1 - Q^{(k)}_x = 0 \tag{5.10}$$

$$M^{(k)}_{xy,x} + M^{(k)}_{y,y} + z_{k+1}s^{(k)}_2 - z_k s^{(k)}_1 - Q^{(k)}_y = 0 \tag{5.11}$$

where the lamina moment resultants are defined by

$$(M_x, M_y, M_{xy})^{(k)} = \int_{z_k}^{z_{k+1}} (\sigma_x, \sigma_y, \sigma_{xy})^{(k)} \, z \, dz \, . \tag{5.12}$$

Differentiating equation (5.10) with respect to x and (5.11) with respect to y, and then substituting the resulting expressions for $Q^{(k)}_{x,x}$ and $Q^{(k)}_{y,y}$ into equation (5.6), we obtain

$$\begin{aligned}M^{(k)}_{x,xx} + 2M^{(k)}_{xy,xy} + M^{(k)}_{y,yy} + (z_{k+1}t_2^{(k)} - z_k t_1^{(k)})_{,x} + (z_{k+1}s_2^{(k)} - z_k s_1^{(k)})_{,y} \\ + N_x^{(k)} w_{,xx} + 2N_{xy}^{(k)} w_{,xy} + N_y^{(k)} w_{,yy} + p_2^{(k)} - p_1^{(k)} = 0\,.\end{aligned} \tag{5.13}$$

Equations (5.4), (5.5), and (5.13) form the set of lamina equilibrium equations from which the interlaminar stress formulas will be derived.

For a perfectly bonded laminate, interfacial continuity of the lamina surface tractions exists and may be expressed as

$$t_2^{(k)} = t_1^{(k+1)},\ s_2^{(k)} = s_1^{(k+1)},\ p_2^{(k)} = p_1^{(k+1)}, \qquad k = 1,2,\ldots\ ,\mathrm{N}-1\,. \tag{5.14}$$

Keeping these continuity conditions in mind, and summing equations (5.4), (5.5), and (5.13) from the first to the k^{th} lamina of the laminate, expressions for the interlaminar stresses at the $k+1^{st}$ interface are obtained in terms of derivatives of the in-plane lamina resultants and the out-of-plane displacement. These interlaminar stress equations are

$$t_2^{(k)} = t_1^{(1)} - \left\{ \left[\sum_{l=1}^{k} N_x^{(l)}\right]_{,x} + \left[\sum_{l=1}^{k} N_{xy}^{(l)}\right]_{,y} \right\} \tag{5.15}$$

$$s_2^{(k)} = s_1^{(1)} - \left\{ \left[\sum_{l=1}^{k} N_{xy}^{(l)}\right]_{,x} + \left[\sum_{l=1}^{k} N_y^{(l)}\right]_{,y} \right\} \tag{5.16}$$

$$
\begin{aligned}
p_2^{(k)} = p_1^{(1)} &- \left\{ \left[\sum_{l=1}^{k} M_x^{(l)} \right]_{,xx} + 2 \left[\sum_{l=1}^{k} M_{xy}^{(l)} \right]_{,xy} + \left[\sum_{l=1}^{k} M_y^{(l)} \right]_{,yy} \right\} \\
&- \left\{ \left[\sum_{l=1}^{k} N_x^{(l)} \right] w_{,xx} + 2 \left[\sum_{l=1}^{k} N_{xy}^{(l)} \right] w_{,xy} + \left[\sum_{l=1}^{k} N_y^{(l)} \right] w_{,yy} \right\} \\
&- \left[z_{k+1} t_2^{(k)} + \frac{t}{2} t_1^{(1)} \right]_{,x} - \left[z_{k+1} s_2^{(k)} + \frac{t}{2} s_1^{(1)} \right]_{,y} .
\end{aligned}
\tag{5.17}
$$

The derivative terms $t_{2,x}^{(k)}$ and $s_{2,y}^{(k)}$ in equation (5.17) are eliminated by differentiation and substitution of equations (5.15) and (5.16) into (5.17).

Hooke's law for classical laminated plate theory may be used to express the partial sums of lamina stress and moment resultants in equations (5.15-17) in terms of laminate resultants. If contracted notation is adopted so that for the in-plane stresses $\sigma_1 = \sigma_x$, $\sigma_2 = \sigma_y$, and $\sigma_6 = \sigma_{xy}$, for the mid-plane strains $\varepsilon_1^o = \varepsilon_x^o$, $\varepsilon_2^o = \varepsilon_y^o$, and $\varepsilon_6^o = \gamma_{xy}^o$, and for the mid-plane curvatures $\kappa_1 = \kappa_x$, $\kappa_2 = \kappa_y$, and $\kappa_6 = \kappa_{xy}$, then Hooke's law for the k^{th} lamina in classical laminated plate theory may be written

$$
\sigma_i^{(k)} = \sum_j \overline{Q}_{ij}^{(k)} (\varepsilon_j^o + z\kappa_j) , \qquad i, j = 1,2,6 \tag{5.18}
$$

where the transformed reduced stiffnesses for the k^{th} lamina are designated by $\overline{Q}_{ij}^{(k)}$. Substituting this relationship into equation (5.7) for the lamina stress resultants and (5.12) for the lamina moment resultants yields

$$
N_i^{(k)} = \sum_j (a_{ij}^{(k)} \varepsilon_j^o + b_{ij}^{(k)} \kappa_j) \tag{5.19}
$$

$$M_i^{(k)} = \sum_j (b_{ij}^{(k)} \varepsilon_j^{o} + d_{ij}^{(k)} \kappa_j) \tag{5.20}$$

with

$$\left[a_{ij}^{(k)}, b_{ij}^{(k)}, d_{ij}^{(k)}\right] = \left[(z_{k+1} - z_k),\ \frac{1}{2}(z_{k+1}^2 - z_k^2),\ \frac{1}{3}(z_{k+1}^3 - z_k^3)\right] \overline{Q}_{ij}^{(k)}. \tag{5.21}$$

Total laminate resultants may be obtained by summing equations (5.19) and (5.20) over all N laminae giving

$$N_i = \sum_j (A_{ij} \varepsilon_j^{o} + B_{ij} \kappa_j) \tag{5.22}$$

$$M_i = \sum_j (B_{ij} \varepsilon_j^{o} + D_{ij} \kappa_j) \tag{5.23}$$

in which

$$[A_{ij}, B_{ij}, D_{ij}] = \sum_{k=1}^{N} \left[a_{ij}^{(k)}, b_{ij}^{(k)}, d_{ij}^{(k)}\right] . \tag{5.24}$$

However, since the laminated plate under consideration is assumed to be mid-plane symmetric, the coupling coefficients B_{ij} in equations (5.22) and (5.23) vanish, and thus the inverted forms of these equations become

$$\varepsilon_i^{o} = \sum_j A_{ij}^{-1} N_j \tag{5.25}$$

$$\kappa_i = \sum_j D_{ij}^{-1} M_j \, . \tag{5.26}$$

Equations (5.25) and (5.26) are used to eliminate the mid-plane strains and curvatures in equations (5.19) and (5.20), and the resulting equations are summed over the portion of the laminate from the first to the k^{th} lamina to yield

$$\sum_{l=1}^{k} N_i^{(l)} = \sum_j (A_{ij}^{(k)} N_j + B_{ij}^{(k)} M_j) \tag{5.27}$$

$$\sum_{l=1}^{k} M_i^{(l)} = \sum_j (C_{ij}^{(k)} N_j + D_{ij}^{(k)} M_j) \tag{5.28}$$

in which

$$A_{im}^{(k)} = \sum_j \left[\sum_{l=1}^{k} a_{ij}^{(l)} \right] A_{jm}^{-1} \tag{5.29}$$

$$B_{im}^{(k)} = \sum_{j} \left[\sum_{l=1}^{k} b_{ij}^{(l)} \right] D_{jm}^{-1} \tag{5.30}$$

$$C_{im}^{(k)} = \sum_{j} \left[\sum_{l=1}^{k} b_{ij}^{(l)} \right] A_{jm}^{-1} \tag{5.31}$$

$$D_{im}^{(k)} = \sum_{j} \left[\sum_{l=1}^{k} d_{ij}^{(l)} \right] D_{jm}^{-1} \tag{5.32}$$

and where i, j, and m take on the values 1, 2, and 6.

Substitution of equations (5.27) and (5.28) into the partial sums of equations (5.15-17) gives the desired interlaminar stress formulas. These formulas are written in the form

$$t_2^{(k)} = t_1^{(1)} - \underset{\sim}{A}_{k1}^{T} \underset{\sim}{N}_{,x} - \underset{\sim}{B}_{k1}^{T} \underset{\sim}{M}_{,x} - \underset{\sim}{A}_{k6}^{T} \underset{\sim}{N}_{,y} - \underset{\sim}{B}_{k6}^{T} \underset{\sim}{M}_{,y} \tag{5.33}$$

$$s_2^{(k)} = s_1^{(1)} - \underset{\sim}{A}_{k6}^{T} \underset{\sim}{N}_{,x} - \underset{\sim}{B}_{k6}^{T} \underset{\sim}{M}_{,x} - \underset{\sim}{A}_{k2}^{T} \underset{\sim}{N}_{,y} - \underset{\sim}{B}_{k2}^{T} \underset{\sim}{M}_{,y} \tag{5.34}$$

$$\begin{aligned} p_2^{(k)} = p_1^{(1)} &- (z_{k+1} + \frac{t}{2})[t_{1,x}^{(1)} + s_{1,y}^{(1)}] \\ &- \underset{\sim}{E}_{k1}^{T} \underset{\sim}{N}_{,xx} - 2\underset{\sim}{E}_{k6}^{T} \underset{\sim}{N}_{,xy} - \underset{\sim}{E}_{k2}^{T} \underset{\sim}{N}_{,yy} - \underset{\sim}{F}_{k1}^{T} \underset{\sim}{M}_{,xx} - 2\underset{\sim}{F}_{k6}^{T} \underset{\sim}{M}_{,xy} - \underset{\sim}{F}_{k2}^{T} \underset{\sim}{M}_{,yy} \\ &- w_{,xx}[\underset{\sim}{A}_{k1}^{T} \underset{\sim}{N} + \underset{\sim}{B}_{k1}^{T} \underset{\sim}{M}] - 2w_{,xy}[\underset{\sim}{A}_{k6}^{T} \underset{\sim}{N} + \underset{\sim}{B}_{k6}^{T} \underset{\sim}{M}] - w_{,yy}[\underset{\sim}{A}_{k2}^{T} \underset{\sim}{N} + \underset{\sim}{B}_{k2}^{T} \underset{\sim}{M}] \end{aligned} \tag{5.35}$$

where $k = 1, 2, \dots, N$. The 3 × 1 laminate resultant vectors in equations (5.33-35) are defined by

$$\underset{\sim}{N} = \begin{Bmatrix} N_x \\ N_y \\ N_{xy} \end{Bmatrix}, \quad \underset{\sim}{M} = \begin{Bmatrix} M_x \\ M_y \\ M_{xy} \end{Bmatrix} \tag{5.36}$$

and the 3 × 1 coefficient vectors by

$$\underset{\sim}{A}_{ki} = \begin{Bmatrix} A_{i1}^{(k)} \\ A_{i2}^{(k)} \\ A_{i6}^{(k)} \end{Bmatrix}, \quad \underset{\sim}{B}_{ki} = \begin{Bmatrix} B_{i1}^{(k)} \\ B_{i2}^{(k)} \\ B_{i6}^{(k)} \end{Bmatrix}, \quad \underset{\sim}{E}_{ki} = \begin{Bmatrix} C_{i1}^{(k)} - z_{k+1}A_{i1}^{(k)} \\ C_{i2}^{(k)} - z_{k+1}A_{i2}^{(k)} \\ C_{i6}^{(k)} - z_{k+1}A_{i6}^{(k)} \end{Bmatrix}, \quad \underset{\sim}{F}_{ki} = \begin{Bmatrix} D_{i1}^{(k)} - z_{k+1}A_{i1}^{(k)} \\ D_{i2}^{(k)} - z_{k+1}A_{i2}^{(k)} \\ D_{i6}^{(k)} - z_{k+1}A_{i6}^{(k)} \end{Bmatrix} \tag{5.37}$$

where $k = 1,2, \ldots , \mathrm{N}$ and $i = 1,2,6$. Equations (5.33-35) express the interlaminar stresses σ_z, σ_{zx}, and σ_{zy} ($p_2^{(k)}$, $t_2^{(k)}$, and $s_2^{(k)}$, respectively, in Figure 59) at the $k+1^{st}$ interface in terms of laminate membrane and bending resultants and their first and second derivatives, derivatives of the out-of-plane displacement w, and a number of coefficient vectors. These coefficients are easily found and depend on material properties, ply orientations, and the thickness coordinate of the interface of interest. The terms $t_1^{(1)}, s_1^{(1)}$, $p_1^{(1)}$, $t_{1,x}^{(1)}$, and $s_{1,y}^{(1)}$ are considered to be prescribed quantities on the bottom ($z = -\,t/2$) surface of the plate.

Equations (5.33-35) can be written in terms of mid-plane strains and curvatures by substituting equations (5.22) and (5.23) for the laminate resultants. The interlaminar stress equations would then require first and second derivatives of these mid-plane strains and curvatures. For von Karman plate theory, the relationships between the strains and displacements are

$$\varepsilon_1^{\mathrm{o}} = \varepsilon_x^{\mathrm{o}} = u_{,x} + \frac{1}{2}(w_{,x})^2, \qquad \varepsilon_2^{\mathrm{o}} = \varepsilon_y^{\mathrm{o}} = v_{,y} + \frac{1}{2}(w_{,y})^2$$

$$\varepsilon_6^{\mathrm{o}} = \gamma_{xy}^{\mathrm{o}} = (u_{,y} + v_{,x}) + w_{,x}w_{,y} \tag{5.38}$$

$$\kappa_1 = \kappa_x = -w_{,xx}, \qquad \kappa_2 = \kappa_y = -w_{,yy}, \qquad \kappa_6 = \kappa_{xy} = -w_{,xy}.$$

Thus, the interlaminar stress formulas could be written in terms of displacements u, v, and w instead of mid-plane strains and curvatures. Note that in this form, the interlaminar shear stresses depend upon second order derivatives of the in-plane displacements and on third order derivatives of the out-of-plane displacement, whereas the interlaminar normal stress component depends upon third order derivatives of the in-plane displacements and fourth order derivatives of the out-of-plane displacement. The interlaminar stress equations may be used in either the stress resultant (equations (5.33-35)), mid-plane strain and curvature, or displacement formulation; however, no matter which form is utilized, derivative information is required which is not directly obtainable from a two-dimensional finite element code such as STAGS. Thus, if these equations are to be used to derive interlaminar stress data from a STAGS solution, some numerical procedure is necessary to construct this derivative information from the STAGS output. The numerical method chosen in the current work is described in the next section.

The relative merits of the three different formulations for the interlaminar stress equations discussed above are not clear. It might at first seem best to obtain stress and moment resultants from the finite element solution and then apply some numerical procedure to that data to obtain first and second derivatives of the resultants, for use in equations (5.33-35), rather than to try to obtain third and fourth order derivatives of displacements for use in a displacement oriented formulation of the interlaminar stress equations. It should be remembered, however, that stress resultant output from a displacement-based finite element code is already the result of differentiation of the interpolation functions within an element, and as such may not provide very accurate data upon which to perform a second differentiation process. Better interlaminar stress results might in fact be obtained by starting with the very accurate displacement data from the finite element code over a field of elements, and then using some numerical procedure to extract the relatively high order displacement derivative information.

5.2 Construction of a Fourier Series Approximation for Discrete Data

In the preceding section, formulas for the interlaminar stresses were obtained from elasticity equilibrium equations, under the assumption that the thickness distribution of the in-plane stresses was piecewise linear in accordance with classical laminated plate theory. The interlaminar stress formulas show that higher order derivatives of the displacements are required than are necessary for a mathematically weak finite element formulation. Thus, higher order derivatives of the displacements as represented by the interpolation functions within an element cannot be expected to be very meaningful. The approach taken here is to construct a Fourier series approximation for each of the displacement components over the entire domain of the plate. The Fourier series coefficients are computed from nodal displacement data via the Discrete Fourier Transform (DFT). Derivatives of the displacements are computed by differentiating the Fourier series. This procedure to compute derivatives of displacements from discrete values of the displacement function was used in a tire contact problem by Tielking and Schapery[20].

Some researchers, for example Lajczok[21] and Chaudhuri[22], have had success in computing interlaminar shear stresses using equilibrium equations and linear distributions of the in-plane stresses in the thickness coordinate. Lajczok uses finite differences to compute first derivatives of in-plane strain data from the MSC/NASTRAN computer code, and then uses these derivatives to determine the interlaminar shear stresses. Chaudhuri calculates the transverse shear stresses, which are equal to interlaminar shear stresses at ply interfaces, for a triangular element after in-plane stresses have been computed from a layerwise constant shear angle theory. However, from the perspective of predicting delamination, interlaminar normal stress is just as important as the interlaminar shear stresses. The computation of interlaminar normal stress requires one more differentiation of the displacements than that necessary for calculation of the interlaminar shear stresses. Computation of the interlaminar normal stress from displacement-based finite element codes for laminated plates has not, to the author's knowledge, been reported in the open literature.

5.2.1 Derivation of the Method

Combined use of the Discrete Fourier Transform (DFT) and the Fourier series offers a way to obtain derivative information about a function which is known only as a set of discrete values. Consider an M x N matrix or grid of values, where M and N are even integers. This matrix could be a set of regularly spaced nodal quantities obtained from a finite element code. Application of the DFT to this matrix yields approximations to the first (M + 1) x (N + 1) coefficients of a truncated Fourier series representation of the original function. This approximate Fourier series may then be easily differentiated to provide the required derivative data.

For a function $w(x,y)$ which is periodic in x with period a and in y with period b, the Fourier series representation of $w(x,y)$ may be written in complex form as

$$w(x,y) = \sum_{m=-\infty}^{\infty} \sum_{n=-\infty}^{\infty} C(m,n) \exp\left[2\pi i \left(\frac{mx}{a} + \frac{ny}{b} \right) \right], \qquad i = \sqrt{-1} \tag{5.39}$$

where the coefficients $C(m,n)$ are determined from

$$C(m,n) = \frac{1}{ab} \int_0^a \int_0^b w(x,y) \exp\left[-2\pi i \left(\frac{mx}{a} + \frac{ny}{b} \right) \right] dx\, dy \qquad m, n = \dots, -1, 0, 1, \dots \ . \tag{5.40}$$

If the function $w(x,y)$ is explicitly known, the integration may be performed to obtain the Fourier series coefficients; if, however, $w(x,y)$ is known only at a set of discrete points, then equation (5.40) can no longer be used to find the Fourier series coefficients without resorting to numerical integration. Suppose, though, that we have such a function $w(x,y)$ which is known only at a set of points (x_j, y_k) , and that these points define a grid which is evenly spaced in the x- and y-directions, with M intervals in the x-direction and N intervals in y. M and N are even integers, and the spacing in the x-direction does not have to be the same as the spacing in y. The x and y values at which w is known are

$$x_j = j\frac{a}{\mathrm{M}} \qquad j = 0,1,2,\ldots,\mathrm{M}-1 \tag{5.41}$$

$$y_k = k\frac{b}{\mathrm{N}} \qquad k = 0,1,2,\ldots,\mathrm{N}-1\,. \tag{5.42}$$

The goal is to construct a truncated form of the Fourier series in equation (5.39)

$$w(x,y) \sim \sum_{m=-\mathrm{M}/2}^{\mathrm{M}/2} \sum_{n=-\mathrm{N}/2}^{\mathrm{N}/2} C(m,n) \exp\left[2\pi i\left(\frac{mx}{a} + \frac{ny}{b}\right)\right] \tag{5.43}$$

based on the data $w(x_j, y_k)$. Evaluating equation (5.39) at these points (x_j, y_k) gives

$$w(x_j, y_k) = w\left(j\frac{a}{\mathrm{M}}, k\frac{b}{\mathrm{N}}\right) = \sum_{m=-\infty}^{\infty} \sum_{n=-\infty}^{\infty} C(m,n) \exp\left[2\pi i\left(\frac{mj}{\mathrm{M}} + \frac{nk}{\mathrm{N}}\right)\right]. \tag{5.44}$$

The infinite sums may be restructured[23] so that

$$w(x_j, y_k) = \sum_{m=0}^{\mathrm{M}-1} \sum_{r=-\infty}^{\infty} \sum_{n=0}^{\mathrm{N}-1} \sum_{s=-\infty}^{\infty} C(m+\mathrm{M}r, n+\mathrm{N}s) \exp\left\{2\pi i\left[\frac{(m+\mathrm{M}r)j}{\mathrm{M}} + \frac{(n+\mathrm{N}s)k}{\mathrm{N}}\right]\right\} \tag{5.45}$$

which reduces to

$$w\left(j\frac{a}{\mathrm{M}}, k\frac{b}{\mathrm{N}}\right) = \sum_{m=0}^{\mathrm{M}-1} \sum_{n=0}^{\mathrm{N}-1} \left\{\sum_{r=-\infty}^{\infty} \sum_{s=-\infty}^{\infty} C(m+\mathrm{M}r, n+\mathrm{N}s)\right\} \exp\left[2\pi i\left(\frac{mj}{\mathrm{M}} + \frac{nk}{\mathrm{N}}\right)\right] \tag{5.46}$$

based on the periodicity of the exponential function. With the following definitions,

$$C_p(m,n) = \sum_{r=-\infty}^{\infty} \sum_{s=-\infty}^{\infty} C(m + \mathrm{M}r, n + \mathrm{N}s) \tag{5.47}$$

$$W_\mathrm{M} = e^{2\pi i/\mathrm{M}} \quad \text{and} \quad W_\mathrm{N} = e^{2\pi i/\mathrm{N}}, \tag{5.48}$$

where W_M and W_N are called weighting kernels, equation (5.46) may be rewritten

$$w\left(j\frac{a}{\mathrm{M}}, k\frac{b}{\mathrm{N}}\right) = \sum_{m=0}^{\mathrm{M}-1} \sum_{n=0}^{\mathrm{N}-1} C_p(m,n) W_\mathrm{M}^{mj} W_\mathrm{N}^{nk}. \tag{5.49}$$

Equation (5.49) defines the Inverse Discrete Fourier Transform (IDFT) in two dimensions for the Discrete Fourier Transform pair $w\left(j\frac{a}{\mathrm{M}}, k\frac{b}{\mathrm{N}}\right)$ and $C_p(m,n)$. The two-dimensional DFT for this pair is

$$C_p(m,n) = \frac{1}{\mathrm{MN}} \sum_{j=0}^{\mathrm{M}-1} \sum_{k=0}^{\mathrm{N}-1} w\left(j\frac{a}{\mathrm{M}}, k\frac{b}{\mathrm{N}}\right) W_\mathrm{M}^{-mj} W_\mathrm{N}^{-nk} \tag{5.50}$$

where $m = 0,1,\dots,\mathrm{M}-1$ and $n = 0,1,\dots,\mathrm{N}-1$. Standard Fast Fourier Transform (FFT) computer routines can be used to efficiently find the $C_p(m,n)$ given the data field $w(x_j, y_k)$ via equation (5.50).

The significance of the $C_p(m,n)$ terms will now be established. From equation (5.47), it may be observed that each $C_p(m,n)$ is equal to a double infinite sum of Fourier series coefficients. However, for large M and N and for values of the index m between $-\mathrm{M}/2$ and $\mathrm{M}/2$ and the index n between $-\mathrm{N}/2$ and $\mathrm{N}/2$, the dominant term in this double summation occurs when r and s are equal to zero. Therefore, if the terms in the summation corresponding to nonzero values of r and s are neglected, equation (5.47) becomes

$$C_p(m,n) \sim C(m,n)\,, \qquad \text{for} \quad m = -\frac{M}{2}, \ldots, \frac{M}{2} \quad \text{and} \quad n = -\frac{N}{2}, \ldots, \frac{N}{2}\,. \tag{5.51}$$

That is, the values of $C_p(m,n)$ obtained by applying the DFT to the data sequence $w(x_j, y_k)$ are approximations to the Fourier series coefficients $C(m,n)$ required in equations (5.39) and (5.43), if M and N are large even integers. Since, however, the values of $C_p(m,n)$ are found from equation (5.50) for $m = 0,1, \ldots, M-1$ and $n = 0,1, \ldots, N-1$ (i.e., the $C_p(m,n)$ are not initially determined for the negative values of the indices m and n in equation (5.51)), equation (5.51) should be rewritten

$$C(m,n) \sim C_p(m,n)\,, \qquad \text{for} \quad m = 0,1, \ldots, \frac{M}{2} \quad \text{and} \quad n = 0,1, \ldots, \frac{N}{2}\,. \tag{5.52}$$

The coefficients $C_p(m,n)$ for which $m = M/2+1, \ldots, M-1$ or $n = N/2+1, \ldots, N-1$ are, for the moment, ignored. For negative indices, it may be shown that due to the periodicity of the DFT in equation (5.50),

$$\begin{aligned} C_p(-m,n) &= C_p(M-m,n) \\ C_p(m,-n) &= C_p(m,N-n) \\ C_p(-m,-n) &= C_p(M-m,N-n) \end{aligned} \tag{5.53}$$

and therefore the coefficients corresponding to the negative values of m or n in equation (5.51) which are necessary for the Fourier series approximation in equation (5.43) are defined by

$$C(-m,n) \sim C_p(-m,n) = C_p(M-m,n)\,, \qquad m = 1, \ldots, \frac{M}{2} \quad \text{and} \quad n = 0,1, \ldots, \frac{N}{2} \tag{5.54}$$

$$C(m,-n) \sim C_p(m,-n) = C_p(m,N-n)\,, \qquad m = 0,1, \ldots, \frac{M}{2} \quad \text{and} \quad n = 1, \ldots, \frac{N}{2} \tag{5.55}$$

$$C(-m,-n) \sim C_p(-m,-n) = C_p(M-m,\, N-n)\,, \qquad m = 1, \ldots, \frac{M}{2} \quad \text{and} \quad n = 1, \ldots, \frac{N}{2}\,. \tag{5.56}$$

As shown by equations (5.54-56), the data values of $C_p(m,n)$ obtained from equation (5.50) for indices $m = \mathrm{M}/2 + 1, \ldots, \mathrm{M} - 1$ and/or $n = \mathrm{N}/2 + 1, \ldots, \mathrm{N} - 1$ are used to approximate the Fourier series coefficients with negative indices.

To summarize, for large even values of M and N, the coefficients $C(m,n)$ of equation (5.43), where $m = -\mathrm{M}/2, \ldots, \mathrm{M}/2$ and $n = -\mathrm{N}/2, \ldots, \mathrm{N}/2$, are approximated by equations (5.52) and (5.54-56), in which the $C_p(m,n)$ terms are found from the original discrete data field through the DFT in equation (5.50). With the determination of these coefficients, equation (5.43) gives an explicit, and differentiable, analytical representation of the original discrete data field. This process could be applied to the stress resultant and moment data and/or to the displacement data obtained from a STAGS solution. Derivatives of the Fourier series could then be used to approximate the higher derivatives of this data required by any of the formulations of the interlaminar stress equations derived in the last section.

5.2.2 Examples of the Method

5.2.2.1 One-Dimensional Example

A one-dimensional cylindrical bending problem was used for a simple first evaluation of the effectiveness of the Fourier analysis method. Consider a laminated plate of length a in the x-direction and of arbitrary width. A uniformly distributed compressive stress resultant N is applied at $x = 0$ and $x = a$, and a uniformly distributed pressure q is applied to the surface of the plate. The boundary conditions along the loaded edges of the plate are left, for the moment, unspecified, and the unloaded edges are free. The out-of-plane deflection of the plate, $w(x)$, may be written

$$w(x) = \mathrm{A}_1 \sin \lambda x + \mathrm{A}_2 \cos \lambda x + \mathrm{A}_3 x + \mathrm{A}_4 + \frac{q}{2N} x^2 \qquad (5.57)$$

where $\lambda^2 = N/D_{11}$, and A_1 through A_4 are constants determined from the boundary conditions on the loaded edges $x = 0$ and $x = a$. Once these boundary conditions are chosen, this problem has an analytical and easily differentiated solution, against which approximate solutions obtained from the combined DFT-Fourier series method may be compared. In addition, the expression in equation (5.57) may be substituted into the one-dimensional equivalent of (5.40) to yield exact Fourier series coefficients for comparison with the approximate coefficients from the DFT method. The cases of simply supported and clamped loaded edges were examined.

For a given set of boundary conditions, the exact solution (5.57) was sampled at M points x_j, where x_j is defined in equation (5.41), to provide the discrete data field for input to the DFT. A number of different values of M were tried, to assess the effects of changes in the sampling rate on the approximate Fourier solution. As was expected, sampling the original function at more points led to a more accurate Fourier series representation. Application of the one-dimensional DFT to the set of discrete data $w(x_j)$, $j = 0, 1, \ldots, M - 1$ provided $M + 1$ approximate Fourier series coefficients for use in a truncated one-dimensional Fourier series similar to equation (5.43). The values of $w(x)$ and its first four derivatives obtained from equation (5.57) and from the approximate truncated Fourier series were then compared at the M sampled points x_j. Since exact Fourier series coefficients could be derived from integration of equation (5.57), a truncated Fourier series representation of $w(x)$ using the first $M + 1$ exact coefficients was also included in the comparison. Direct comparison of the Fourier series coefficients $C_p(m)$ obtained from the DFT with the exact coefficients $C(m)$, where $m = -M/2, \ldots, M/2$, showed that for the dominant coefficients (corresponding to the smaller values of $|m|$), the exact and approximate values were identical. For larger values of $|m|$, a discrepancy between $C_p(m)$ and $C(m)$ appeared. As the number of sampled points M was increased, the range of values of the index m within which approximate Fourier series coefficients were equal to the exact coefficients grew. Interestingly, the approximate truncated Fourier series and its derivatives compared better in general to the exact solution than did the truncated Fourier series which used the exact Fourier coefficients.

Two problems with the DFT-Fourier series method became evident from examination of the one-dimensional example problem. The first problem is a common difficulty when the partial sum of a Fourier series "overshoots," or "rings," badly near a discontinuity. This is called the Gibbs phenomenon, and results from nonuniform convergence of the Fourier series near the discontinuity. In order to understand this problem, it is necessary to look more closely at the nature of the Fourier series representation of a function that is not periodic. The original function of interest often applies to a finite region; for example, the cylindrical bending problem of this section has physical meaning only in the range $0 \leq x \leq a$. The Fourier series, however, is periodic and ranges over all possible values of the independent variables. The Fourier series representation of a function, in fact, represents what is called the protracted version of the original function. The protracted function may be visualized as an infinite sequence of exact copies of the original function placed one after the other, forming a periodic function which can then be represented as a Fourier series. The protracted functions corresponding to the out-of-plane displacement for the simply supported and clamped end condition cases of the cylindrical bending problem are shown in Figure 60. If a discontinuity exists at any point in the protracted function or its derivatives, a "ringing" or oscillation about the point of discontinuity will occur in the corresponding derivative of the truncated Fourier series approximation, due to the missing terms of the series. The ringing propagates away from the points of discontinuity and into the entire domain of the Fourier series approximation for derivatives of higher order than the one in which the discontinuity appears. For example, note that in Figure 60(a), while no discontinuity occurs in the displacement function for the simply supported case, there is a slope (first derivative) discontinuity at points $x = \ldots, -a, 0, a, \ldots$. In the neighborhood of these points, the value of the first derivative obtained from a truncated Fourier series representation would oscillate about the exact value. For higher order derivatives, the ringing would spread throughout the entire domain of the truncated Fourier series approximation. From Figure 60(b), it may be observed that the protracted function for the case of clamped boundary conditions is apparently continuous at least through the second derivative. Ringing in fact did not occur in the truncated Fourier series approximation for the clamped cylindrical bending case until the third derivative, and thus the comparison between equation (5.57) and its derivatives and the truncated

Fourier series approximation was much better in general for clamped boundary conditions than for simply supported ends.

Since partial sums of the Fourier series will oscillate about the exact function values near discontinuities, a smoothing technique is often useful in countering the ringing effects. The smoothing algorithm used during the study of the one-dimensional example of this section is known as smoothing by fives. If smoothing of a certain derivative of the truncated Fourier series approximation was desired, then the value of that derivative at each interior point $x_j, j = 2, \dots, \mathrm{M} - 3$, was replaced by the arithmetic mean of the original values at x_{j-2}, x_{j-1}, x_j, x_{j+1}, and x_{j+2}. The value of the derivative of interest at the endpoint x_0 was replaced by the average of the original values at x_0, x_1, and x_2 , while the smoothed value at endpoint $x_{\mathrm{M}-1}$ was defined to be the average of the original values at $x_{\mathrm{M}-3}$, $x_{\mathrm{M}-2}$, and $x_{\mathrm{M}-1}$. At point x_1 , the original value of the derivative was replaced by the mean of itself, the original value at endpoint x_0, and the original values at the two nearest interior points, x_2 and x_3 . A similar process was used to obtain the smoothed value for $x = x_{\mathrm{M}-2}$. This smoothing technique was found to significantly diminish the effects of the Gibbs phenomenon in the one-dimensional cylindrical bending case.

The second problem which was addressed during the examination of this one-dimensional example arises from the fact that the Discrete Fourier Transform requires evenly spaced input data; that is, for an N-dimensional problem, the data sampling rate in each coordinate direction must remain constant. However, the discrete data field corresponding to a finite element solution for displacements, strains, or stress resultants is often not evenly spaced, due to mesh refinements in certain areas of the finite element model. The strategy proposed to address this problem was to perform interpolation of the data between the finite element data points, and then sample this interpolated data at a constant rate to generate input for the DFT. For the one-dimensional cylindrical bending example, this situation was simulated by evaluating the exact displacement function of equation (5.57) at unevenly spaced values of x . The set of exact values of w so obtained represented the unevenly spaced output from a finite element program. Piecewise cubic spline interpolating polynomials were constructed between these points, and then this series of cubic splines was sam-

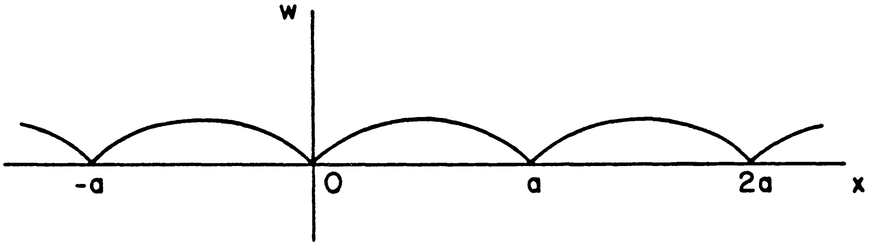

a) Simple Support

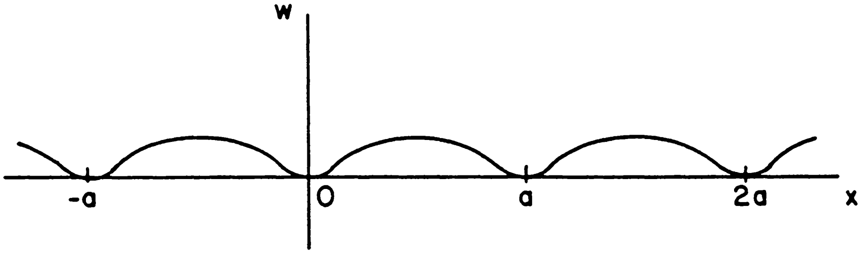

b) Clamped

Figure 60. Protracted functions for the cylindrical bending example: (a) simply supported boundary conditions and (b) clamped boundary conditions

pled at a constant rate to provide the discrete displacement input to the DFT. A truncated Fourier series approximation to the original unevenly spaced data could then be formed and compared to the exact function of equation (5.57) and its derivatives. It was found that the introduction of this extra interpolation step slightly degraded the results obtained from the approximate Fourier series method. It was also found, by keeping the number and spacing of the original interpolated points the same while varying the sampling rate imposed over these interpolated points to obtain the DFT input data, that the best results were obtained from the Fourier series approximation when the sampling rate was such that no more than one point was sampled from the interior of the smallest original interval. In retrospect, this result is not surprising, since such a sampling rate allows the required uniformly spaced input data to be generated while minimizing the possibly erroneous contributions of the cubic spline interpolation step.

Results are presented in Figures 61 through 64 for the cylindrical bending problem with clamped end conditions. The hypothetical plate had the L16A layup from the current study and length $a = 5.0$ in; the compressive stress resultant N was 100.0 lb/in and the uniform lateral pressure q was -1.0 psi. Twenty-one unevenly spaced points were obtained from the exact function for $w(x)$ and connected by piecewise cubic splines, which were then sampled to produce 52 evenly spaced values of w for input to the DFT. The solid line in each figure represents the exact function or derivative, the open triangles are the values obtained at the 52 sampling points from the truncated Fourier series approximation, and the dashed line connects the points obtained by applying the smoothing-by-fives algorithm to the approximate Fourier series results. The plots for w and w'' in Figures 61 and 62 show that the Fourier series results are excellent without smoothing for cases where no discontinuities are present. A discontinuity occurs at the end points $x = 0, a$ of the third derivative of the exact function in Figure 63, which causes ringing throughout the domain of the truncated Fourier series approximation; but the smoothing algorithm produces results very near the exact values, especially towards the interior of the region. Examination of the results for w'''' in Figure 64 shows that although no discontinuity exists in the protracted function for the fourth derivative, sizable oscillations occur in the truncated Fourier series solution. This ringing is a result of the third derivative discontinuity; but it is once again considerably diminished by the application of smoothing.

5.2.2.2 *Two-Dimensional Example*

Several two-dimensional problems were also examined. As in the one-dimensional case, each example was an attempt to learn more about the behavior of the approximate Fourier method by using it to reconstruct from discrete data a function w which was originally written in an analytically exact and differentiable form. The most sophisticated example studied the ability of the combined DFT-Fourier series approach to reconstruct a displacement function $w(x,y)$ which was similar in appearance to the out-of-plane deflection of a one-edge-free plate. Consider a two-dimensional region of length a in the x-direction and width b in the y-direction. Let a function of the form

$$w(x,y) = \left(c_1x^4 + c_2x^3 + c_3x^2 + c_4x + c_5\right)\left(d_1y^4 + d_2y^3 + d_3y^2 + d_4y + d_5\right) \tag{5.58}$$

exist in the region. It should be noted that this function has no physical significance; this is not intended to be the solution to a plate bending problem. Impose clamped-like boundary conditions (out-of-plane displacement and rotation set equal to zero) along the edges $x = 0$, $x = a$, and $y = 0$ of the region. Along $y = b$, let $w_{,y}$ and $w_{,yy}$ be equal to zero. It must be pointed out that these boundary conditions on $y = b$ are not those associated with a free edge in plate theory. Application of these eight boundary conditions to equation (5.58) yields

$$w(x,y) = c_1d_1\left(x^4 - 2ax^3 + a^2x^2\right)\left(y^4 - \frac{8}{3}by^3 + 2b^2y^2\right) \tag{5.59}$$

where the product c_1d_1 is a constant which may be arbitrarily chosen. A value for c_1d_1 of $48/a^4b^4$, which gives a maximum displacement w of 1.0 at the center $x = a/2$ of the "free edge" $y = b$, was used in the current work. Equation (5.59) with this value of c_1d_1 is depicted graphically in Figure 65.

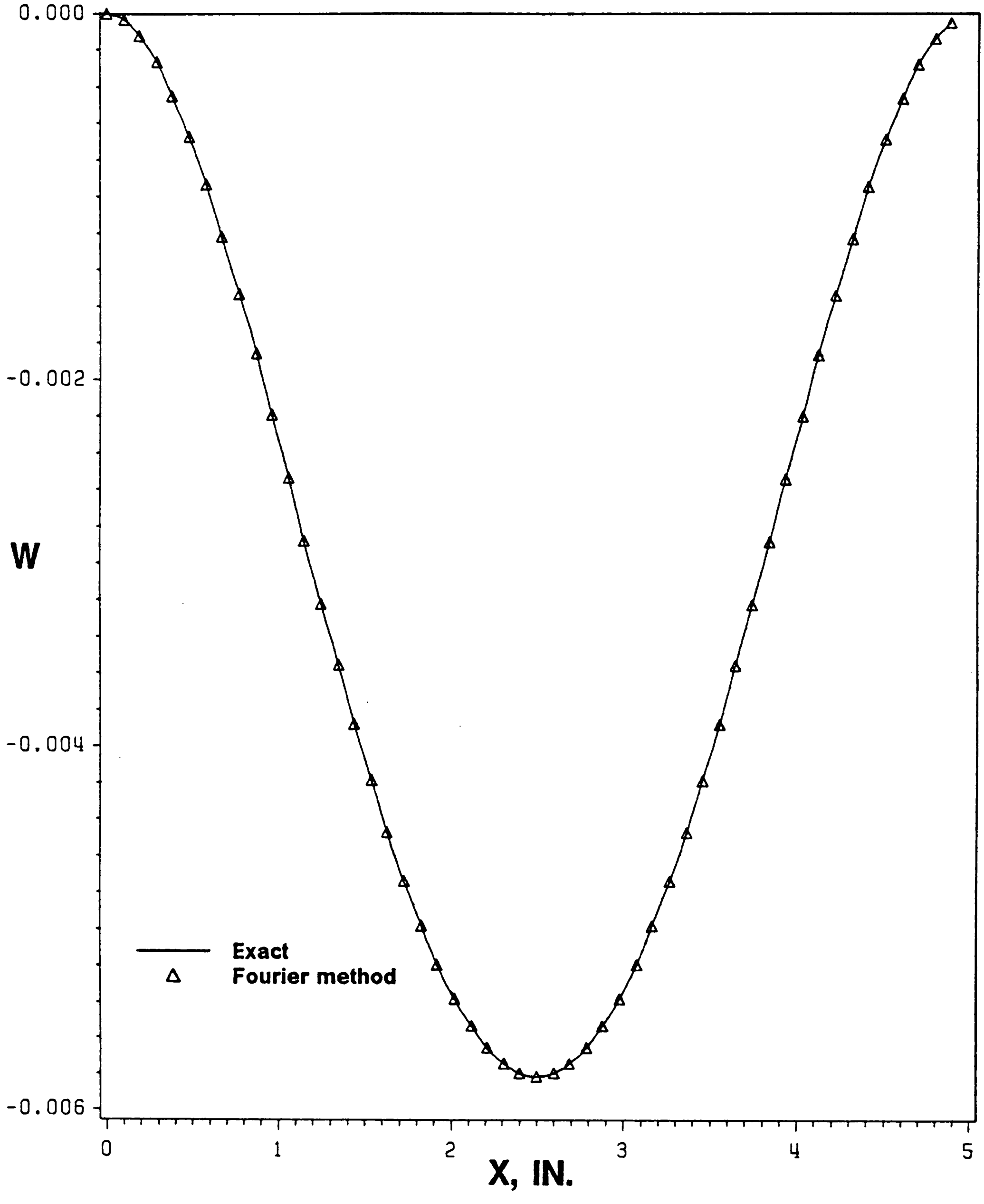

Figure 61. Displacement w for 1-D cylindrical bending example

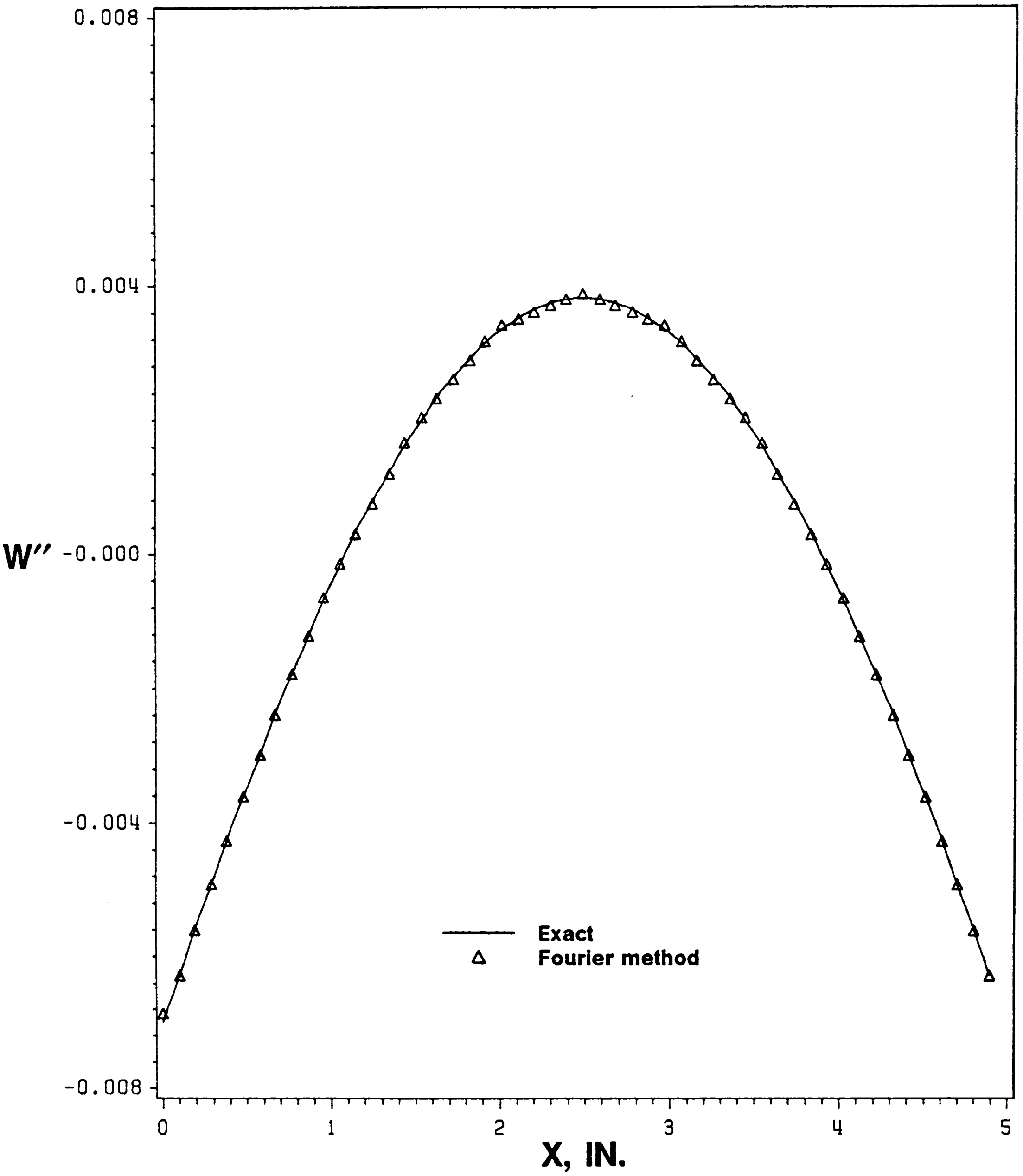

Figure 62. Second derivative of w for 1-D cylindrical bending example

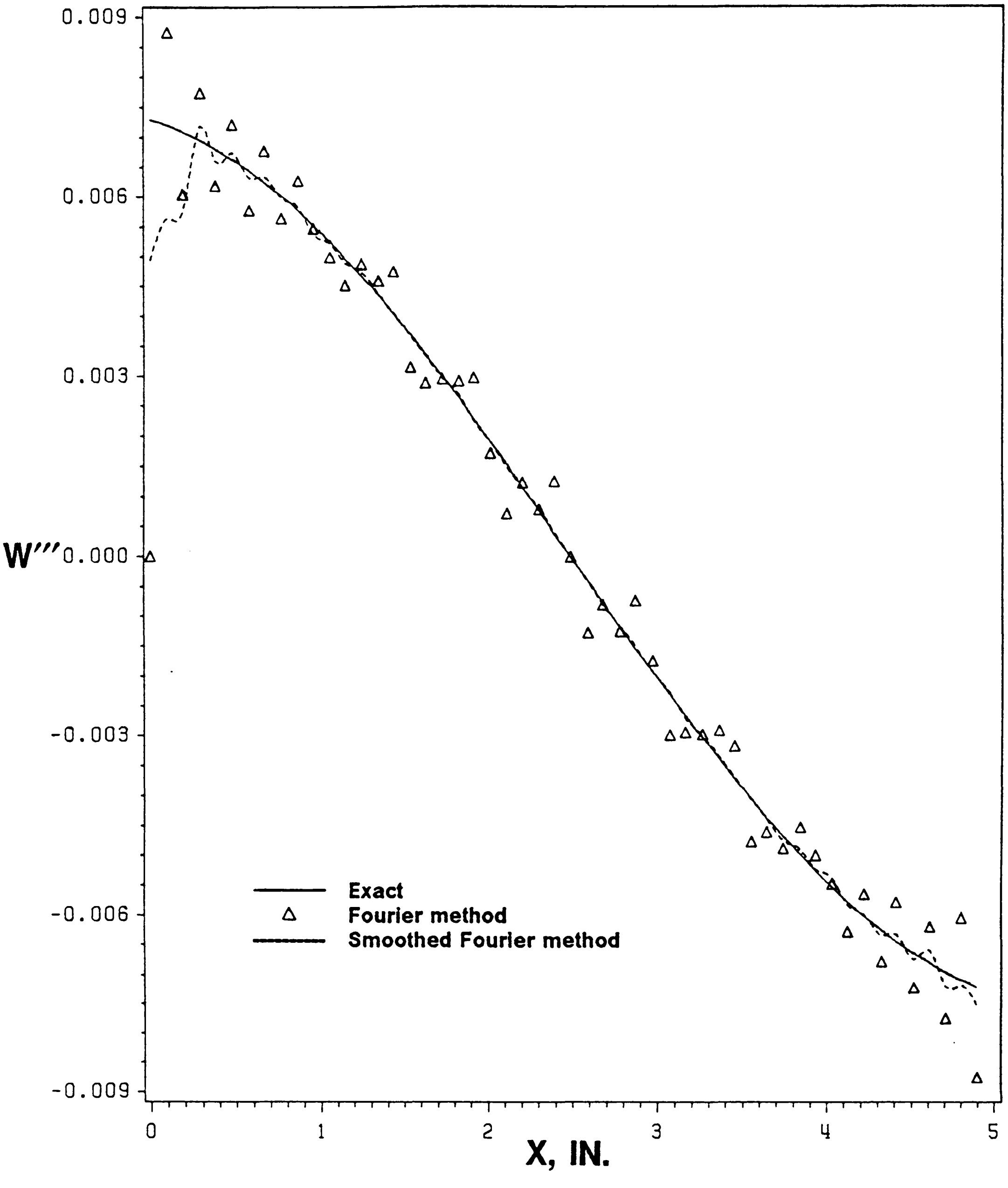

Figure 63. Third derivative of w for 1-D cylindrical bending example

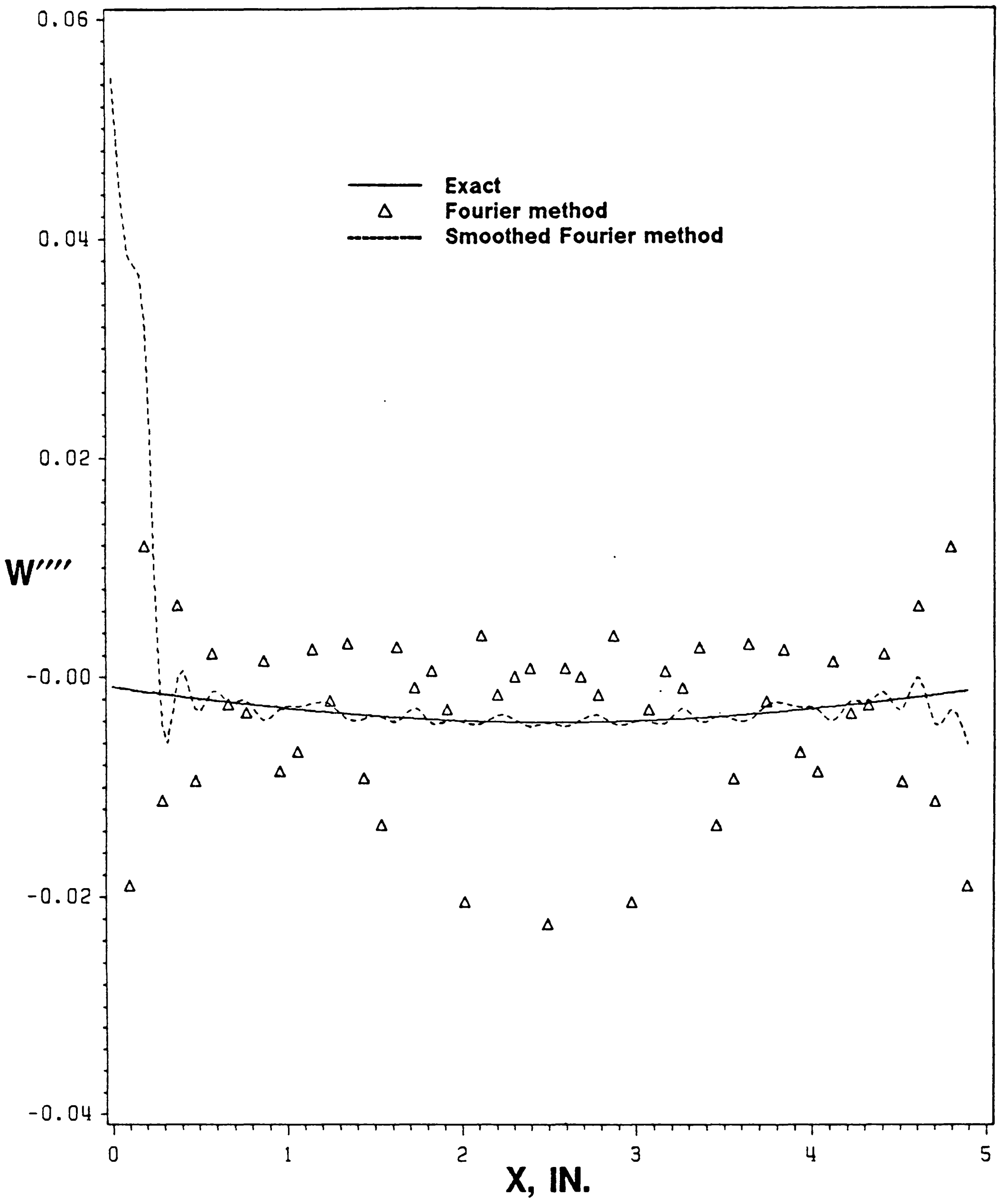

Figure 64. Fourth derivative of w for 1-D cylindrical bending example

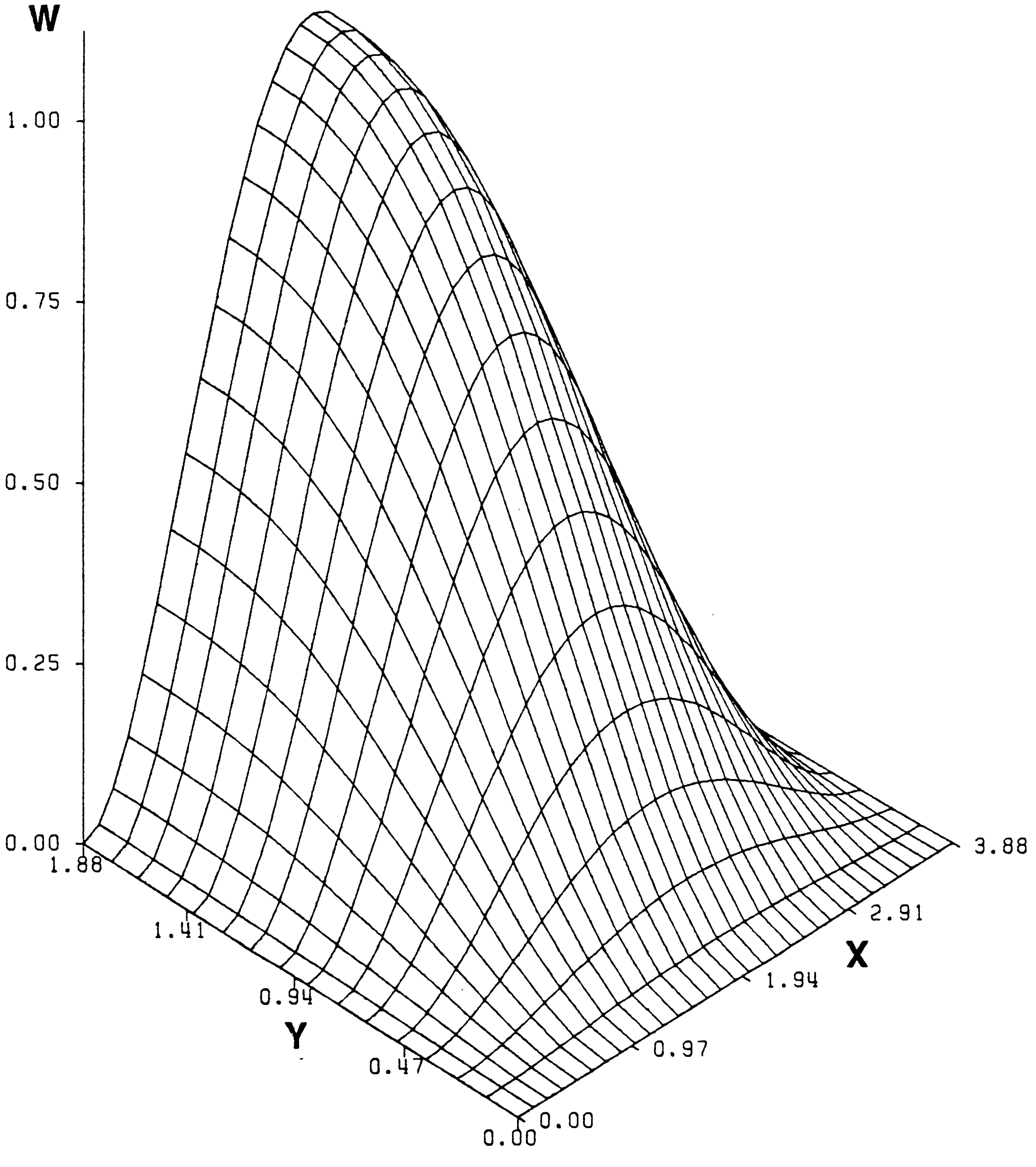

Figure 65. Displacement function for the two-dimensional free edge example

Equation (5.59) was used both as a source for deriving input data fields for the two-dimensional approximate Fourier method and as a basis for comparison and evaluation of the performance of this Fourier method, just as equation (5.57) was used in the one-dimensional cylindrical bending example. It was recognized that the same two problems observed in the one-dimensional case, the Gibbs phenomenon due to discontinuities in the original protracted function and the acquisition of evenly spaced input to the DFT from potentially unevenly spaced displacement data, would have to be addressed. Extension of the smoothing technique used for the cylindrical bending case to two dimensions proved to be fairly effective against the Gibbs phenomenon. An unfortunate consequence of this two-dimensional "free edge" problem, however, is a very large discontinuity in the protracted displacement function in the y-direction, as may be observed from Figure 65. This discontinuity in such a low order derivative causes high order derivative results from the truncated Fourier series to behave badly, even with smoothing applied. This problem is very serious, since in the current stiffener crippling work interlaminar stress data (and thus high order derivative data) are desired for just such a one-edge-free type of case (a postbuckled flange).

The free edge displacement discontinuity problem was ameliorated by performing what will be referred to herein as a "free edge reflection." The discrete data field which was sampled from equation (5.59) was reflected about the line $y = b$ (the "free edge") to form a new discrete data set whose domain was $0 \leq x \leq a$, $0 \leq y \leq 2b$, and which was effectively "clamped" on all four edges. In other words, a mirror image of the original discrete displacement information was constructed in the region $0 \leq x \leq a$, $b \leq y \leq 2b$. The protracted version of this new function had no displacement discontinuities, and the original discrete function sampled from equation (5.59) remained present within the new function in the sub-region $0 \leq x \leq a$, $0 \leq y \leq b$. Application of the two-dimensional DFT to this reflected discrete data field yielded approximate coefficients for a truncated Fourier series which had period a in the x-direction and $2b$ in the y-direction, and which was a representation of the discrete data field that resulted from the reflection. This truncated Fourier series approximation was then evaluated over the original domain $0 \leq x \leq a$ and $0 \leq y \leq b$ to obtain displacement and derivative information for the original region of interest. This procedure was somewhat effective in reducing the magnitude of the Gibbs phenomenon observed in this quasi-free edge example. Even with the use of this reflection technique and a smoothing process, however, the effects of the Gibbs phenomenon remained unacceptably large in the higher order derivatives. Thus, it appears from this example that the combined DFT-Fourier series method as formulated in the current work is not completely successful in generating accurate high order derivative information from discrete input data for the case of a one-edge-free problem. It is possible that a recasting of the method based on a series made up of Chebyshev polynomials instead of the trigonometric functions of the Fourier series would provide better results for the case of a free edge.

The second difficulty, the acquisition of evenly spaced two-dimensional input to the DFT from potentially unevenly spaced finite element solution data, was addressed through interpolation of the original discrete data, similar to the one-dimensional case. In anticipation of the eventual use of the DFT-Fourier series method to reconstruct derivative information from actual STAGS solution data, however, a more useful interpolation scheme than the cubic splines of the cylindrical bending example was utilized. Since, as discussed in Section 4.2, the finite element used in the analytical portion of the current work was the STAGS 411 element, which has twelve out-of-plane degrees of freedom, interpolation among the original discrete data points of the free edge example problem was accomplished with the interpolation polynomial for a four-noded, twelve out-of-plane degree-of-freedom rectangular plate finite element taken from Ref. 24. This polynomial was used to interpolate within the rectangular regions formed by the original data, where the four corners of each region were defined by four adjacent discrete data points. Evenly spaced sampling of the original data could thus be achieved, providing the M × N input matrix to the DFT for calculation of the approximate Fourier series coefficients, as per equation (5.50).

Results are presented for the "free edge" problem of equation (5.59), with $a = 4$ and $b = 2$, in Figure 66 for $w_{,xxxx}$ and in Figure 67 for $w_{,yyyy}$. The input data for the DFT was obtained by directly sampling equation (5.59) at the points (x_j, y_k) defined in equations (5.41) and (5.42) with $\mathrm{M} = 32$ and $\mathrm{N} = 16$. Free edge reflection was performed during the computations, but only the data corresponding to the original region is shown in the figures. In both figures, the exact solution from equation (5.59) is labeled (a), the data obtained from the truncated approximate Fourier series is plotted in (b), and smoothed Fourier series results are shown in (c). For both $w_{,xxxx}$ and $w_{,yyyy}$, the unsmoothed results of the approximate Fourier series show considerable evidence of the Gibbs phenomenon in the direction in which the four derivatives are taken; smoothing diminishes these effects. Mixed fourth order partial derivatives like $w_{,xxyy}$ and lower order partial derivatives of w exhibit less ringing effects and better overall correlation between the exact solution and the truncated approximate Fourier series reconstruction than do the derivatives depicted in Figures 66 and 67.

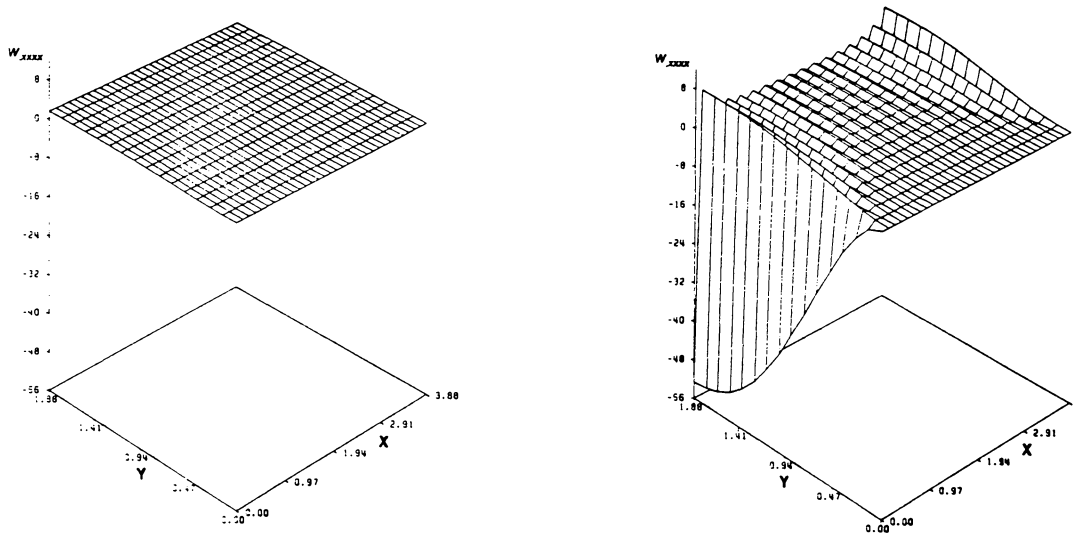

(a) Exact

(b) Fourier method

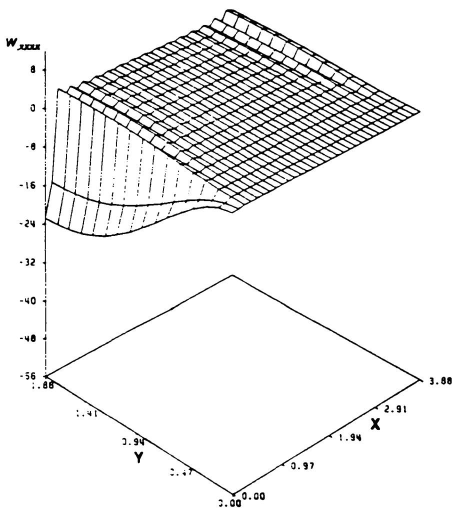

(c) Smoothed Fourier method

Figure 66. W,xxxx for the two-dimensional free edge example: (a) exact function , (b) approximate Fourier series , and (c) smoothed approximate Fourier series

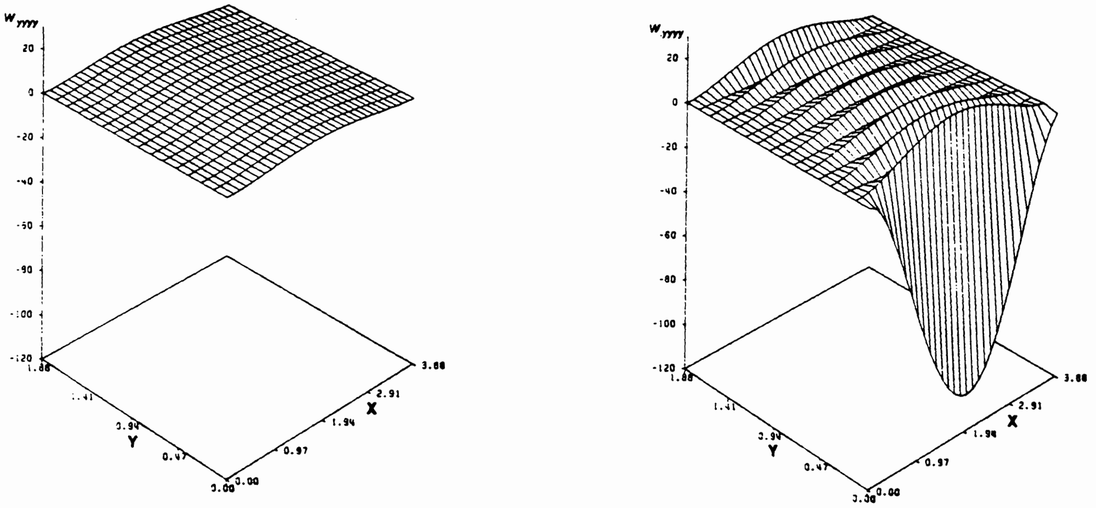

(a) Exact

(b) Fourier method

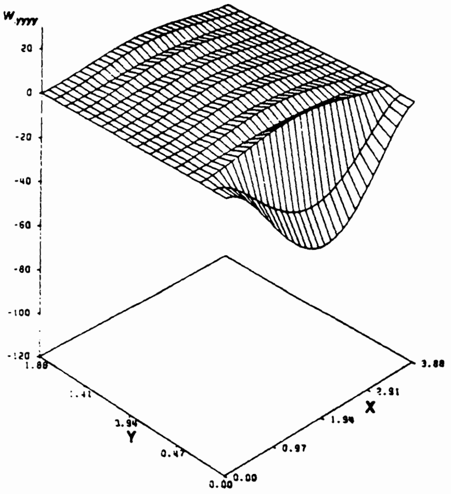

(c) Smoothed Fourier method

Figure 67. W,yyyy for the two-dimensional free edge example: (a) exact function , (b) approximate Fourier series , and (c) smoothed approximate Fourier series

Chapter 6

Summary and Conclusions

The preceding chapters have detailed the results of a combined experimental and analytical study of the local buckling, postbuckling, and crippling (failure) of a variety of thin-walled graphite-epoxy aircraft stiffener sections subjected to axial compressive loading. The goal of this work has been to enhance the current understanding of composite stiffener crippling by

1. conducting fundamental experiments to determine how composite stiffener crippling differs from metallic stiffener crippling,

2. studying the influence of cross section, layup, flange width, wall thickness, inner corner radius, and stiffener length on the buckling, postbuckling, and crippling behavior of graphite-epoxy stiffeners,

3. using the general purpose shell analysis computer code STAGS to create computational models for the buckling and postbuckling response of selected test specimens which correlate fairly well with experimental results, and

4. developing a postprocessor to the STAGS code which can estimate interlaminar stresses.

A summary of the important results and conclusions of the current study is presented here, followed by suggestions for future work in the area of composite stiffener crippling.

6.1 Experimental Program

A total of 36 stiffener specimens fabricated from three different layups of AS4/3502 graphite-epoxy unidirectional tape were tested as intermediate length columns loaded in axial compression. Channel, zee, and I- and J-section cross-sectional geometries were considered; the flange width b_f, inner corner radius r_c, thickness t, and gage length l were varied among the specimens to examine the effects of these basic geometric parameters upon stiffener response. An additional quantity, the flange width-to-thickness ratio $(b/t)_f$, was defined in equation (3.4), and combines b_f, r_c, and t into one useful dimensionless parameter. The quantity $(b/t)_f$ is basically the ratio of the width to the thickness of that portion of a flange which can be considered a flat plate. The experimental data from each individual test was closely examined in order to identify damage events which might have occurred during the test and then estimate the location and nature of damage initiation. The following conclusions may be drawn from the experimental program:

1. While the crippling of metallic thin-walled stiffener sections is a local collapse initiated by yielding in the corners due to high compressive membrane strains, composite stiffener crippling is characterized by the existence of several potential brittle failure mechanisms. Depending on the geometry, material properties, and layup of a composite stiffener, crippling failure can be initiated by delamination at the free edge of a flange, delamination in the interior of a coplanar pair of flanges at the web junction, delamination in a corner due to an opening of the angle

between cross-sectional elements, or an ultimate compressive strength material failure in a corner.

2. A number of different damage initiation modes have been observed for the I- and J-section specimens in this study. All of these modes may be placed into two categories: damage which initiates in a corner due to material compressive strength failure, or damage which begins as a delamination somewhere in the specimen. The observation that the first damage found in a specimen occurs in a certain mode does not necessarily imply that the ultimate failure of the specimen is due to the same mechanism.

3. For the I- and J-section stiffeners, a relationship exists between the damage initiation mode observed and the width-to-thickness ratios of a specimen's flanges. If any flange in a specimen cross section has $10 < (b/t)_f < 20$, then damage initiation due to delamination at the free edge of that flange is the most likely mode. If $(b/t)_f$ is greater than about 25 for all flanges, then the effects of transverse shearing deformations (and interlaminar stresses) in the flanges are diminished, and large compressive stresses in the corners result in a local material strength failure in a corner. For the I- and J-section specimens studied in the present work, failure occurs in a short column mode (i.e., buckling does not occur) if the $(b/t)_f$ of all flanges is less than ten.

4. For the sixteen-ply I- and J-section specimens in which the width-to-thickness ratios of all flanges are less than fifteen, a previously undocumented type of crippling failure is sometimes observed in which a single delamination involving only one ply interface propagates through the entire width of two coplanar flanges and along almost the full length of the specimen. No broken fibers accompany this failure mode. The mode appears most dramatically in I-section specimens having the L16B layup. Undetected manufacturing defects within the specimen may be responsible for this type of crippling failure.

5. Decreasing the average flange width-to-thickness ratio has the general effect of increasing the average stress in a specimen at buckling for all four stiffener cross-sectional shapes considered.

This increase in the average stress is not just the effect of a reduction in the area of the cross section; decreasing the $(b/t)_f$ of a flange by reducing the flange width b_f causes an increase in the buckling load as well as the buckling stress.

6. For the I- and J-section specimens, an increase in the inner corner radius from 0.125 inches to 0.250 inches implies a greater amount of unidirectional filler material in the filled corner regions, which significantly increases both the average buckling and average crippling stresses in the stiffener. The same increase in the corner radius for the channel and zee section stiffeners does not significantly change the average buckling stress or crippling stress. Since the corners of a zee or channel cross section are formed by the junction of only two elements (a flange and the web), the insertion of filler material in these corners during fabrication is not necessary.

7. The presence of non-symmetric stacking sequences in some cross-sectional elements of the I- and J-section specimens as a result of the fabrication process does not seem to cause any significant effects. Apparently, as was noted by Wang[12], the mutual restraint of the individual plate elements in each cross section inhibits any prebuckling out-of-plane deformation of these elements due to a non-symmetric layup.

From these conclusions, certain design recommendations may be made for composite I- and J-section stiffeners subjected to axial compression.

1. For a postbuckled design, that is, a structural design in which the stiffeners are allowed to operate in a buckled condition, the strongest stiffener cross section (i.e., the cross section with the highest crippling load) will have large flange width-to-thickness ratios and inner corner radii. The large $(b/t)_f$ means that the stiffener will buckle at a relatively low stress level, but the flanges will be resistant to free edge delamination. This allows the corners of the stiffener to achieve their full load-carrying potential before failure occurs. The large inner corner radius and consequent increased volume of 0° corner filler material enhance this corner load-carrying capability.

2. If local buckling of the stiffeners is unacceptable, then a buckling resistant design is required. Decreasing the width-to-thickness ratio of the flanges will increase the average stress at which buckling occurs in a stiffener.

6.2 Analytical Program

The finite element computer code STAGS was used to analyze the geometrically nonlinear response of five experimental specimens: Z1, Z6, I2, I10, and I16. This code is based on two-dimensional shell theory consistent with the Kirchhoff hypothesis, and it therefore neglects through-the-thickness extension and transverse shearing deformations. For the stiffener specimens under consideration in the current study, however, which have relatively small flange width-to-thickness ratios, and which show significant delaminations after failure, transverse shearing deformations are not always negligible. This limitation of the STAGS code was exhibited in the comparison of experimental and analytical results for the three specimens (Z6, I2, and I16) discussed in Chapter 4. These results were compared on a global basis by examining load-shortening data, and on a local basis by looking at cross-sectional distributions of surface strains. In addition, a variety of plane stress failure criteria were applied to in-plane stress data obtained from STAGS at selected locations within each specimen for the five specimens for which a nonlinear analysis had been completed. The criteria were evaluated at the load corresponding to the first observed experimental damage event for specimens Z1, I2, I10, and I16, and at the crippling load for specimen Z6. Finally, a postprocessor to determine interlaminar shear and normal stresses from STAGS nodal solution data using equations derived from equilibrium and an assumed piecewise linear thickness distribution of in-plane stresses was partially developed. The postprocessor utilizes a combined Discrete Fourier Transform - Fourier series method to generate the high order derivative information necessary for such interlaminar stress computations from the STAGS displacement data. Several conclusions may be made from the results of the analytical portion of the present study.

1. Changing the initial geometric imperfection applied to the STAGS nonlinear model of a stiffener specimen changes the buckling load with respect to the bifurcation buckling load. As the analysis continues into the postbuckling region, the effects of such an imperfection variation disappear.

2. Correlation between STAGS analysis and experiment is excellent prior to buckling for all specimens analyzed on both the load-shortening curves and surface strain distributions.

3. Correlation between STAGS analysis and experiment degrades after buckling has occurred. One reason for this lack of correlation is the neglect of transverse shear by STAGS, which causes the finite element models to appear "stiffer" in postbuckling than the corresponding physical specimens. Another possible explanation for this lack of agreement is the uncertainty of the boundary conditions at the ends of the gage length of each specimen analyzed. A discrepancy in the in-plane boundary conditions may have significant effects on the postbuckling response. Damage events which occur during the testing of the specimens also contribute to this observed lack of agreement.

4. Specimen I2 shows the best correlation between analysis and experiment in postbuckling of all specimens analyzed. Since the flanges of this specimen have relatively large width-to-thickness ratios $(b/t)_f$, which implies that the effects of through-the-thickness shear are diminished, the improved agreement for this specimen further supports the idea that neglect of transverse shearing deformations by STAGS is responsible for some of the lack of agreement noted between experiment and analysis for all specimens analyzed.

5. The plane stress failure analysis is not able to predict consistently the load or mode of the first damage event for specimens Z1, I2, I10, and I16 or the crippling load of specimen Z6. It does, however, seem to indicate the same locations of damage initiation as were observed from the testing of specimens Z1, I2, I10, and I16. The plane stress compressive fiber mode criterion of Hashin appears to correlate best with the experimental results among those failure criteria

surveyed; the Tsai-Hill failure criterion gives, for the specimens of the present study, the most conservative predictions.

6. The use of the Discrete Fourier Transform in combination with a truncated Fourier series to construct high order displacement derivatives from discrete displacement data yields good results in some cases. However, for the very important problem of a plate free edge, this method does not provide sufficiently accurate high order derivative information, due to the strength and pervasiveness of the Gibbs phenomenon. The use of Chebyshev polynomials in the place of the trigonometric functions of the Fourier series might improve this method.

6.3 Suggestions for Future Work

1. A significant body of experimental research on composite stiffener crippling has been established, due to the present study and the previous work of Refs. 1-5 and 8-12 detailed in Chapter 1. Additional experimental work, however, involving a wide variety of cross-sectional geometries, flange widths, web widths, and inner corner radii would help to refine the preliminary observations made in the current study on the relationships between geometric parameters and crippling failure.

2. While some useful two-dimensional postbuckling analysis of composite stiffeners has been performed, this study and others have shown that there is a need for analysis which includes the effects of transverse shearing deformations and interlaminar stresses in some way. Such an analysis, which might use the method described in Chapter 5, would provide important information on the internal states of stress and strain within a stiffener specimen, and thus complement the observations which have been made from experiments.

3. A more thorough examination of the capabilities of the interlaminar stress postprocessor discussed in Chapter 5 is necessary, including an evaluation of the performance of an analog of the DFT-Fourier series method based on a series of Chebyshev polynomials.

References

1. Spier, E. E., "Crippling/Column Buckling Analysis and Test of Graphite/Epoxy Stiffened Panels," AIAA Paper No. 75-753, presented at the *AIAA/ASME/SAE 16th Structures, Structural Dynamics, and Materials Conference*, Denver, CO, May 27-29, 1975.

2. Spier, E. E. and Klouman, F. L., "Empirical Crippling Analysis of Graphite/Epoxy Laminated Plates," *Composite Materials: Testing and Design* (Fourth Conference), ASTM STP 617, 1977, pp. 255-271.

3. Spier, E. E., "Stability of Graphite/Epoxy Structures with Arbitrary Symmetrical Laminates," *Experimental Mechanics*, Vol. 18, No. 11, Nov. 1978, pp. 401-408.

4. Spier, E. E., "On Experimental Versus Theoretical Incipient Buckling of Narrow Graphite/Epoxy Plates in Compression," AIAA Paper No. 80-0686, in *Proceedings of AIAA/ASME/ASCE/AHS 21st Structures, Structural Dynamics, and Materials Conference*, May 12-14, 1980, pp. 187-193.

5. Spier, E. E., "Postbuckling Fatigue Behavior of Graphite-Epoxy Stiffeners," AIAA Paper No. 82-0779, in *Proceedings of AIAA/ASME/ASCE/AHS 23rd Structures, Structural Dynamics, and Materials Conference*, Part 1, May 10-12, 1982, New Orleans, LA, pp. 511-527.

6. Peery, D. J., *Aircraft Structures*, McGraw-Hill Book Company, New York, 1950, pp. 382-384.

7. Arnold, R. R., "Buckling, Postbuckling, and Crippling of Materially Nonlinear Laminated Composite Plates," Ph.D. Dissertation, Department of Civil Engineering, Stanford University, March 1983.

8. Tyahla, S. T. and Johnson, E. R., "Failure and Crippling of Graphite-Epoxy Stiffeners Loaded in Compression," Report No. CCMS-84-07 and VPI-E-84-19, Virginia Polytechnic Institute and State University, Blacksburg, VA, June 1984.

9. Reddy, A. D., Rehfield, L. W., Bruttomesso, R. I., and Krebs, N. E., "Local Buckling and Crippling of Thin-Walled Composite Structures Under Axial Compression," AIAA Paper No. 85-0672, in *Proceedings of AIAA/ASME/ASCE/AHS 26th Structures, Struc-*

tural Dynamics, and Materials Conference, Part 1, April 15-17, 1985, Orlando, FL, pp. 804-810.

10. Rehfield, L. W. and Reddy, A. D., "Observations on Compressive Local Buckling, Postbuckling, and Crippling of Graphite/Epoxy Airframe Structure," AIAA Paper No. 86-0923, in *Proceedings of AIAA/ASME/ASCE/AHS 27th Structures, Structural Dynamics, and Materials Conference*, Part 1, May 19-21, 1986, San Antonio, TX, pp. 301-306.

11. Causbie, S. M. and Lagace, P. A., "Buckling and Final Failure of Graphite/PEEK Stiffener Sections," AIAA Paper No. 86-0921, in *Proceedings of AIAA/ASME/ASCE/AHS 27th Structures, Structural Dynamics, and Materials Conference*, Part 1, May 19-21, 1986, San Antonio, TX, pp. 280-287.

12. Wang, C., Pian, T. H. H., Dugundji, J., and Lagace, P. A., "Analytical and Experimental Studies on the Buckling of Laminated Thin-Walled Structures," AIAA Paper No. 87-0727, in *Proceedings of AIAA/ASME/ASCE/AHS 28th Structures, Structural Dynamics, and Materials Conference*, Part 1, April 6-8, 1987, Monterey, CA, pp. 135-140.

13. Almroth, B. O., Brogan, F. A., and Stanley, G. M., *Structural Analysis of General Shells*, Vols. 1 and 2, Applied Mechanics Laboratory, Lockheed Palo Alto Research Laboratory, Palo Alto, CA, Dec. 1982.

14. Whitney, J. M., *Structural Analysis of Laminated Anisotropic Plates*, Technomic Publishing Company, Inc., Lancaster, PA, 1987, p. 263.

15. Jones, R. M., *Mechanics of Composite Materials*, McGraw-Hill Book Company, New York, 1975, pp. 90-96.

16. Riks, E., "An Incremental Approach to the Solution of Snapping and Buckling Problems," *Int. J. Solids Structures*, Vol. 15, No. 7, 1979, pp. 529-551.

17. Kapania, R. K. and Yang, T. Y., "Buckling, Postbuckling, and Nonlinear Vibrations of Imperfect Plates," *AIAA Journal*, Vol. 25, No. 10, Oct. 1987, pp. 1338-1346.

18. Hashin, Z., "Failure Criteria for Unidirectional Fiber Composites," *Journal of Applied Mechanics*, Vol. 47, No. 2, June 1980, pp. 329-334.

19. Tsai, S. W., *Composites Design - 1986*, Think Composites, Dayton, Ohio, 1986, p. 10-8.

20. Tielking, J. T. and Schapery, R. A., "A Method for Shell Contact Analysis," *Computer Methods in Applied Mechanics and Engineering* , Vol. 26, 1981, pp. 181-195.

21. Lajczok, M. R., "New Approach in the Determination of Interlaminar Shear Stresses from the Results of MSC/NASTRAN," *Computers and Structures*, Vol. 24, No. 4, 1986, pp. 651-656.

22. Chaudhuri, R. A., "An Equilibrium Method for Prediction of Transverse Shear Stresses in a Thick Laminated Plate," *Computers and Structures*, Vol. 23, No. 2, 1986, pp. 139-146.

23. Cooley, J. W., Lewis, P. A. W., and Welch, P. D., "Application of the Fast Fourier Transform to Computation of Fourier Integrals, Fourier Series, and Convolution Integrals," *IEEE Transactions on Audio and Electroacoustics*, Vol. AU-15, No. 2, June 1967, pp. 79-84.

24. Yang, T. Y., *Finite Element Structural Analysis*, Prentice-Hall Inc., Englewood Cliffs, NJ, 1986, p. 418.

Appendix A

Plane Stress Failure Criteria

A.1 *Hashin's Failure Criteria*

Tensile Fiber Mode, $\sigma_{11} > 0$

$$\frac{\sigma_{11}^2}{X_t^2} + \frac{\sigma_{12}^2}{S^2} = 1 \qquad \text{(A.1)}$$

Compressive Fiber Mode, $\sigma_{11} < 0$

$$\frac{\sigma_{11}}{X_c} = 1 \qquad \text{(A.2)}$$

Tensile Matrix Mode, $\sigma_{22} > 0$

$$\frac{\sigma_{22}^2}{Y_t^2} + \frac{\sigma_{12}^2}{S^2} = 1 \qquad \text{(A.3)}$$

Compressive Matrix Mode, $\sigma_{22} < 0$

$$\frac{\sigma_{22}^2}{4S^2} + \left[1 - \frac{Y_c^2}{4S^2} \right] \frac{\sigma_{22}}{Y_c} + \frac{\sigma_{12}^2}{S^2} = 1 \tag{A.4}$$

A.2 Other Failure Criteria

Tsai-Hill Failure Criterion

$$\frac{\sigma_{11}^2}{X^2} - \frac{\sigma_{11}\sigma_{22}}{X^2} + \frac{\sigma_{22}^2}{Y^2} + \frac{\sigma_{12}^2}{S^2} = 1 \tag{A.5}$$

If $\sigma_{11} > 0$, $X = X_t$; $X = X_c$ otherwise. If $\sigma_{22} > 0$, $Y = Y_t$; $Y = Y_c$ if σ_{22} is negative.

Tsai-Wu (Tensor Polynomial) Failure Criterion

Using contracted stress notation, $\sigma_1 = \sigma_{11}$, $\sigma_2 = \sigma_{22}$, and $\sigma_6 = \sigma_{12}$,

$$F_1\sigma_1 + F_2\sigma_2 + F_{11}\sigma_1^2 + F_{22}\sigma_2^2 + F_{66}\sigma_6^2 + 2F_{12}\sigma_1\sigma_2 = 1 \tag{A.6}$$

The six constant F terms are defined by

$$\begin{gathered} F_1 = \frac{1}{X_t} + \frac{1}{X_c} , \qquad F_2 = \frac{1}{Y_t} + \frac{1}{Y_c} \\ F_{11} = -\frac{1}{X_t X_c} , \qquad F_{22} = -\frac{1}{Y_t Y_c} \\ F_{66} = \frac{1}{S^2} , \qquad F_{12} = -\frac{1}{2}\sqrt{F_{11}F_{22}} . \end{gathered} \tag{A.7}$$